Nanowires: from Microchip Integrated Synthesis to Application Examples

Dissertation

zur Erlangung des akademischen Grades
Doktor der Ingenieurwissenschaften
(Dr.-Ing.)
der Technischen Fakultät
der Christian-Albrechts-Universität zu Kiel

Dawit Gedamu

Kiel
December 2013

1. Gutachter:	Prof. Dr. Rainer Adelung
2. Gutachter:	Prof. Dr. Herman Kohlstedt
Datum der mündlichen Prüfung:	Februar 18, 2014

Acknowledgments

I have recieved tremendous help through out my MSc and PhD study from my supervisor, colleagues and ofcourse my family. First and foremost, I would like to express my sincere gratitude and appreciation to my supervisor Prof. Dr. Rainer Adelung who was more than generous and continuously supporting of my Ph.D study and research. I would like to thank for his patience, motivation, enthusiasm, immense knowledge and offering me with a flexible time schedule to finalize my PhD thesis. I'd like to thank Dr. Yogendra Kumar Mishra helping in correcting my thesis and much help in writing articles.

I'd like to thank students who have worked with me for their MSc and BSc thesis in Prof Dr. Adelung's Group: Xin Jin, Necdet Onur Urs, Pervin Sahin, Torge Behrendt and Roberto Benavides. The members of the Prof. Dr. Adelung's Group have contributed immensely to my personal and professional time in TF, CAU. I am grateful to members of Functional Nanomaterials (FUN) who are very friendly, collaborative and immensely supportive when I need them. I am especially grateful for the much help I got from Sören Kaps, Ingo Paulowicz, Arnim Schuchardt, Dr. Oleg Lupan, Galina Haidarschin and former members of our group Dr. Sebastian Wille and Dr. Seid Jebril.

Many of my experiments such as sample preparation and characterization have been performed in cleanroom (Kieler Nanolabor) and I received many helps from people working at various instruments. I would like to say thank you to all people working in the group of Prof. Dr. Eckhard Quandt and especially like to thank Dr. Dirk Meyners for introducing me with electron beam lithography and many other fruitful discussions too.

I would like to thank the group of Prof. Dr. Hermann Kohlstedt who were supportive to me from designing to device fabrication of Al NWFET. Many thanks to Dr. Adrian Petraru, Dr. Ondrej Vavra, Nico Ruppelt, Dr. Rohit Soni, Mirko Hansen and Dr. Martin Ziegler. I thank you so much for your kind help and most friendly working environment you offered me.

I would like to thank Prof. Dr. Lorenz Kienle group for the TEM characterization of iron oxide nanostructures, especially Burak Erkartal for his great effort and time to determine the exact phase of the iron oxide nanowires. Thanks to Mao Deng for TEM investigation and commenting on TEM part of my thesis.

I am so thankful with the support I get from Prof. Dr. Franz Faupel

starting from the time when I come to Kiel for my MSc study. I would also like to thank Prof. Dr. Faupel and his group who were very supportive in using their lab and lab equipments. I would like to express my sincere appreciation for the enormous help I got from Dipl.-Ing. Stefan Rehders, Christoph Ochmann, Dipl.-Ing. Rainer Kloth and Dipl.-Inf. Peter Sommer.

I greatly acknowledge the financial support I got from German Research Foundation (DFG) under different schemes and *Technet_nano* project.

Finally I would like to thank my wife Hewan Teshome and my son Brook and daughter Liya for their enormous love and patience during my study. I would also like to thank my parents, brothers and sisters back home in Ethiopia for shaping my life and so much support.

Contents

1 Introduction

One-dimensional metal and semiconductor structures have gained tremendous research interest due to their unique physical, structural properties and their potential role in the miniaturization of modern electronic devices. Due to high surface-to-volume (S/V) ratio, nanowires (NWs) for example exhibit extraordinary electrical properties. Having such unique properties NWs are thus expected to become an important components of micro and nanoelectronic devices [1] and a potential implementation as devices. Based on 1D structures, several devices have already been demonstrated including light emitting diodes (LEDs) [2, 3], field effect transistors (FETs) [4–8], solar cells [9–12], and biosensors [13].

In 1965, Dr. Gordon E. Moore with Intel predicted the exponential growth in the number of transistors that could be manufactured on a chip. The number of transistors in a chip doubles every 24 months according to Moore's law and today the exponential growth continues (source: Moore's law and Intel Innovation). In relation to cost, the trend shows that the falling of a unit cost as the number of components per circuit rises [14] and the economy may dictate to incorporate many electronic components in a single chip. As a result companies that do not stay near the leading edge of process technology suffer from a cost disadvantage [15]. The leading edge technology requires to keep up with the curve as shown in Figure 1.1. This trend to smaller and smaller dimensions has actually accelerated as people have recognized the slope. The reason for interest in the miniaturization of IC (integrated circuit) is first, the cumulative device performance increases as result of short channel width. Second: decrease of costs per every device as result of high density of integrated IC's per chip. Intel *Fun Facts*, released that Intel entered volume production of the world first 22 nm 3D tri-gate Si transistor in the year 2012 after making a radical transistor design change in 2011. These examples show that how Moore's law type trends have driven the electronics

industry in order to cope up with the market and need of people.

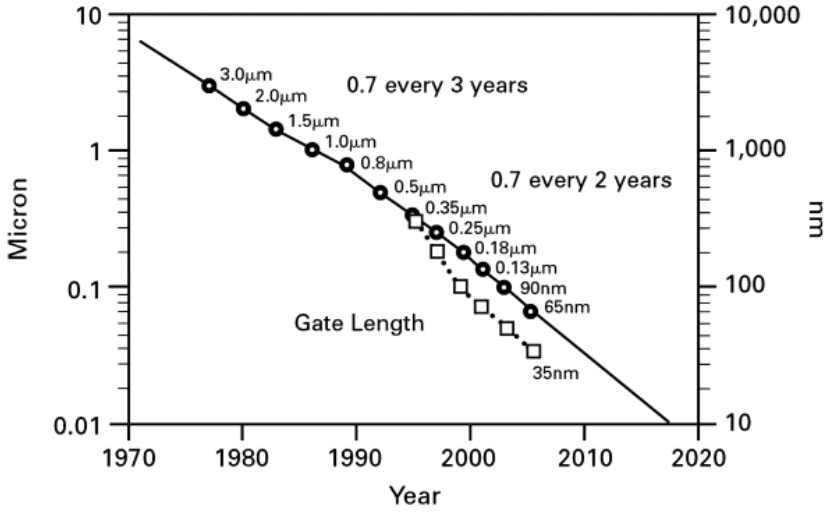

Figure 1.1: *Illustrates plot of new technology generation introductions (1975−2005). Adapted with permission from ref. [15]. Copyright: Intel.*

Emerging Research Logic Technologies in the International Technology Roadmap for Semiconductors states that one-dimensional structures, such as carbon nanotubes (CNT) and semiconductor NW field effect transistor(NWFET) are mentioned as the possible candidates offering an appealing approach to scaling CMOS [16]. However, the device application to industrial scale is only in the beginning stage. As the scaling down trend of dimensions continues, there would be a need for higher doping and channel conductance close to that a metal is required for device operation [5]. But the conductivity should be limited, because a high conductivity like in bulk metal systems poses a problem that an electric field can not penetrate except for extremely short distances. Appropriate technologies expected come up with solutions for the problems that down scaling dimensions pose. Metal and metal-metal oxide hybrid NWs are among the possible candidates that are being researched where the conductance of the NW could be modulated by external inhomogeneous electric field [17]. Rotkin and Hess [5] showed the principle of working metallic NW transistor (METFET) synthesized from typical armchair tubes: SWNT of 0.7 nm and 1.4 nm in diameter. The electric field applied through a tunneling tip penetrate in the nanotube which is weakly screened so that it can permit transistor action [18]. Cheng et al have also

synthesized a sub 30 nm scale Ag silver NWs through electron beam lithography (EBL) and showed the device function as metallic electrostatic transistor that operates similar to the depletion type MOSFETs [19].

The innovations related to quasi-1D nanostructures are expected to revolutionize cheap integrated nano electronics not only through high precision positioning and integration of nano scale devices into substrate, but also through the addition of new functionalities that arise from being nano scaled materials. This new functionalities show that addition of a new dimension to Moore's law. The recent developments in industry also show the increasing importance of a new trend called *More than Moore*(MtM). According to MtM, additional *non-digital* functionalities can be incorporated into devices that do not necessarily scale according to Moore's law [20]. The technologies include typical examples such as RF, power/HV, passives, optics, sensor and actuators/MEMS or Bio-chips.

In the past few years, progress in the synthesis and characterization of NWs is thus driven by the need to understand the novel physical properties of 1D nano scale materials and their potential applications in constructing for instance nano scale electronic and optoelectronic devices [21–23]. Several methods such as templates [24–26], solution growths [27], lithographic methods (electron beam and conventional) [28, 29], VLS and its modified versions [29–32] and several others have been employed to synthesize 1D structures. Cost effective, rapid synthesis with less complex processing steps and easy integration into chips should be established for further further scale up. For that three rapid methods Flame Transport Synthesis (*FTS*), Thin Film Fracture (*TFF*) and Thermal Annealing Method (*TAM*) which add minimal processing steps are developed. For summarized introduction to these synthesis techniques, go to the appendix.

1.1 Thesis Layout

This thesis incorporates seven chapters that include basics on nanotechnology relevant to the thesis, synthesis of devices and metrology. The chapters is organized as follows after this introduction:

- **Chapter 2**, discusses fundamental challenges and concepts relevant to NWs. The quantum confinement effects and associated characteristic lengths, den-

sity of states, electron transport mechanisms and electron tunneling in nanostructures are presented.

- **Chapter 3**, presents some of the characterizing instruments used and the scientific principles behind them.
- **Chapter 4**, details the practical procedures involved in device synthesis starting from designing to experimenting are discussed. Due attention is given to conventional lithography as it is the basic step for the different types of synthesis involved. Also results that are important and a must for the next processing step are given.
- **Chapter 5**, presents mainly results from semiconductor NWs (nanostructures) synthesized through TFF and FTS approaches. Chip integrated ZnO NW (nanostructure) photo-detector fabricated through the two synthesis techniques are compared and model for the high performance photodetection is proposed. The versatility of FTS is also shown through the synthesis of SnO_2 nanostructures.
- **Chapter 6**, covers the synthesis and application of metal-metal oxide hybrid structures fabricated using TFF and TAM techniques. Important experimental step are also briefly discussed. Results from core-shell NWs that are used potentially as NWFET and different sensoric applications are also presented.
- **Chapter 7**, presents the summary and the general conclusion of the work done in the thesis and a short outlook.

2 Theoretical Basics of NWs

The interest in 1D structures rise after the discovery of carbon nanotubes (CNTs) by Iijima in 1991 [33]. Having excellent electrical, mechanical and optical properties, CNTs are thought to become the building blocks of the next generation electronic devices. Nanostructures in general have atleast one dimension in the order a nanometer (10^{-9} m). Further more if the two dimension of a material are constrained (confined) in a nanometer scale and the third dimension is freely extended without any restriction, it is called a *NW*. It means that NWs have transverse dimensions, i.e., $width(w)$ and $thickness(t)$ that are substantially below 100 nm and the length l extends unconstrained. That results in an aspect ratio which is much greater than one as $l \gg w, t$. As the NWs dimensions are more

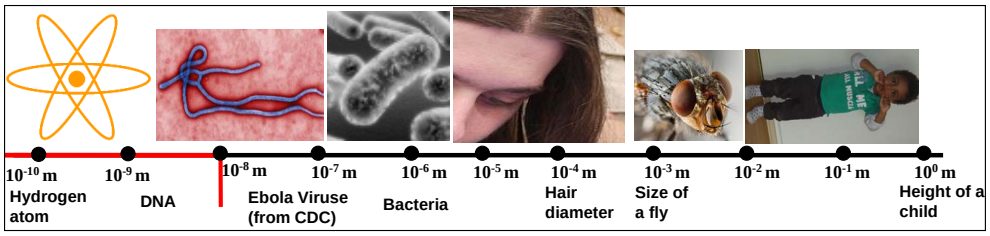

Figure 2.1: *Illustrates size comparison chart for a nano meter size to a variety of other sizes: on th right hand side is 1 m which is appr. height of a child and to a far left is the size of hydrogen atom 0.1 nm. The red marker in the picture shows the beginning of the most important scale where distinct material properties start to show up. (some pictures from copy right permitted source).*

down scaled, the importance of quantum mechanical effects comes into play and is true for materials in a nano scale level. Thus unlike bulk counter parts, nano scale materials have a non-classical characteristics that need the employment of quantum mechanics for understanding and explaining of the characteristics obtained. To name some, the quantum effects alter the electrical, optical, chemical

and mechanical properties that are very important material properties for various device applications. Thus NWs been studied thoroughly and tremendous attention up to date is given in nanoscience research and nanotechnology as they possess unique and fascinating properties superior to their bulk counterparts. For instance such metals follow Ohms law in their electrical characteristics. As the size approaches the atomic scale, however, all the knowledge we have about such material properties become invalid. The famous Ohm's law, which predicts that the resistance of a conductor scales proportional to its length, breaks down. If the electrons traverse an atomic-sized conductor (ballistic), the resistance becomes independent of its length [34], basically quantum mechanical effects dominate. Such unique properties of NWs are expected to come up with a potential applications in many area such as in electronic devices and sensor [35, 36].

2.1 Challenges of NWs

Despite the attractive features on NWs, there are a number of challenges that still remain unsolved in relation to the complexity of NWs synthesis, integration into chips, cost and controlled mass production. Issues of synthesis and integration of NWs into chips is considered in the sections below.

2.1.1 Synthesis

NWs in general could be synthesized through top-down, bottom-up, a combination of the two [37] or even through reshaping of thin films (e.g., TAM). Typical examples for top down approach are photolithography and electrophoresis. The basic principle of photolithography is illustrated and explained in Chapter 4. In this approach, one starts with a macroscopic piece of material out of which a nanostructure device is made. In bottom-up approach, the material synthesis takes place starting from atomic or molecular species via chemical reactions, allowing for the precursor particles to grow in size (i.e., controlling atoms from bottom (substrate) and assemble them to grow up). NWs in a bottom-up approach are synthesized by combining of constituent adatoms and most NW synthesis technique use bottom-up approach. The attributes of top-down and bottom-up

approach are also combined for instance the case of VLS synthesis. A photolithography or electron beam lithography (EBL) defines the position of the catalytic particle (e.g., Au) on the chip and is followed by deposition of NW material (ZnO) at the predefined location. Chemical method [38, 39], Lithographic methods (EBL and conventional) [29], Al_2O_3 template assisted method [40, 41], VLS or VS [30, 42] or modified versions of VLS (C-FTS), electrophoresis [43], TFF [6, 44–47] approach etc., are some the major nanostructure and NW synthesis routes that are developed. Many of these methods are either costly, complicated or time consuming especially when one considers mass fabrication point of view. The presented techniques (FTS, TFF and TAM) for NWs synthesis in this thesis offer very easy ways to over come the challenges associated with nanostructures and are found to be cost effective.

2.1.2 Integration into Chips and Mass Fabrication

Integration of NWs is one of the critical challenges that has been given lots of attention in the scientific community aiming at developing an effective method to integrate or support a large number of nanostructure devices into practical functional circuits [7] or modern electronic circuits. It is a challenging task due to the fact that integrating these 1D wires into device requires nanoscale connecting contacts among others. To integrate 1D nanostructures into device applications, it is of importance to align such nanostructures in a parallel, scalable, and highly reproducible manner independent of the specific materials. Because well aligned 1D nanostructures might exhibit superior properties that are not found in their disordered counterparts, allowing promising applications in diverse fields [48]. The manual method *Pick-Place* of a single NW among many randomly deposited NWs for investigation is expensive, time consuming, complicated and tedious. Ye et al., [49] demonstrated a robotic pick-place of NWs decreasing the complexity and up to some extent increasing efficiency if one should employ such a method. Nevertheless, even in its automized version, this method is still complicated and expensive. Efforts have also been exerted in finding out new and simpler ways of integration of NWs. With combination of fluidic alignment and surface patterning [50], crossing wires techniques [51, 52], metal-catalyzed simultaneous growth of NWs and electrodes [53]and [54], using high speed roller for transfer printing [55]

Bosch-process-based and micromachining [56], etc., are some of the suggested ways that have been investigated as a possible routes of NWs integration. Possible options include an independent synthesis of NWs as first step and then integrating them into the devices. Many of these methods stated earlier are either too slow or too expensive when one looks from mass fabrication or market point of view. Thus there should be an optimal way in which NWs can get proper support or integration with minimum cost and complexity could be done.

2.2 Energy Band Diagrams

According to Pauli exclusion principle, an orbital can hold zero, one or two electrons and two electrons when the electrons have opposite spins. Therefore, an atom can never have more than two electrons per orbital. The question then is *what happens when two identical atoms are placed next two each other for instance in formation of pure bulk solid material?* When identical two atoms are far from each other, the electrons of atom 1 will have the same energy as the electrons of atom 2, [57]. However when these atoms are brought to a close proximity, the orbitals overlap and the electrons suddenly start to occupy each sublevel that come to face to face with their clone. The orbital overlap also results in the

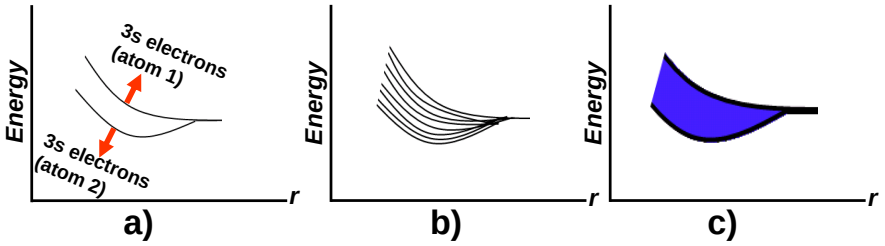

Figure 2.2: *Schematic illustration of the energy of the outermost electrons of two sodium atoms as a function of separation distance* **r**. *a) Atom 1 and atom 2 are at large distance from each other that the two electrons have equal energy. As the orbitals overlap, the outermost energy sublevel splits. b) When eight atoms are closer each other, the energy sublevel splits into eight. c) When large number of atoms brought together, the energy sublevel splits become too close and appear to be continuous energy band.*

outermost energy sublevel splitting which would result in two different energies

for the electrons. Let us take a typical example of sodium atoms that could be placed at far and close distances from each other. The energy sublevel splitting at different number of sodium atoms [57] that are brought close together is illustrated in Figure2.2. As more and more sodium atoms are brought together, more splits occur with in the energy sublevels. This appears to be more like a continuous energy band as shown in Figure2.2c). Thus solid bulk materials are defined in a way that possess similar number of energy sublevel splits like the number of atoms it is constituted from.

2.3 Conceptual NW Model

In order to understand properties of 1D structures, it is important to explore basic ideas from quantum mechanics so that it will help one to evaluate the potentials of such structures in the next generation electronic devices. The starting equation that helps for the derivation of the size effects is the famous Schrödinger equation. The time independent three dimensional Schrödinger equation for the energy eigenfunction $\psi(x, y, z)$ of electrons is given as

$$-\frac{\hbar^2}{2m^*}\nabla^2\psi(x,y,z) + V(x,y,z)\psi(x,y,z) = E\psi(x,y,z). \tag{2.1}$$

with $\hbar \equiv h/2\pi$

where: h is the universal Planck's constant, E is the energy, m^* is the effective mass of the electron, V is the potential energy of the electron at position (x, y, z). Starting from equation 2.1, the electron quantum confinement in relation to the size or down scaling of the NWs can be found. In the sections and subsections below, the quantitative relationship will be derived through consideration of appropriate boundary conditions. A much plausible derivation of the NW model given below as shown by Khare et al. [35] is directly taken. As the size of a NW is approaching to the size a few electron wavelengths, the electron energies become quantized and the spacing between the energy levels become larger. This could be shown by solving Schrödinger equation for a NW potential confined in 2D and a potential along the axis of the wire(x). Thus the total potential $V(x, y, z)$ is

$$V(x,y,z) = V(x) + V(y,z). \tag{2.2}$$

and eigenfunction can be written as

$$\psi(x, y, z) = \psi(x) + \psi(y, z). \tag{2.3}$$

Using equations 2.2 and 2.3 in equation 2.1, one could get

$$-\frac{\hbar^2}{2m^*}\left[\psi(y,z)\frac{\partial^2\psi(x)}{\partial x^2}\psi(x)\frac{\partial^2\psi(y,z)}{\partial y^2} + \psi(x)\frac{\partial^2\psi(y,z)}{\partial z^2}\right]$$

$$+\psi(x)V(y,z)\psi(y,z) + \psi(x)V(x)\psi(y,z)$$

$$= \psi(x)(E_x + E_{y,z})\psi(y,z). \tag{2.4}$$

Associating the kinetic and potential energies on the left-hand side of equation 2.4 to the corresponding equations on the right-hand side and realizing that $V(x) = 0$ (meaning there is no potential gradient along the wire axis), yields two decoupled equations:

$$-\frac{\hbar^2}{2m^*}\frac{\partial^2\psi(x)}{\partial x^2} = E_x\psi(x), \tag{2.5}$$

and similarly the other part of equation is

$$-\frac{\hbar^2}{2m^*}\left[\frac{\partial^2\psi(y,z)}{\partial y^2} + \frac{\partial^2\psi(y,z)}{\partial z^2}\right] + V(y,z)\psi(y,z) = E_{y,z}\psi(y,z). \tag{2.6}$$

The solution of equation 2.5 is

$$E_x = \frac{\hbar^2 k_x^2}{2m^*}. \tag{2.7}$$

where k_x is any real number. Equation 2.6 represents a confinement potential in NWs and could be solved by some assumptions. Assuming a rectangular and infinitely deep NW, and taking the potential inside the wire to be zero but taking potential outside to be infinity 2.6 changes the equation to

$$-\frac{\hbar^2}{2m^*}\left[\frac{\partial^2\psi(y,z)}{\partial y^2} + \frac{\partial^2\psi(y,z)}{\partial z^2}\right] = E_{y,z}\psi(y,z). \tag{2.8}$$

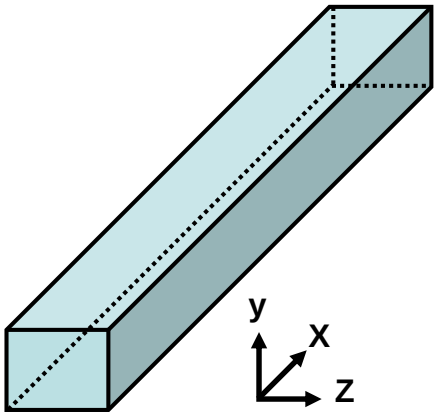

Figure 2.3: *Schematics of rectangular and infinitely long NW similar to a deep potential well confining electrons along y and z that electron transport is possible along the the x-axis.*

Outside the wire the eigenfunction $\psi(x, y, z) = 0$ as the potential is infinite. Thus $\psi(y, z) = \psi(y)\psi(z)$ through using separation of variables. Using these values and assigning corresponding energies along different axes into equation 2.8 results into two decoupled equations:

$$-\frac{\hbar^2}{2m^*}\frac{\partial^2\psi(y)}{\partial y^2} = E_y\psi(y). \tag{2.9}$$

$$-\frac{\hbar^2}{2m^*}\frac{\partial^2\psi(z)}{\partial z^2} = E_z\psi(z). \tag{2.10}$$

The solutions for equations 2.9 and 2.10 with the origin placed at the corner of the NW schematics Figure 2.3 are

$$\psi(y) = \sqrt{\frac{2}{L_y}}\sin\left(\frac{\pi n_y y}{L_y}\right),\ \psi(z) = \sqrt{\frac{2}{L_z}}\sin\left(\frac{\pi n_z z}{L_z}\right), \tag{2.11}$$

with n_x and n_y positive integers with a component energy eigenvalues given by

$$E_y = \frac{\hbar^2\pi^2 n_y^2}{2m^* L_y^2},\ E_z = \frac{\hbar^2\pi^2 n_z^2}{2m^* L_z^2} \tag{2.12}$$

The energy eigenvalues are inversely proportional to the effective mass of the electron and the square of the dimension size L. Thus the confinement energy increases with the decrease of the NW dimension.

2.3.1 Density of States (DOS)

The band structure and the density of states (DOS) of a material contain important information about transport properties like electrical or thermal conductivity. DOS is the number of states per unit energy per unit volume of real space. It determines many physical and chemical properties of materials. DOS can mathematically be written as

$$DOS(E) = \frac{dN}{dE} \tag{2.13}$$

where N is total density of states upto an energy E. Based on this formula and consideration of the total number of states (N^{1D}) in NWs are

$$DOS(E) = \frac{dN^{1D}}{dE} = \frac{dN^{1D}}{dk}\frac{dk}{dE} \tag{2.14}$$

where $N^{1D} = \frac{2k}{\pi}$. Using equation 2.7 into equation 2.14 yields

$$DOS(E)^{1D} = \left(\frac{2m^*}{\hbar^2}\right)^{\frac{1}{2}} \frac{E^{-\frac{1}{2}}}{\pi} \tag{2.15}$$

2.3.2 Quantum Tunneling

Tunneling is a quantum mechanical phenomena which electrons can pass through a thin layer of insulating film. Sommerfeld and Bethe were the first to make a theoretical study of this phenomena for very low voltages and for high voltages [58]. The tunneling phenomena arise from the wave nature of particles that they are penetrating through an angstrom thick insulating barrier. This phenomenon can be explained by through solving the time independent Schrodinger's equation. An electron with energy E approaching from the left to a thin and finite potential barrier of energy V_0, with $E < V_0$ and thin wall of width L is tunneling (transmitted) as schematically shown in Figure 2.5. The incident particle (electron) represented by the de Broglie wave at the potential barrier where it is partially reflected and partially transmitted in the potential barrier. The Schrodinger's equation is solved through separate consideration of regions I, II and III. Considering one dimensional equation, the three equations corresponding to three

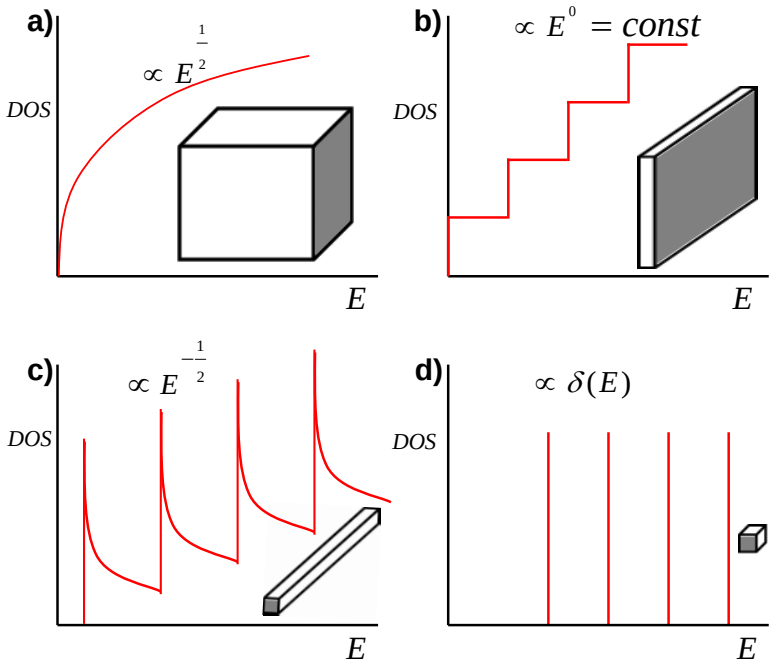

Figure 2.4: *Illustration density of states (DOS) in nanostructures depending on dimensionality: a) Bulk material that has 3 degrees of freedom for electron propagation (no confinement). If electrons are confined in one dimension and have 2 degree of freedom for propagation b), DOS increases like a stare case. c) A quantum wire that has 1 degree of freedom shows abrupt change in DOS. It has nearly discrete DOS with some continuity. d) When the electron is confined in all spatial dimension (0 degree of freedom), it is called quantum dot. The plot shows DOS for quantum dots is discrete.*

regions are written as

$$\frac{\hbar^2}{2m^*}\frac{\partial^2\psi_I}{\partial x^2} + (E)\psi_I = 0 \tag{2.16}$$

$$\frac{\hbar^2}{2m^*}\frac{\partial^2\psi_{II}}{\partial x^2} + (E - V_0)\,\psi_{II} = 0 \tag{2.17}$$

$$\frac{\hbar^2}{2m^*}\frac{\partial^2\psi_{III}}{\partial x^2} + (E)\psi_{III} = 0 \tag{2.18}$$

where m^* is the effective mass h is Planck's constant and ψ is the wave function. The potential barrier $V_0 = 0$ in regions I and III. The solutions of the above equations through consideration of boundary considerations in these regions is thus

$$\psi_I = Ae^{ik_1x} + Be^{-ik_1x} \tag{2.19}$$

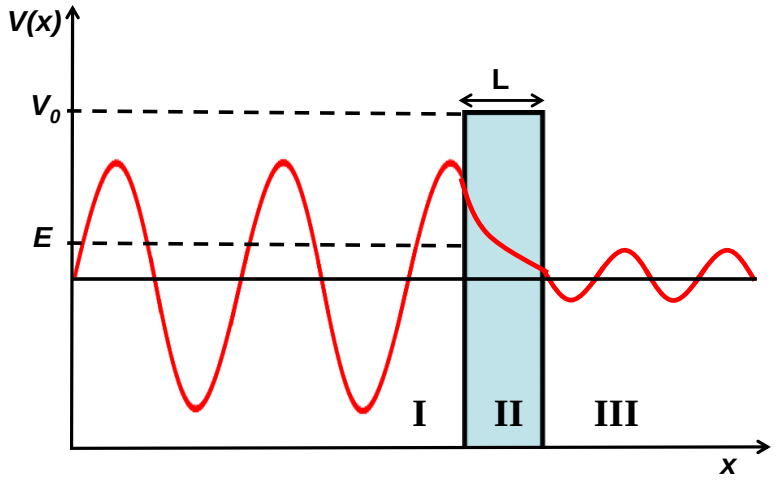

Figure 2.5: *Schematic illustration of quantum tunneling across a finite potential barrier. The amplitude of the transmitted wave is reduced as shown in region III.*

$$\psi_{II} = Ce^{ik_2 x} + De^{-ik_2 x} \tag{2.20}$$

$$\psi_{III} = Fe^{ik_1 x} \tag{2.21}$$

where $k_1 = \frac{\sqrt{2m^* E}}{\hbar}$ and $k_2 = \frac{\sqrt{2m^*(V_0 - E)}}{\hbar}$ are the wave numbers outside and inside the barrier respectively. Considering the boundary conditions and treating the incident, the reflected and transmitted waves separately, the solution of the Schrödinger equation leads to find out that the transmission probability T given as [59]

$$T = \left[\frac{16}{4 + (k_1/k_2)^2}\right] e^{-2k_2 L} \tag{2.22}$$

2.3.3 Characteristic Lengths

The electrical transport properties of materials such as metals in macroscopic scale are expected to show Ohmic behavior. However, the transport properties are determined by set of characteristic lengths if device dimensions are relatively comparable to the electron wavelength. Thus these sets of characterless lengths are important and decisive parameters for understanding the observed results. Considering an electron (as a particle) on the basis of classical mechanics, it can be characterized by mass m and a momentum vector $\boldsymbol{p}$. With certainty, the position

of center of mass of the electron is known in space $\boldsymbol{r}$. From quantum mechanical point of view, however, electron has wave characteristics that is given by wave function $\psi(\boldsymbol{r})$ with a probabilistic value in finding the electron in a small volume $d\boldsymbol{r}$ around $\boldsymbol{r}$. The wave like behavior of electrons will lead to the dependency of electrons characteristics in the geometry of the samples which the electrons are either interacting or propagating. If the material dimension are in the order of characteristic length or less, the material will show intriguing characteristics which are interesting for various electronic devices and applications such as in sensors. In this section, the definition of some lengths that are related to the fundamental physical characteristics of electrons in materials are given.

2.3.3.1 Electron Wavelength

Electrons in mesoscopic systems (nanostructures) show their wave like behavior [60, 61] and the wavelength defines the scale on which quantum-mechanical effects become important. The electron wavelength length $\lambda = 2\pi/k$ called de Broglie wavelength is related a electron energy E and effective mass of electron m^*. In three dimensions, it can be expressed as

$$\lambda = \frac{h}{p} = \frac{h}{\sqrt{2m^*E}} = \frac{2\pi\hbar}{\sqrt{2m^*E}} = \lambda_0\sqrt{\frac{m_0}{m^*}} \tag{2.23}$$

where k represents the magnitude of the electron wave vector. In semiconductors the electron effective mass can be less than the free electron mass m_0 and thus the de Broglie wavelength λ is greater than that of free electron wavelength λ_0. The significance of de Broglie wave length in relation to the size can be understood by taking for instance metal structures at lower temperature where electrons have nearly Fermi energy. The Fermi energy of the degenerate electrons E_F in 3D is expressed by

$$E_F = (3\pi^2)^{\frac{2}{3}}\frac{\hbar^2 n^{\frac{2}{3}}}{2m^*}, \qquad T \to 0, \tag{2.24}$$

where n is the concentration of electrons per unit volume, m^* here is mass of electron and $\hbar$ is $1/2\pi$ of Planck's constant h. Interms of wave vector k_F, the Fermi energy is also given by

$$E_F = \frac{\hbar^2 k_F^2}{2m^*} \tag{2.25}$$

Comparison of formulas 2.24, 2.25 and using $\lambda_F = 2\pi/k_F$ results

$$\lambda_F = \left(\frac{3n}{8\pi}\right)^{-1/3} \tag{2.26}$$

In general, $k_F \approx (n)^{1/d}$, where d represents the dimension of the system. For typical metallic systems the electron density is $n \approx 10^{29}/m^3$ [62] so that the de Broglie wavelength of electrons in metal is of the order of $0.1 - 1\ nm$. This wavelength becomes comparable to with the sizes of nanostructures that could be fabricated using modern techniques such as electron beam lithography. That is why quantum mechanical effect should be considered for understanding the characteristics of nanostructures. In similar way, assumption of low temperature for semiconductor materials, wavelength comparable to the nanostructure dimension ($\approx 1nm$) could be found [60]. In Figure 2.6, the λ vs m^*/m_0 is given

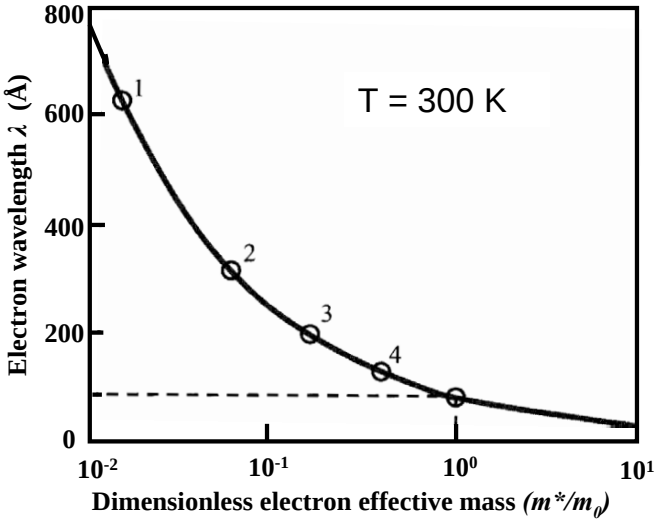

Figure 2.6: *Electron wavelength versus electron effective mass for semiconductor materials at room temperature. The points 1 to 4 in the curve correspond to materials InSb, GaAs, GaN, and SiC respectively. Reprinted from Mitin et al [63].*

for different semiconductor materials at room temperature. Points 1 to 4 correspond to InSb, GaAs, GaN, and SiC respectively. The used effective mass m^*/m_0 for each accordingly is 0.014, 0.067, 0.172, and 0.41. Assuming electron energy $E = k_B T$, where k_B is Boltzmann constant, the de Broglie wavelength for these semiconductors of effective mass $(0.01 - 1)m_0$ ranges between 73-7.3 nm which is

much larger than the lattice constant. Decreasing the temperature for instance to 3 K increase the wavelength by one order of magnitude. thus the wavelength becomes comparable to the size nanostructured devices.

2.3.3.2 Electron Mean Free Path

According to Sondheimer [64], the long free paths at low temperature for metals are very difficult to explain through classical theory, but they can be understood on the basis of quantum mechanical analysis. Bloch and many authors have analyzed of the motion of electrons in a crystal lattice and forwarded precise meanings interms of electron density and free path. Accordingly, electrons in a metal are regarded as distributed over a number of energy bands, filling most of them completely. The electron mean free path is the average distance traversed by electron between two scattering events and looses its extra energy and there by destroying its momentum. The mean free path varies from dozens of nanometers for light elements to ten to hundreds of nanometers for heavy elements. Typical examples for electron mean-free path: silicon has few nanometers (1 nm) and high-quality compound semiconductors such as GaAs have about 100-200 nm [65]. The dominant elastic scattering mechanism is impurity scattering besides other scattering sources such as lattice imperfections, phonons, electrons, grain and ground boundaries or even magnons. The mean-free path is related to the (transport) momentum relaxation time τ_{tr} by

$$l_m = v\tau_{tr} \tag{2.27}$$

where v is the average carrier speed. A "good" metal has $l_m/\lambda_F >> 1$; because electrons travel long lengths between scattering events. In metal NWs, elastic scattering in such structures is strongly influenced by grain boundary scattering rather than other scattering mechanisms.

2.3.3.3 Screening Length (Thomas-Fermi Screening Length)

It is known that metals (conductors) have free mobile charge carriers (electrons) and the electrons distribute around the surface. These electrons can shield the interior of the conductor from an applied external electric field. This is called

screening effect or some times called Thomas-Fermi screening. A classical electrostatics predicts that the external electric field induces charges on the surface that the electric field dies out to zero in the interior of the metal. However, the quantum effects predict finite penetration depth (screening length) [66] in the conductor and finite thickness for the charge distribution on the conductor [67, 68]. Suppose a positively charged particle is surrounded by sea of electrons (electron gas) and is held rigidly at one position. It will then attract many electrons around creating surplus negative charge and reduces (screens) the electric field. The electric field of the embedded charge falls off with increasing r faster than $1/r$ [69, 70], because the electron gas tend to turn around and screen the positive charge assumed with in the metallic core. Let us consider the schematics of metal-insulator-metal contact as depicted in by Black and Wesler [71] in Figure 2.7c) which is a more realistic capacitor model in which the electric field is decaying exponentially from $x = 0$ on the electrode to $x = \ell$. Using induced surface charge density in terms of electric field [72], Black et al., have shown that

$$\rho(x) = \rho_{max} exp\left(\frac{-x}{\ell}\right) \tag{2.28}$$

where ℓ characterizes the length scale of the distribution, $\rho(x)$ refers to the surface charge density at the metal/dielectric interface and ρ_{max} is the surface charge density at $x = 0$ of the electrode. Considering ideal conductors in Figure 2.7a), applying a bias voltage will induce a charge displacement in the insulator-conductor interface. Using Gauss's law, the electric displacement D is related to surface charge density by

$$\nabla \cdot D(x) = \rho(x) \tag{2.29}$$

Using the above equation, the total density per unit area can be found through integration over the entire surface:

$$D_{total} = \int \rho(x)dx = \rho_{max}\ell \tag{2.30}$$

The induced charge density is related to the biasing electric potential (Φ) for all points within the electrodes

$$\Phi = -\int E \cdot ds = -\int \frac{D(x)}{\varepsilon_0 \varepsilon_m} \cdot dx = \frac{\rho(x)\ell^2}{\varepsilon_0 \varepsilon_m} \tag{2.31}$$

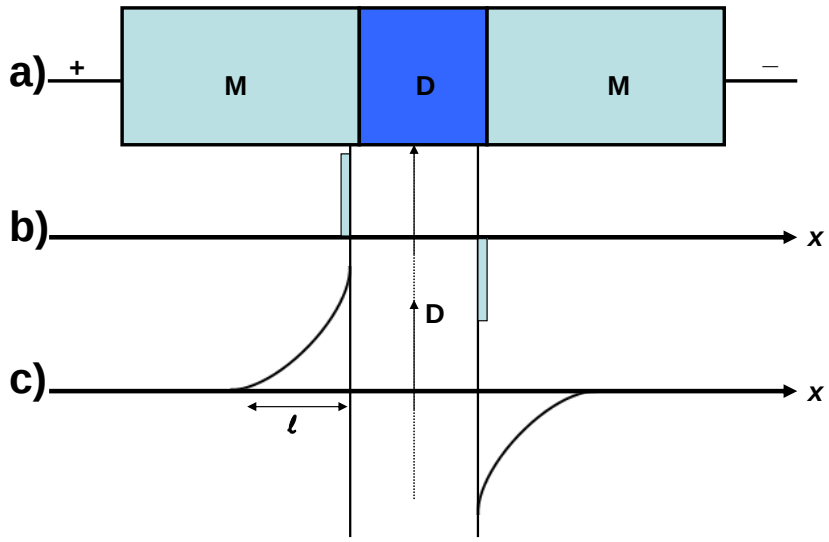

Figure 2.7: *(a) Schematic illustration of a metal-dielectric-metal sandwiches under bias voltage. (b) shows a simplest approximation, displacement charge in the electrodes builds up in an infinitely-thin plane at the electrode/dielectric interface. (c) A more realistic model acknowledges that the displacement charge occupies a finite spatial extent (l) [71].*

The field depth in the electrode is assumed to be zero for simplified evaluation of the electrostatic potential. Thus the surface potential at the metal/dielectric interface is

$$\Phi(0) = \frac{\rho_{max}\ell^2}{\varepsilon_0\varepsilon_m} = \frac{D_{total}\ell}{\varepsilon_0\varepsilon_m} \tag{2.32}$$

An effective dielectric constant ε_m is introduced in equations 2.31, 2.32 which is dependent on the polarizability of bound electrons in the underlying metal lattice. Because of free electrons, bulk metals are assumed to have an infinite dielectric constant.

The screening length ℓ is estimated through the use of Thomas-Fermi approximation that relates the potential(Φ) at any point in an electron gas to the electron density at that same point. In this model a static (DC) conditions are imposed. With this condition and using binomial series approximation for $e\Phi(x) \ll E_F$, the induced charge density is

$$\rho(x) = \rho_0\left[1 - \frac{e\Phi(x)}{E_F}\right]^{\frac{3}{2}} - \rho_0 \approx -e\rho_0\frac{3\Phi(x)}{2E_F} \tag{2.33}$$

where E_F is the Fermi energy of the electrode, and ρ_0 is the bulk conduction-electron density. Substituting the results of equation 2.32 into 2.33, the electric field penetration can be solved to yield to

$$\rho(x=0) = \rho_{max} \cong -e\rho_0 \frac{3\rho_{max}\ell^2}{2\varepsilon_0\varepsilon_m E_F} \tag{2.34}$$

The penetration depth ℓ in terms of intrinsic properties can then be written as

$$\ell^2 = \varepsilon_m \frac{2}{3}\frac{\varepsilon_0 E_F}{\rho_0 e} \tag{2.35}$$

Typically the value $\frac{2}{3}\frac{\varepsilon_0 E_F}{\rho_0 e}$ is defined as the Thomas-Fermi screening length ℓ_{TF} squared. Thus 2.35 can be rewritten in short form as

$$\ell^2 = \varepsilon_m \ell_{TF}^2 \tag{2.36}$$

2.4 Electrical Transport in NWs

The classical free electron conduction assumes that electrons in metal behave like gas molecules moving statistically through out the lattice. This lead to the formation of Ohms law which relates the electric current to the applied voltage for a bulk metallic conductor. The electrical resistance R which is the reciprocal of the electrical conductance is related to the conductivity σ by

$$R = \frac{l}{\sigma A} \tag{2.37}$$

where l and A are the length and cross-sectional area of the conductor respectively. From the simple Drude classical theory model, the electrical conduction involves the motion of free charges carriers (electrons) in a material under the influence of an applied electric field. Take a conducting wire, a voltage (potential difference) at the two ends of the wire supplies an electric field that applies the force on free electrons in the conducting wire. The conductivity σ, which relates the electric current density to the electric field by $j = \sigma\mathbf{E}$, is expressible in terms of the areal charge density ρ_S for 2D electron gas of effective mass m^* through

the equation [69]

$$\sigma = \frac{\rho_S e^2 \tau}{m^*} \tag{2.38}$$

τ refers to the average time since the last collision (scattering) of an electron in the conductor while it is drifting through the conductor. The larger τ, the better is the conductance as electrons travel more distance. The scattering of electrons can take place from two possible sources: collisions of conduction electrons with the vibrating lattice ions and collisions of electrons with the impurities present in the metal. The value τ is usually in the order of $10^{-14}s$. It was also been proven that conductivity is dependent on temperature. This can be proved through the consideration of free electrons resembling molecules of a gas and therefore the laws of kinetic theory of gases are applicable. Through this assumption and kinetic energy of electrons, the thermal velocity v_{th} of electrons is shown as

$$v_{th} = \sqrt{\frac{3kT}{m^*}} \tag{2.39}$$

where k is the Boltzmann constant and T is the absolute temperature. Using $\tau = l_m/v_{th}$ and 2.39 into equation of conductivity 2.38 it can be shown that

$$\sigma = \frac{\rho_S e^2 l_m}{\sqrt{3m^* kT}} \tag{2.40}$$

l_m is mean free path of electrons. The decrease in conductivity is because electrons travel a shorter distance before they encounter scattering as the temperature increases. Because of lattice vibrations, the probability of scattering of moving electrons with the lattice increases and as a result this in turn decreases the conductivity. Experimental results however showed that the inverse relation of conductivity to the square root of temperature is not exact but the conductivity is linearly decreasing with the temperature [73, 74]. For metals in general increasing temperature results in a larger lattice vibration and shorter τ which lowers the conductivity.

2.4.1 Hopping Conductance in NWs

The quantum confinement effects are well known to influence the electrical transport properties of 1D systems that are very different from their bulk counterparts in a certain temperature regimes. Wang et al., [75] experimentally showed that Bi NWs undergo a semimetal-semiconductor transition due to two-dimensional quantum confinement effects. Gold NWs ranging from 8-30 nm in diameter [76] and platinum NWs of diameter 70 nm [77] also showed a decrease in resistance as the temperature increases. Similar behavior in resistance is also shown in a vertically standing graphenes when temperature is increased up to room temperature [78]. All these studies show that under thermal activation, carriers could be transferred from occupied to unoccupied states through the involvement of phonon (causing phase change in electrons wave function), which is called hopping.

Hopping is a mechanism of conduction in realistic strongly disordered systems. The hopping conductance has a characteristic temperature dependence and was first derived by Mott [79]. It is also called Mott variable-range hopping or simply variable-range hopping (VRH). It describes the variable range hopping at low temperatures of highly disordered systems and are due to localized charge carriers and electron-electron interactions play important roles in these systems. The hopping conduction is associated with hole jumping from occupied acceptors to empty ones and governed by the hopping probability between impurity sites [80]. For a hopping hole there is the lowest activation energy ΔE (energy separation between adjacent states) and corresponding optimum hopping distance r (which maximizes the hopping probability). In zero bias condition, the hopping probability is

$$P \sim exp\left(\frac{-2r}{a} - \frac{\Delta E}{k_B T}\right) \tag{2.41}$$

where k_B is the Boltzmann constant and a is the localization length of the hole wave function. The hopping distance $r \gg a$, depends on the temperature according to $r = [9a/(8\pi N(E_F)k_B T)]^{1/4}$ for a 3D system. Here $N(E_F)$ is the density of states near the Fermi level and the corresponding activation energy is $\Delta E = 3/[\pi r^3 N(E_F)]$. The hopping probability at elevated temperature then

becomes

$$P \sim exp\left(-\frac{\Delta E}{k_B T}\right) \tag{2.42}$$

resembling an Arrhenius relation describing a nearest neighbor hopping mechanism with an activation energy. Consideration of negligible electron-electron interaction in Mott's model, and assumption of constant $N(E_F)$ the temperature dependence of the resistance R for d dimensional systems is given by

$$R = R_0 exp\left[\left(\frac{T_0}{T}\right)^{\frac{1}{1+d}}\right] \tag{2.43}$$

where R_0 and T_0 are materials constants and T_0 is given as

$$T_0 = \frac{18}{k_B a^3 N(E_F)} \tag{2.44}$$

k_B is the Boltzmann constant, a is the localization length, and $N(E_F)$ is the density of states at the Fermi energy E_F.

The value of d for 3D, 2D and 1D system is 3, 2 and 1 respectively. Thus if electron transport takes place by hopping to the nearest neighbor localized sites in NWs, then temperature dependent conduction from equation 2.43 simplifies to

$$R = R_0 exp\left[\left(\frac{T_0}{T}\right)^{\frac{1}{2}}\right] \tag{2.45}$$

The conduction through hopping in NWs is thus $T^{\frac{1}{2}}$ temperature dependence. With decreasing temperature, hopping over large barriers to the nearest neighbor localized sites becomes energetically unfavorable than to a distant site lower barrier height, i.e VRH dominates. NWs formed in growth process suitable for mass fabrication are typically consisting of short single crystalline wire segments separated by grain boundaries or narrow necks. Unlike in the crystals, quantum mechanical effects dominate like ballistic transport, the current is dominated by the connections in between. Those dominate the overall conductivity and are responsible for the sensitivity of NWs [81]. Al and Ti NWs synthesized in TFF approach have shown a conductance of Mott's type of temperature dependence and results of investigation are given in the subsequent chapters.

3 Characterization Techniques

In this chapter, the working principles of major instruments used for characterization are discussed. Many other instruments such as profilometer, optical microscope, mask-aligner, spin coater, picoampere meter, source meter, UV source lamp, various furnaces including hot plates and many other have been used. Detail discussion however, is given for four instruments in the following sub sections.

3.1 Atomic Force Microscope (AFM)

The atomic force microscopy (AFM) is one of a the scanning probe microscopes which is invented by Binnig, Quate and Gerber in the early 1980s after the introduction of surface studies through scanning tunneling microscope (STM) [82]. Using STM, Binning and Rohrer in IBM Zurich showed a 3D atomic resolution image for a highly conductive material. This invention led them to receive Nobel Prize for Physics in 1986. Few years later, the same group has invented AFM from the combination of the principles of STM and the stylus profilometer which could be utilized to characterize the surfaces of nearly all materials [83]. AFM has demonstrated a high resolution that atomic and molecular levels can be viewed and in addition it has some significant advantages as compared to other probing microscopy systems such as electron microscopes. All kind materials including biological materials could be characterized and analyzed through AFM. Besides that it does not require specially prepared samples (coating samples with conductive layers in SEM or STM) which permits for characterizing samples in near native conditions.

3.1.1 Principles of AFM

The underlying principle for the operation of AFM is detecting the bending of a cantilever in response to the small force on the tip as it scans the sample surface. The most commonly used materials for the fabrication of cantilevers with integrated tips are silicon nitride (Si_3N_4) or silicon (Si) and the tip diameter could be $10 - 50$ nm. The smaller the tip diameter the higher is the resolution. A cantilever in general is a thin rectangular lever with some hundreds of micrometers long and a few micrometers wide. The forces between a sharp tip (probe) surface at very short distance ($0.2 - 10$ nm). The piezoelectric actuator that is intact with the sample performs scanning relative to the tip (not shown in the schematics). The force between a sharp tip (probe) and microscopically rough sample surface is detected at a very short distance ($0.2 - 10$ nm). The deflections of the cantilever are measured through a laser that is reflected off the back of the cantilever and collected in a position sensitive photodiode. The deflection received is then converted into an electrical signal to produce the images. The position of the laser spot is measured through comparing the signals from the four sections of the diode as shown in Figure 3.1. In Figure 3.1b), the tip-sample distance covers various ranges. As a result of this, the tip-sample interaction involve various forces. The dominant interactions at short probe-sample distances are Van der Waals interactions. However long-range interactions (i.e adhesive, electrostatic, magnetic) are significant when tip is further away from the surface. The sample predominantly experiences repulsive van der Waals force that exists when two surfaces (fine tip and sample) are brought near to each other (few Å). As the tip moves further away from the surface(≥ 1 nm) attractive Van der Waals forces are dominant.

3.1.2 Scan Modes

According to Hookeṫs law, the cantilever which is in a raster-scan across the sample surface exhibits a locally varying deflection($\Delta z = \Delta F/k_c$) directly representing the surface morphology of the sample surface. Δz is the deflection, ΔF is the force and k_c is spring constant of the cantilever. If the spring constant of cantilever (typically 0.1-1 N/m) is less than surface, the cantilever bends and

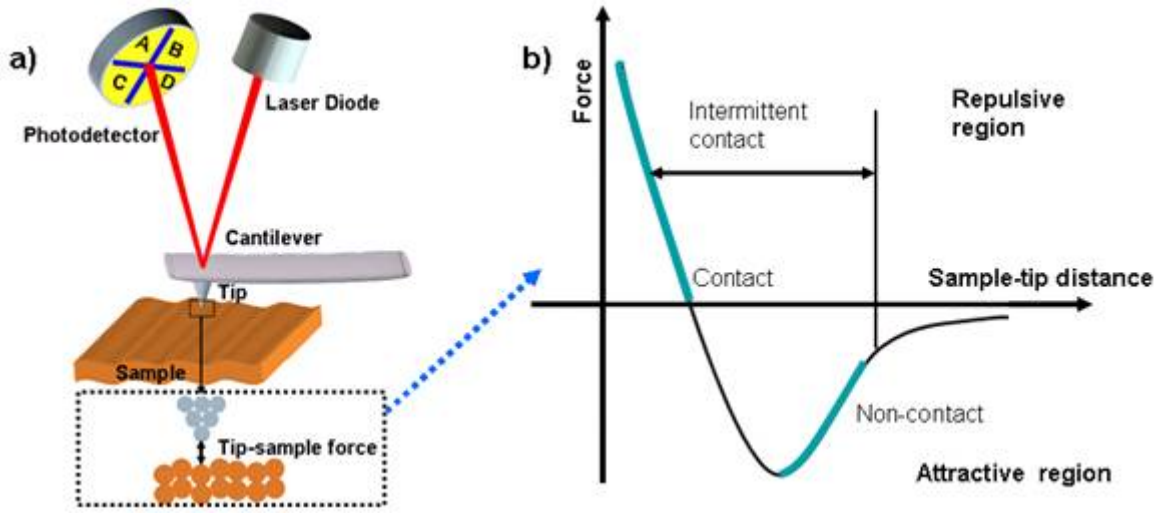

Figure 3.1: *a) Schematic depiction of AFM and its working principle. The tip experiences a force that causes displacement of the cantilever causing a signal deflection that is detected through position sensitive detector consisting of photo diodes. b) Graphical representation of the force of interaction between the tip and the sample (Lennard Jones potential)*

the deflection is monitored [84]. There are three general types of AFM imaging modes: contact mode, tapping mode and non-contact modes. However, because of AFM's versatility nature there are also other modes such as magnetic force mode, lateral force mode and some others. In the following sections the two common modes that are used during imaging are discussed.

3.1.3 Contact Mode

Contact mode is the most common method of operation of the AFM and is useful for obtaining 3D topographical information on micro and nano scale levels. As the name suggests, the tip and sample remain in close contact as the scanning proceeds. During contact with the sample, the probe predominately experiences repulsive Van der Waals forces. By maintaining a constant cantilever deflection (from feedback loops) the force between the probe and the sample remains constant and an image of the surface is obtained. The cantilever with spring constant of 1 N/m bends upward because of the repulsive force.

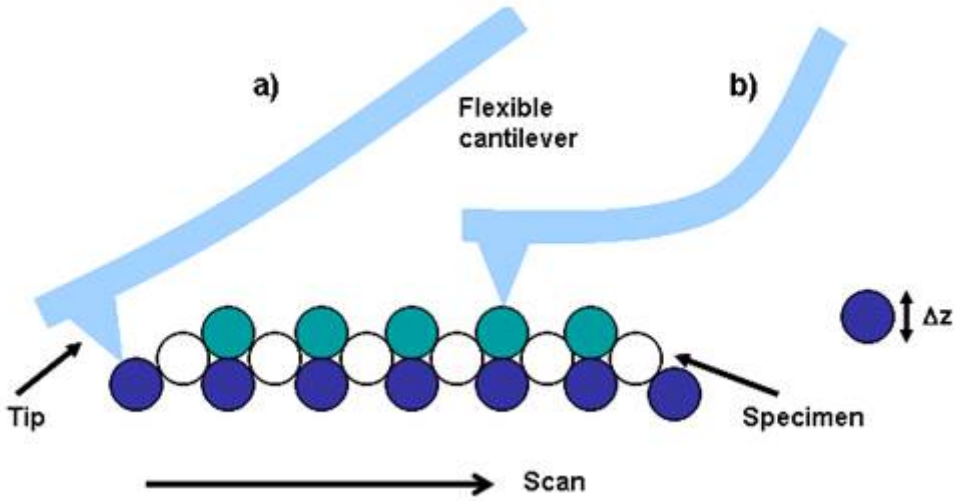

Figure 3.2: *Schematic depiction of contact mode. a) The sample is raster scanned while the tip is in soft physical contact where the cantilever is in a no bending condition. As the tip hovers on the sample surface, a larger height (b) results more repulsive force causing the bending of the highly flexible cantilever.*

As the tip is dragged over the specimen, contact mode is a disadvantage since large lateral forces are exerted on the sample. This may result in a deformed image or a damaged specimen. Small later forces however can provide about the friction or dragging resistance of the sample when the AFM is in a lateral force mode. As compared to other modes of operation, contact mode in general has advantage in speed of scanning, good for rough samples with extremely changing topography and can give atomic resolution.

3.1.4 Non-contact Mode

In this mode the probe oscillates above the surface of the sample at distance (at least 1 nm) such that it is no longer in the repulsive regime but in the attractive regime of the inter- molecular force curve(long-range interactions). This allows scanning without changing the shape of the sample. All samples unless otherwise in a controlled UHV or environmental chamber have some liquid adsorbed on the surface which makes non-contact mode difficult. Using a feedback loop to monitor changes in the amplitude due to attractive VdW forces the surface topography

can be measured. In this mode a very low force on the sample ($\approx 10^{-12}N$) and the probe will have long life time. The disadvantage of this mode is generally lower resolution; contaminant layer on surface can interfere with oscillation; usually need ultra high vacuum (UHV) to have best imaging.

3.2 Scanning Electron Microscope (SEM)

When small scale objects are desired to be magnified or imaged, the first instrument that comes to mind in tradition is optical microscope. The optical microscope gives a microscopic scale details of the object under investigation. However, the more resolution is required, the optical microscope reaches to a limit where it can not resolve more. Thus the need for SEM and TEM comes to support for optical microscope. SEM is one of the scanning probe microscopes that uses focused beam of electrons (probe), scanning in vacuum the specimen surface, imaging one point at a time. Electrons in scanning electron microscopes are accelerated at voltages in the range of usually 0.1 to 50 kV. The interaction of the electron beam with every point of the specimen surface is registered as explained in the following subsections.

3.2.1 Principle of SEM

The design of SEM are usually different from one manufacturer to another, but the basic concepts of the working principles of all SEMs are the same. The basic structure of SEM machine and its parts are depicted in Figure 3.4. A beam of electrons is produced at the top of the microscope by an electron gun. Most older SEMs use tungsten (W) or lanthanum hexaboride (LaB_6) or cerium hexaboride (CeB_6), thermionic emitters, however new microscopes are increasingly equipped with cold, thermal or Schottky field emitters for better performance, reliability and life time. In thermionic emitters a rise in temperature will increase the kinetic energy of electrons so that they can overcome the work function (the energy barrier of the filament) E_w, and escape from it. The current density, J_c, obtained from the emitter by thermionic emission is expressed by the Richardson

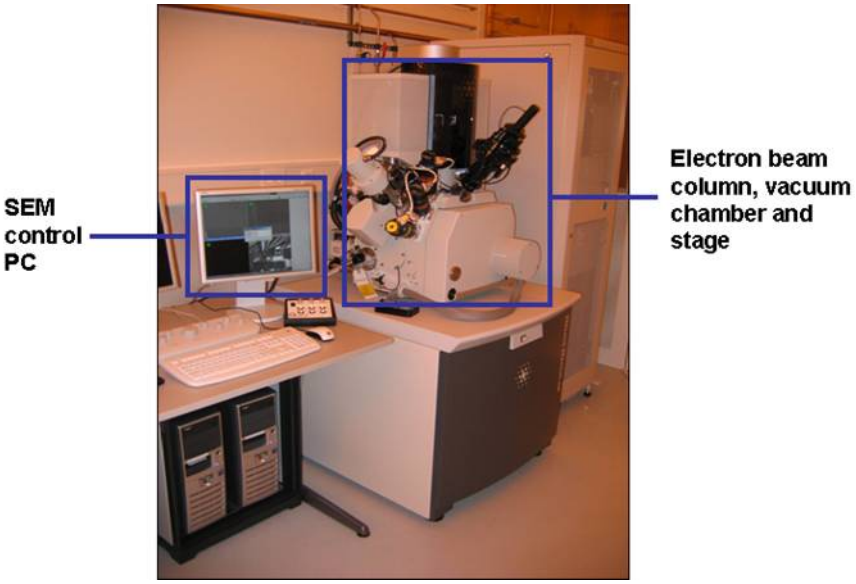

Figure 3.3: *FEI Dualbeam Helios SEM machine. This is a multi-purpose machine that currently equipped with EBL, EDX and FIB besides SEM characterization technologies (Raith SEM facility, Kieler Nanolabor).*

equation:

$$J_c = A_c T^2 exp(-E_w/kT) \quad A/cm^2, \tag{3.1}$$

where A_c is the experimental value varying with the material and lies between 50 *and* 100 $A.cm^{-2}K^{-2}$ is a constant for all thermionic emitters, $T(K)$ is the absolute emission temperature, and k is Boltzmann constant. Field emission like thermionic emission is another way of electron beam emission. The difference however is that the emitter is not heated so that electrons escape from it and for this reason are often referred as *cold field emission*. It is based on the quantum mechanical tunneling effect and can provide high current densities in the order of 10^6 $A.cm^{-2}$

The electron beam is accelerated and follows a vertical path through the microscope, which is held within a vacuum. The beam travels through electromagnetic fields and lenses, which focus the beam down toward the sample. At sufficiently high acceleration voltages an electron probe will have say a diameter of 5 nm and a current of 10 pA. The electron probe is scanned across the specimen in raster mode with the aid of two pair of deflecting coils. The interaction of the

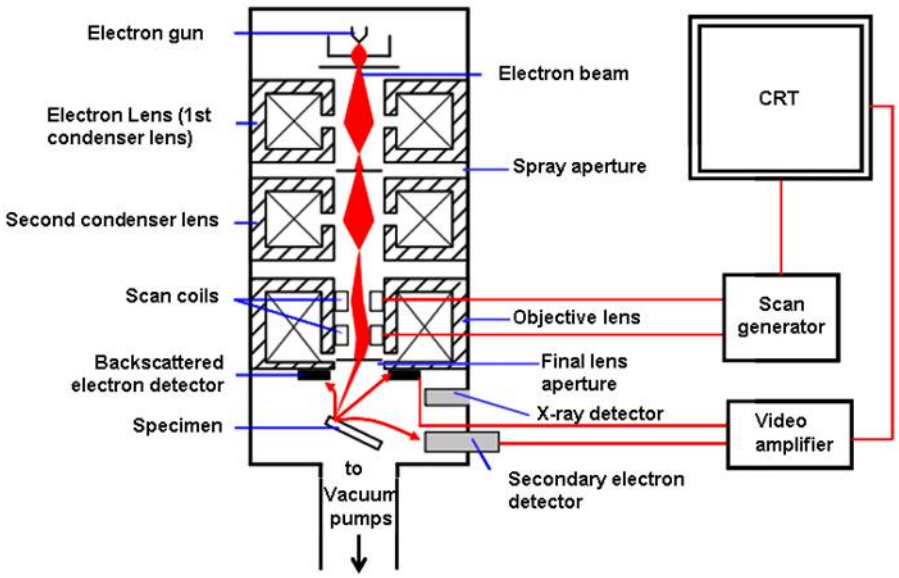

Figure 3.4: *Schematic drawing of the main components of SEM: electron column, scanning system, detector(s), display, vacuum system and electronics controls. An electron beam is generated in the gun and focused on to the specimen by the condenser and probe forming lenses. The scan coils make the probe scan across the specimen. The secondary and back scattered electrons converted as signals by the detectors will be amplified and sent to a CRT (screen)*

primary electrons with the specimen gives a series of effects in which electrons and X-rays are ejected from the sample. The ejected electrons and rays will be collected by collector grid, detected and converted into signal to form image in the screen.

3.2.2 The Probe-Sample Interaction

When electrons that are accelerated with significant amounts of kinetic energy in SEM interact with the sample, scattering phenomenon happens which energy is dissipated and the incident electrons are decelerated in the solid sample. The scattering process between electron and the sample could be elastic with atomic nucleus or inelastic with atomic electrons. The elastic interaction could lead to the effects such as electron back scattering, diffraction and deflection of electrons depending the type of the sample material (ferromagnetic sample). The inelastic

scattering however can lead to the secondary processes such as emission of secondary electrons, excitation of plasma, emission of X-rays and Auger electrons. The interaction of the electrons with the sample produces a number of effects on the target material as depicted in Figure 3.5a). The figure shows the various possible signals that could be produced when probe interacts with the sample. Secondary electrons (SE), back scattered electrons (BSE), and absorbed electrons are produced, flowing off as specimen current. In addition, X-rays, Auger electrons, and cathodoluminescence are produced. These resulting effects allow for extraction of analytical information on various properties of the sample. The

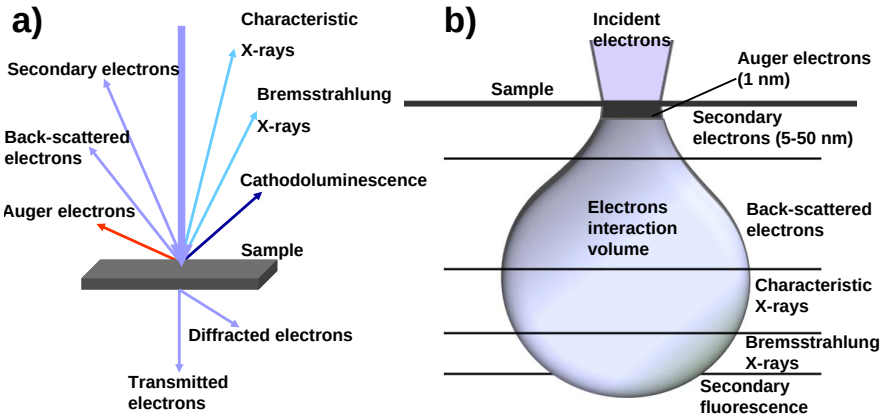

Figure 3.5: *Schematics of electron-sample interaction a) depicts various signals generated as a result of electron beam interaction with a solid and b) depicts electron interaction volume and depth representation where different signals are generated.*

zone, in which such interaction occurs and many different signals are produced is called *interaction volume* (Figure 3.5b)). The size of the interaction volume is proportional to the energy of primary electrons, its shape is determined depending upon scattering processes by the mean atomic number. Usually Monte-Carlo simulation method is used to predict the interaction volume. In the interaction volume for instance shows the escape depth (5-50 nm) at which secondary electrons sufficient energy are ejected out of the sample during inelastic scattering of the energetic beam electrons. Secondary electrons are defined purely on the basis of their kinetic energy. If the energy transferred exceeds the work function of the sample, the emitted electrons can exit the solid. All electrons emitted from the specimen with an energy less than 50 eV are referred as SE by convention and

produced with in few nm of the surface. Where as electrons emitted with energies greater than 50 eV are BSE and Auger electrons. However BSE have energy comparable to primary electrons [85]. X-rays are also produced when primary electrons eject core electrons in an atom.

3.2.3 The Detector System

The principal images produced in the SEM are of three types: SE images, BSE images and elemental X-ray maps. In this section, only electron detectors are described. SE and BSE are separated conventionally according to their energies [85]. SE have electrons with less than 50 eV energy after exiting the sample. Backscattered electrons (BSE) leave the sample quickly and retain a high amount of energy; however there is a much lower yield of BSE. As SE electrons are conveniently and the most commonly used modes of imaging in this thesis, much attention is given to the details of image formation by SE. The SE and BSE after production and integrated with collector grid is depicted in Figure 3.6a).

Most SEMs are equipped with an Everhart-Thornley (E-T) detector depicted in Figure 3.6b) that commonly detect both SE and BSE. As shown in the figure, the secondary electrons are accelerated to 10 kV by a bias voltage applied on the front surface of the scintillator. Light is emitted when energetic electrons strike the scintillator. The light flashes are then guided because of total internal reflection, detected and amplified by a photomultiplier tube. At the photocathode, the photons are converted back into electrons and electrons are accelerated toward the photomultiplier. The function of the photomultiplier is to increase or amplify original signal. Thus, for every photon generated several electrons will be produced, this will result in a significant amplification of the original signal. Through higher positive biasing of the collector grid (Faraday cage) images through majority of SE electrons can be formed. If the Faraday's cage negatively biased, it will exclude low energy secondary electrons but will receive high energy BSE whose path is line of sight with the detector forming images from BSE.

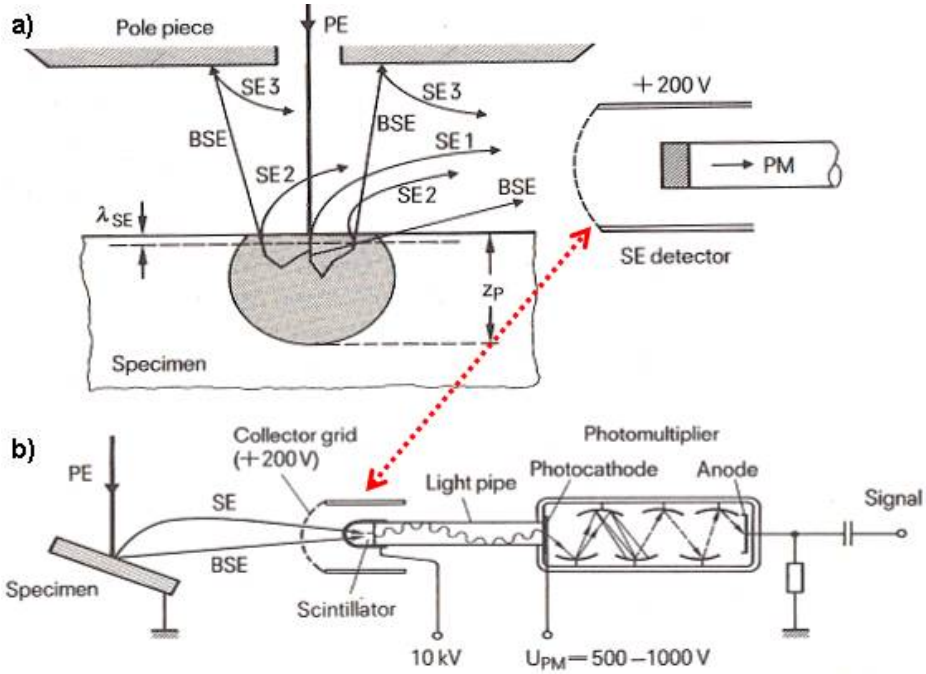

Figure 3.6: *Schematics of a) type SE collected by SE detector: the primary electron PE release only SE1 electrons; SE2 are released by BSE in the specimen. b)Everhart-Thornley SE detector. The SE generated are collected b a grid which is biased at $+200\,V$. After passing through the grid, they are accelerated towards the scintillator which is biased at $10\,kV$. After transmission through the light pipe, the SE electron signal is amplified by adjusting the voltage U_{PM} applied to the photomultiplier [86].*

3.2.4 Image Contrast in SEM

The two most broad categories of contrast include compositional/elemental contrast and topographic contrast which apply nearly for all specimens and provide the foundation of SEM image formation. Contrast is defined according to the equation as

$$C = \frac{S_2 - S_1}{S_2} \tag{3.2}$$

where $S_1 < S_2$ and both represent signals detected at any two arbitrary points in the raster scan that define image field. From the definition contrast is always positive and varies from 0 to 1. For $C = 0$ the signal is the same at two points and it means there is no contrast, where as for $C = 1$ is a case for e.g. an object

is suspended over a hole from which no signal is detected.

3.2.4.1 Compositional Contrast

The most efficient way to image compositional contrast is by using backscattered electrons because of the nearly monotonic increase of the yield of BSE with atomic number. The resulting BSE imaging reveals that regions of high average atomic number will be appearing brighter than to regions of low atomic number. The higher the atomic number, the higher is the back scatter coefficient that the back scattered signal generated from bigger atomic number is also bigger

3.2.4.2 Topographic Contrast

Topographic contrast includes all effects by which the shape and morphology of the specimen can be imaged. Vast majority of applications of the SEM involve studying shapes. Thus topographic contrast is the most important imaging mechanism it can arise from BSE and SE. As the number and trajectories of the BSE and SE depend on the angle of incidence of the beam on the specimen, topographical contrast may arise because the beam-specimen orientation. The angle of incidence varies because of the local inclination of the specimen. At each point the beam strikes, the number of BSE and SE detected gives direct information on the inclination of the specimen. The topographic contrast is also observed depending on the detector used and its placement relative to the specimen and on the exact contribution BSE and SE detected.

When only SE imaging mechanism is considered (because SE are used for SEM imaging usually), contrast of images because of dependency on SE signal can be observed. As already mentioned, SE image contrast depends on parameters like angle of incidence, primary electron energy and on detector geometry. There are different types of contrast mechanisms in SEM such as Surface tilt contrast, Shadow contrast, Diffusion contrast, Voltage contrast. The greatest contribution to the SE contrast is formed by the strong dependence of the SE yield, and hence the SE signal, on the tilt angle of the imaged specimen area. This results in the surface tilt contrast.

- **Surface tilt contrast**: This is resulted from contribution to the image

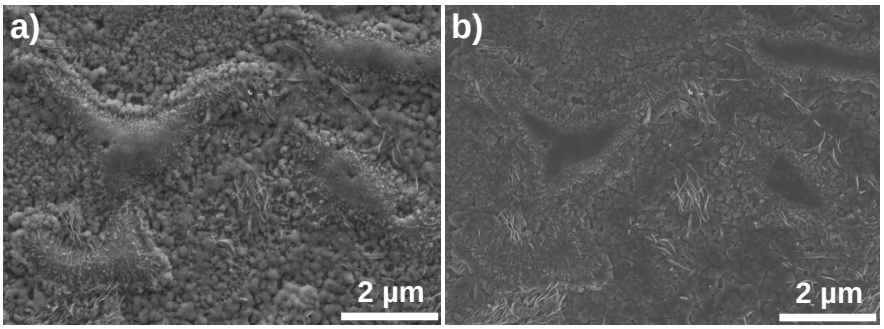

Figure 3.7: *Secondary electron SEM image of a same iron oxide sample with FEG (Carl Zeiss NTS) depicting topographical contrast at different detector geometries. a) When the image is taken with SE2 signal system where there is surfaces tilting in detector direction providing good topographic mapping . b) When the image is taken at Inlens signal system in which the detector is placed above the objective lens and detects directly in the beam path, good mapping of surface structures but low topographic contrast.*

signals that are from SE yield at different angles of tilting that provide different images.

- **Shadow contrast**: In here SE detector usually lies at a side of the specimen; this causes shadow contrast in the images. As there will be lesser SE contribution from locations, that are further away from the detector. These spots will be seen darker.
- **Edge Contrast**: Steep surfaces tend to be seen brighter than flat surfaces in SEM, since the escape distance decreases as the incidence angle increases for steep (non-flat) surfaces. This property gives a three dimensional feeling to the images acquired.
- **Diffusion Contrast**: This contrast mechanism can arise when the penetration depth of PEs is bigger than the specimen which comes up with diffusely scattered electrons can leaving the specimen. This increases the contribution of the SE2 and SE3 electrons. Since the diffusely scattered electrons are responsible for this kind of contrast, it is referred to as the diffusion contrast
- **Voltage Contrast**: When local charging alters the surface potential, the field lines of the detector potential, which exist around the sample are dis-

rupted, and collection of SE is greatly altered. A contrast mechanism develops known as voltage contrast in which the potential distribution across the surface is imaged.

3.3 Transmission Electron Microscope (TEM)

TEM is a powerful characterization instrument that become a mainstay for material scientists because of its high lateral spatial resolution (better than 0.2 nm). It has also the ability to provide both image and diffraction information from a single sample. In addition TEM provides material characterization signals such as EDX, SE and BSE imaging etc because the interaction of electrons with the sample produces characteristic informations.

3.3.1 Principle of TEM

As the name refers TEM is one of the electron microscopes that uses energies of transmitted electrons to extract information about the sample through which electrons passed in. The possible outcome of specimen-electron interactions are shown in Figure 3.5. When an energetic and focused electron beam is incident on a thin specimen (less than 200 nm thickness) [85], electrons will penetrate in both undeflected(unscattered) and deflected way (elastically scattered). The signal in TEM is obtained from these electrons and with the aid of the electron-optical lenses the image of the specimen can be magnified more than a factor of a million. The operation of TEM requires an ultra high vacuum and a high voltage. In the Figure 3.8, the gun (electron source) emits a probe of initially highly coherent and monoenergetic beam with a very small wavelength. For a typical 100 keV electrons for instance, the electrons wave length is 0.0037 nm. Such small wavelength and in phase probe are correlated with spatial associations between scattering centers (atoms). In general the higher the operating voltage, the higher is its lateral spatial resolution. The coherent energetic probe then passes through a series of additional lenses in TEM unlike SEM that has condenser lens only for image formation as depicted in Figure 3.8. For generating a beam of electron energies from 100 to 400.000 keV requires the use of larger coils to produce more

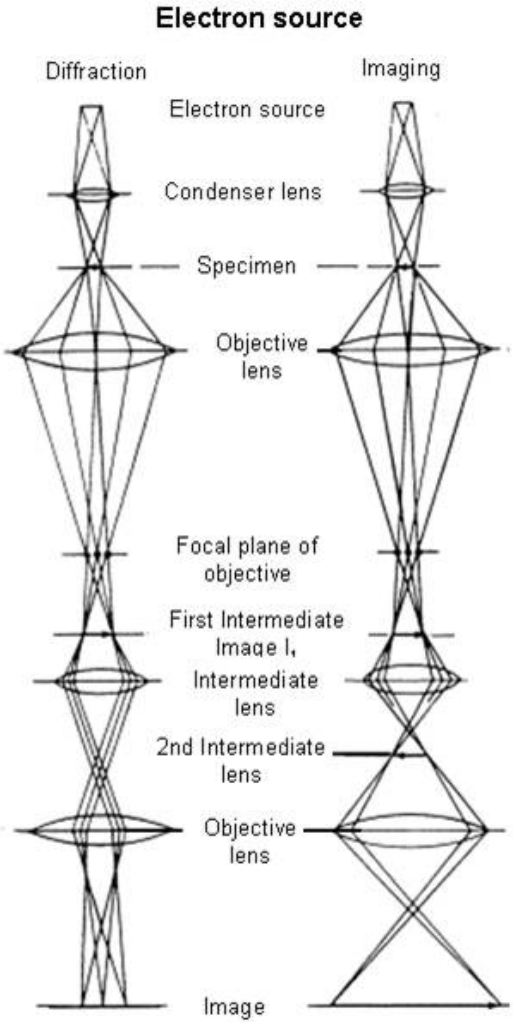

Figure 3.8: *Schematic layout of TEM. a) Ray diagram for selected area diffraction mode TEM. b) Ray diagram for bright-field imaging modes.(figure taken from [87].*

powerful magnetic fields. TEM columns as result are significantly larger than SEM columns. The TEM columns produce a highly energetic probe focused at a specimen to small spot of size a μm or less in diameter. As depicted in the figure electrons after passing through the specimen, the intermediate lenses and objective lens, they are destined to fall on the fluorescent screen or CCD camera, where either image or the diffraction patterns are recorded.

3.3.2 Diffraction and Image Modes

A simpler approach to describe diffraction in TEM is that assuming the waves behaving as if they were reflected off atomic planes as shown in Figure 3.9. From

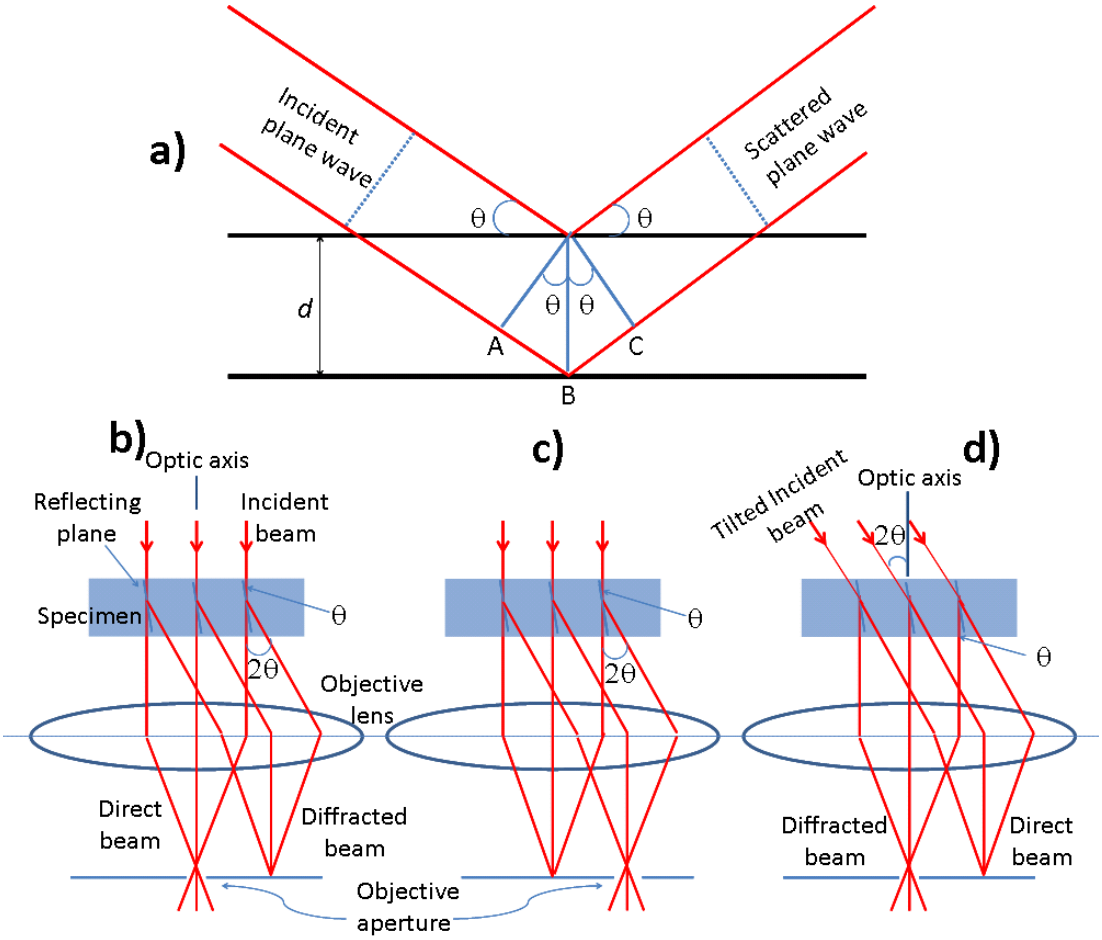

Figure 3.9: *a) The Bragg description of diffraction in terms of the reflection of a plane wave (wavelength λ) incident at an angle θ to atomic planes of spacing d. Ray diagrams showing how the objective lens and objective aperture are used in combination to produce (b) a BF image formed from the direct electron beam, (c) a displaced-aperture DF image formed with a specific off-axis scattered beam, and (d) a CDF image where the incident beam is tilted so that the scattered beam emerges on the optic axis [88].*

this assumption, what is known as Bragg's law is written as

$$2d_{hkl} \sin \theta_B = n\lambda \tag{3.3}$$

where reflecting hkl planes are a distance d apart, the incident and and reflected wave are at an angle θ_B. Monocrystals show distinguished dots in diffraction patterns, polycrystalline materials common centered circles and amorphous materials diffused circles. Using Selected Area Diffraction (SAD) in combination with Bragg's law, the interplanar spacing and the Bravais lattice (crystal group) of crystalline materials could be determined

Imaging in TEM could be formed with only those electrons that penetrate the specimen with out scattering. To allow this, an objective aperture (at the back of the focal plane) limits the scattering angle of the electrons scattered at the specimen ($1\,mrad$) and allows essentially only the direct beam to pass through. An image formed in this way is therefore called bright-field (BF) image. Since the scattered or diffracted electrons are excluded, any changes in the intensity of the transmitted beam due to inhomogeneities in the specimen with respect to density, thickness, and orientation create an image contrast [86]. Bright-field imaging provides a distinct image contrast available when scattered or diffracted beams are excluded by means of an objective lens. The dark-field (DF) image is generated not by the direct beam but the intensity of the diffracted or scattered electrons which can be achieved through tilting or objective aperture displacement. This is used for imaging specimen regions of specific orientation, structure or composition.

TEM has several types of operation mode like HRTEM (High Resolution TEM), STEM (Scanning TEM) and AEM (Analytical Electron Microscopy), etc. Apart from imaging of a material; measuring, modeling and manipulation of a sample can also be accomplished with a TEM. High resolution-TEM (HRTEM) and scanning-TEM (STEM) measurements are performed using Technai F30 STwin microscope (FEI company) operating at 300 kV. The composition was determined by EDX analysis in scanning transmission electron microscope (STEM) mode with a Si/Li detector (EDAX System).

3.3.2.1 HRTEM

The high resolution TEM is made possible by using a large diameter objective diaphragm that admits not only transmitted beam but at least one diffracted beam as well. All of the beams are passed by the objective aperture and made to combine in the image forming process. When viewed at high magnification, it is possible to see contrast in the image in the form of periodic fringes which they represent Bragg diffracting planes and are called phase contrast. With this method and proper high-voltage availability, spatial resolutions in excess 0.2 nm is possible. HRTEM is the ultimate tool in imaging defects. In favorable cases it shows directly a two-dimensional projection of the crystal with defects and all [85, 88].

3.4 Energy Dispersive X-Ray (EDX) Spectroscopy

In section 3.2.2, it was shown that the interaction of electron with a specimen produces various signals including characteristic X-rays. This happens in both SEM and TEM which both of them use energetic electron probes. Energy dispersive x-ray (EDX) spectroscopy utilizes the characteristic spectrum of X-rays that are emitted from the sample following excitation of an atom inner shell electron to a vacant higher energy level by the high energy electron beam. If both SEM and TEM are equipped with an EDX detector system, it is possible to get chemical information from the specimen. The detector is heart of EDX spectrometer which is a diode made from a silicon crystal with lithium ions diffused or drifted from one end to the matrix. Information about the elemental composition of the sample can be obtained, with the spatial resolution determined primarily by the probe size.

3.5 Electrical Measurement Setup

In this study, the main components used for the measurement of nano scale electrical currents are Source meter 2400, Picoampere meter 6485 and Electrometer 6517 all from Keithley instruments. Each of them have their own advantages.

Source meter can source the sample with various voltages and at the same time measure the corresponding electrical current. It doesn't need external power source for biasing the sample. Picoampere meter is advantageous interms of high time resolution measurements (30 ms) and this is found to be important during the characterization of fast UV sensors from ZnO nanostructures. Using Electrometer would be an advantage when the sample to be characterized possess huge electrical resistance. All the measurements were controlled through Labview that are programmed for various characterization techniques such I-V characterization or measurement of current at constant voltage.

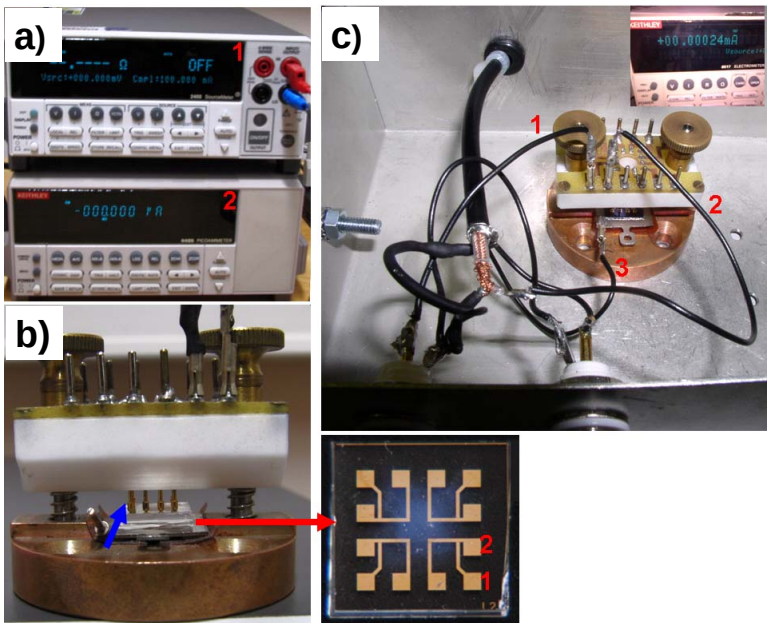

Figure 3.10: *a) Digital Images of electrical measuring instruments Source meter (1) and picoampere meter(2). b) Cheap holder with its gold pins (blue arrow) connected to contacts on quartz substrate. The right hand side image shown with red arrow shows the top views of the cheap where ZnO nanostructures are deposited (white contrast) for measurement and the numbers(1 and 2) shows the actual connections that correspond to cheap holder for electrical measurement. c) Depicts bottom gate NWFET set up inside a shielding metal box. In c) the numbers in red 1), 2) and 3) correspond to cables connections to source, drain and gate respectively. The measurement is done through electrometer shown in the inset.*

All measurements were performed in an ambient atmospheric condition ex-

cept the occasion where evacuation of a cooling chamber is performed during cooling the Al NWs and study the influence of temperature in electrical conductance. A two probe measurement connection was used in all of electrical measurements in this study. The reason is that the nanostructures have got very high resistance ($G\Omega$) as compared resistance of connecting wires (Ω) regime and no effect on the measurement result as the voltage drop in connecting wires is insignificant as compared to the voltage drop across the nanostructure device. The four probe conductivity measurement is useful for measurement of low resistance devices that are comparable to the resistance of connecting wires.

4 Device Fabrication Technologies

The synthesis technology involves the fabrication of chip integrated nanostructures which could be vertically or horizontally aligned with respect to the plane of the chip. The nanostructures fabrication procedure in this thesis begins mainly with the same processing step that starts with lithographic patterning of a photoresist. The summary of the initial stages of wafer processing technique for each type of synthesis is depicted in Figure 4.1: Once the lithographic patterning is successfully done, three possible routes can be followed depending on the final end of the desired nanostructure: Flame Transport Synthesis (FTS), Thermal Annealing Synthesis, and Thin Film Fracture (TFF). FTS could be of Crucible based FTS (C-FTS) or Burner based (B-FTS) technique. Each technique has its own unique approach and advantage providing cost effective, time efficient and less complicated processing as compared to other synthesis techniques such as VLS or electron beam lithography. The details will be discussed in the subsequent sections. Substrates such as Si and glass (quartz) are used. Results of from both types of substrate are discussed in Chapter 5 and 6.

4.1 Mask Deposition and Lithographic Patterning

Patterning of the sample starts with photo lithography on 356 - 406 μm thick, P/Boron <100> oriented Si chip that is coated with 100-300 nm thermally oxidized SiO_2 (mainly from Active Business Company GmbH, Germany). The wafer is cleaned sequentially, first in ultrasonic acetone bath followed by isopropanol cleaning and finally rinsing with deionized water. Isopropanol cleans acetone and the deionized water cleans isopropanol. The wafer will finally be ready to use after drying it with dry nitrogen. As depicted in Figure 4.1b), HMDS (Hexamethyldisiloxane) or $((CH_3)_3Si - NH - Si(CH_3)_3)$ which is a common primer in

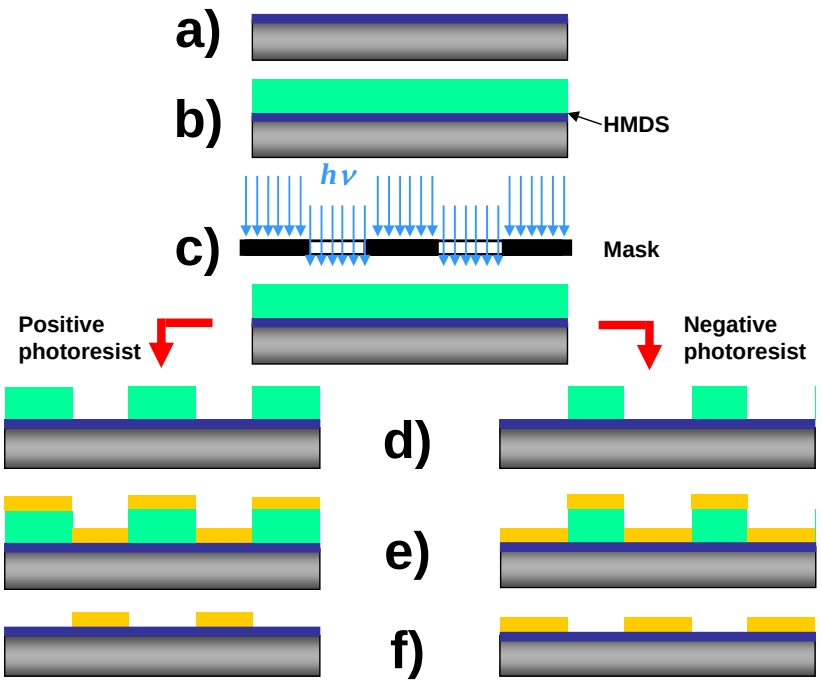

Figure 4.1: *Schematics of sequential steps in a typical optical lithography process for device fabrication a) cross-sectional view of prepared P^{++} doped Si substrate coated with SiO_2 (blue color). b) Adhesion promoter HMDS (Hexamethyldisiloxane) is introduced on the substrate. c) Aligned mask for exposure. d) Resist pattern after development ready for material deposition as shown in e). f) Mask lift-off in ultrasonic acetone bath results in patterned film.*

semiconductor & MEMS manufacturing industry, is used to promote adhesion. It is important to use adhesion promoters for an enhanced adhesion of resists specially on oxide surfaces. There is an active functional group (Si-NH-Si) in HDMS that reacts with the oxide surface in a process called silylation, and the substrate surface is rendered to be hydrophobic due to the methyl termination of the formed HMDS. This will lead to the formation of a strong bond to the surface [89, 90]. The process works not only on silicon dioxide but also on other oxides (e.g., Al_2O_3). HMDS polymer can be applied in two ways: liquid priming or vapor priming form. The vapor form priming is used before the substrate is spin coated with a photoresist and is more efficient than the liquid priming.

The two major resists that frequently used are AZ MiR 701(Micro Chemicals GmbH, Ulm Germany) and AZ 6612(Clariant GmbH, Wiesbaden Germany). For the synthesis of NWs fabricated in TFF approach, AZ MiR 701 resist is spin

coated at 8000 rpm providing an average thickness ranging from 800 to 900 nm after the photoresist development. Self-organized fractures can also be induced by using AZ 6612 resist and the details on the formation fractures will be discussed in the subsequent sections. The minimum thickness that can be achieved in using AZ 6612, however, is appr. 1.5 μm at 8000 rpm. This will result in higher shadowing effect for the deposited materials that are supposed to be inside cracks and reach to the substrate. This can cause broken NW or sometimes no NW deposition at all. One of the possible solutions is thinning resist through dilution with solvents such as PGMEA(propylene glycol monomethyl ether acetate). It is necessary to mention that the self-organized fractures are not only synthesized in silicon substrate, but also in thicker glass substrates (1.5 mm thick) with thicker photoresist. The nature of the fractures appear to be different as compared to the fractures synthesized in silicon wafers. The results are given in the following sections.

4.2 Thin Film Deposition

Chemical Vapor Deposition (CVD) and Physical Vapor Deposition (PVD) are the two useful and well established thin film deposition techniques. In general, CVD offers several advantages of which the three important ones are [91]: *I) Excellent step coverage, II) large throughput, and III) low-temperature processing.* PVD technique is based on the formation of vapor of the material to be deposited as a thin film. The material in solid form is either heated until *evaporation (thermal evaporation)* or atoms are knocked out from a target material by *accelerated ions (sputtering)*. In this work two kinds of PVD routes are followed for the deposition of NW material: Sputter deposition (intensively used) and Evaporation (rarely used).

One of the simplest and widely used PVD techniques is magnetron sputter deposition. The magnetron sputtering chamber and its assemblies are shown in Figure 4.2. The sputtering process begins first with the generation of ions by a plasma discharge usually within an inert gas (Argon). Utilizing the electric field which is established by a voltage drop, the inert-gas ions (Ar^+) are accelerated and the target is eroded by bombarding plasma ions that have energies close to

the external applied voltage (Figure 4.2c)). The escaping atoms are bonded to the substrate as they acquire high kinetic energy. Nearly all materials can be volatilized stoichiometrically through sputtering and the film deposition rate can be made uniform in large areas of a substrate [92]. It is also possible to bombard the sample with an ion beam from an external ion source which allows in varying the energy and intensity of ions reaching the target surface. Sputtering

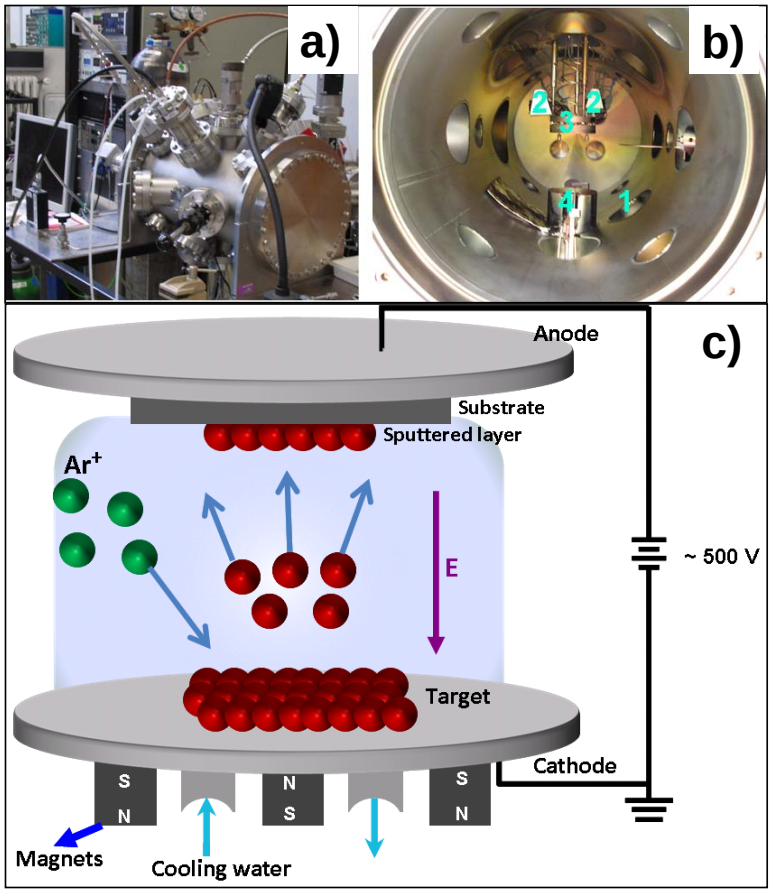

Figure 4.2: *. Digital image of typical custom made magnetron sputtering chamber : a) outer part and b) inner part. The inner part of the chamber in b) comprises important units such as 1) sputter source, 2) quartz crystal micro balance for thickness monitoring, 3) sample holder and 4) evaporation source. c) High velocity Argon ions (Ar^+) knocking out atoms from the target that diffuse through the plasma and depositing on the substrate.*

techniques could be of DC (diode), RF (radio frequency), magnetron, or reactive sputtering. Depending on the type of material to be sputtered and the required

sputtering rate, each techniques could be utilized for thin film deposition. RF sputter deposition for instance is good for insulating materials, since it avoids charge buildup in the target by alternating potential. Because a charge buildup over time in sputtering makes impossible to further bombard the surface. Frequencies above 50 kHz are used in RF sputtering. The sputter rate can also be increased by incorporating magnetron with DC or RF which is called magnetron sputtering.

In magnetron sputtering, the magnetic field from the magnets plays an important role controlling the thin film deposition process. It is the Lorentz force $\mathbf{F} = -\mathbf{e}(\mathbf{E} + \mathbf{v} \otimes \mathbf{B})$ that plays a role in trapping electrons in cycloid and confine them near the target to sustain plasma. The confinement of electrons near the cathode will increase the plasma density and makes the sputtering more efficient. This allows for higher sputter rate at lower Ar pressure, less heating of the substrate due to confined electrons on the target and increase in purity of deposited film as a result of less pressure. The custom made deposition chamber (Figure 4.2a-b)) is used for the deposition of Fe, Al, Ti, Au in DC mode and ZnO in RF mode. The chamber is first evacuated to $\approx 10^{-7}$ mbar followed by argon pressure close to 10^{-3} mbar and then ignition of plasma takes place for sputter deposition. The substrates all the time are under constant rotating condition when sputtering takes place in order to obtain homogeneous film deposition.

The sputter deposition machine (Ardenne CS 730 S) is one of the intensively used machine for deposition. The machine has the following features: consists of 3 chambers with 9 sputter sources, offers possibility of mounting 8 and 4 inch targets, deposition on 6 inch substrate, RF and DC sputtering up to 3 kW and etc. This machine has been used for the deposition of Au electrodes for B-FTS and C-FTS techniques. Besides being used as electrode, Au in C-FTS is also used as a catalytic agent for the growth of ZnO nanostructures. Au electrodes of thickness between 30 and 60 nm have been prepared on Si and quartz substrates. Since the adhesion of Au on Si and quartz is poor, adhesion promoters such as Cr and Ti are first deposited before the actual deposition of Au. The same machine has also been used for the deposition of Fe (in RF magnetron mode 200-400 Watt) for the synthesis of iron oxide NWs.

In industryies and many other application areas, evaporation is one of the

most commonly used type of PVD technique for deposition of thin film through thermal evaporation. In this study, this technique however is rarely used. The fundamental principle is that thermal energy is delivered to the source material through resistive heating (tungsten and tantalum wires) and atoms or molecules are evaporated to the substrate. Like the process in sputtering, the evaporation chamber is evacuated to the base pressure prior to evaporation process. A precursor material in a crucible is then heated inside a high vacuum chamber to a temperature which generates some vapor pressure. The vapor condenses and forms a thin film on the surface of a sample mounted upside down to the vapor source.

In both evaporation and magnetron sputtering depositions, the deposition process is controlled and monitored *in-situ* using quartz crystal control (conventional STM-100/MF) to provide real time deposition rate and to achieve the desired thickness. The basic working principle is that a quartz crystal, sandwiched between two metal electrodes is biased by alternating potential which induces vibration of quartz crystal at resonant frequency. For deposition monitoring, one electrode is exposed to vapor flux and proceeds to accumulate a mass of deposit that causes reduction in the resonant frequency of the crystal. Through comparison of the loaded resonant frequency to that of the reference resonant frequency, the thickness of the deposited mass is calculated. Detection of film weighing 10^{-8} g can be achieved through employing quartz crystal microbalance (QCM). The change in resonant frequency Δf is related to the change in mass Δm at the surface of the electrode by Sauerbeyt's equation given by [93]

$$\Delta f = -C_f \Delta m \tag{4.1}$$

where C_f is linear sensitivity factor of the crystal used. The increase in mass due to the additional deposition is treated though it was really increasing the thickness of the underlying quartz. The deposited film is considered to be rigid and very thin that it does not experience any shear forces during vibration. The thickness of the film can be calculated by:

$$d_f = \frac{\Delta m}{\rho_f} \tag{4.2}$$

where d_f and ρ_f are the thickness and the bulk density of the deposited film, respectively.

4.2.1 Modes of Thin Film Growth

The early stage of thin film growth begins with nucleation on the substrate. When substrates are exposed to vapors of a material, vapor atoms or molecules condense on a substrate and soon after a distribution of small but mobile clusters or islands are observed. The prior nuclei incorporate the impinging atoms and clusters and grow in size while island density rapidly saturates [94]. With a sequence of events or processes in the first few hundred angstroms, thin film growth takes place. The common competing events include adsorption, chemisorption, desorption, surface diffusion, nucleation, island growth and many other processes 4.3a).

During thin film growth, different atomistic processes may occur on the surface. Three distinct growth modes have been identified experimentally: Frank-van der Merwe (FV), Volmer-Weber (VW) and Stranski-Krastonov (SK). Figure 4.3(c-e) depicts the three modes of atomistic growth and these modes of growth can be better understood using Young's equation, where interfacial tension γ is identified by the subscripts f, s, and v representing film, substrate and vapor, respectively:

$$\gamma_{sv} = \gamma_{fs} + \gamma_{fv} cos\theta \tag{4.3}$$

The three modes of growth are displayed based on the wetting angle θ of a droplet on a substrate surface where a material have been deposited. For FV growth mode, the deposit wets the substrate completely, i.e., $\theta \approx 0$ and thus $\gamma_{sv} \geq \gamma_{fs} + \gamma_{fv}$. If γ_{fs} is neglected, the relation suggests that the island growth occurs when the surface tension of the film exceeds that of the substrate which is the reason why deposited metals tend to cluster up on ceramic or semiconductor substrate. In the case of island growth or VW mode, $\theta > 0$ and thus $\gamma_{sv} < \gamma_{fs} + \gamma_{fv}$. Lastly, the SK growth mode also called layer-island growth. In SK mode, initially at least, $\gamma_{sv} > \gamma_{fs} + \gamma_{fv}$ and wets the surface permitting nuclei to form above the initial layers. After the first few monolayers, subsequent layer growth is energetically unfavorable and islands are formed on top of this critical layer thicknes. Any factor that could disturb the monotonic decrease in binding

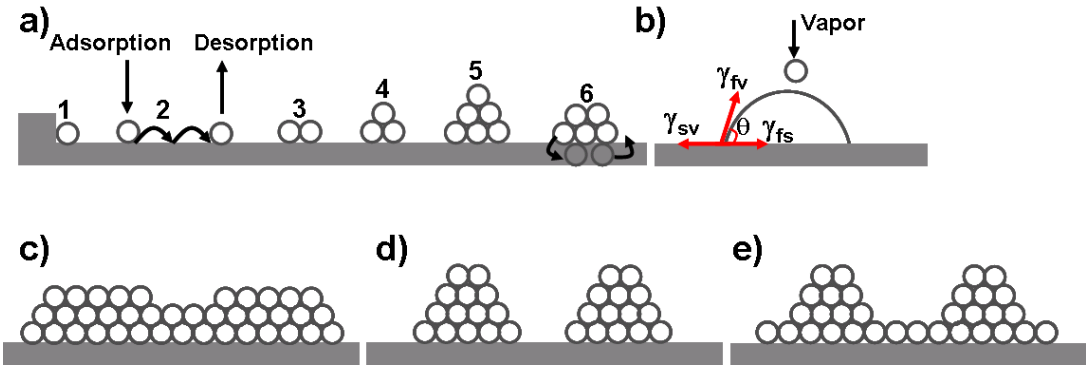

Figure 4.3: *Schematic illustration of a)processes and characteristic energies in nucleation and growth on surfaces. In the diagram represents different processes: 1) special sites atoms preferentially bind, 2) surface diffusion, 3) chemisorption, 4) Nucleation, 5) microstructure formation and 6) Interdiffusion. b) Depicts schematics of wetting angle of a nucleus that correlates with the modes of growth and surface to that of interfacial energy of deposit and substrate. Three thin film growth modes are identified: c) FV mode where atoms are strongly bound to the substrate than to each other favoring layer growh , d) VW mode where atoms are more bound to each other than to the substrate favoring island growth and e) SK mode where islands growth are favored after the growth of intermediate layer.*

energy characteristic of the layer may be the cause. Lattice mismatch or the discontinuity in the symmetry in the bulk crystal of the deposit, strain energy accumulates in the growing film. This results in a high free energy of the deposit intermediate-layer interface which triggers island formation [95, 96].

4.3 1D nanostructures Crystal Growth Methods

There have been different techniques developed so far for the growth of one dimensional nanostructures as they have got potentials for various device applications. The synthesis process of crystalline quasi-1D nanostructures could be categorized [97] into **I) Vapor Phase Synthesis** technique that includes *VLS growth, Oxide-assisted growth, Vapor-solid growth and Carbothermal reactions* **II) Solution Based Synthesis** technique comprising *Template-based synthesis, Solution-liquid-solid process and Solvothermal synthesis.* Besides this, one could

have a third category of nanostructure synthesis based on thermally driven diffusion,i.e. **III) Thermal Annealing of Substrates or Sputtered Deposited Thin Films**. The vapor phase synthesis technique is dependent on evaporation of the source material which later undergoes vapor phase reactions. The end result is a nanostructure as an elemental or oxide composition. In the following sections experimental results from category **I)** and **III)** are discussed based on literature review.

4.3.1 Vapor-Liquid-Solid (VLS) Mechanism of nanostructures growth

VLS or VS, is probably one of the Chemical Vapor Deposition (CVD) mechanisms which has been exhaustively used examined for understanding the growth of oxide nanostructures or NWs. The concept was first introduced by Wagner [30] to explain the mechanism for the growth of Si nanostructures. Nevertheless, this idea is widely used to understand the growth mechanism of 1D structures from many inorganic materials that include semiconductors (Si, Ge,B), II-V semiconductors (GaN, GaP, GAs, InP IAs), II-VI semiconductors (ZnS, ZnSe, CdS, CdSe)and metal oxide structures such as MgO and SnO_2 [98, 99]. In a VLS process, a chemical vapor (gas phase) is deposited on a catalyst alloy usually in liquid phase and ends up with the growth of nanostructures which is in a solid phase. For a controlled NW growth in VLS process, choosing the right catalyst and temperature are important points to be ensured so that there would be a coexistence of liquid alloy and solid NW material [22] as depicted in Figure 4.4b). Au is one of the commonly used catalytic material for nanostructure growth, however other materials such as Ti and Al [100] have been reported as well. The growth material is evaporated first, and then it forms a eutectic liquid alloy with the catalytic material [101]. When supersaturation is reached, there will be precipitation and growth of NWs at the interface between the substrate and the liquid alloy as shown in Figure 4.4c). In this mechanism, the catalytic particles leading the growth direction remain at the top of the NW. The schematic illustration in Figure 4.4d) shows the fact that the catalytic particle on the top of the NWs. The VLS concept of NW seems to be under strong debate. Some suggest that it is a VS process rather than a VLS process. The VLS or the

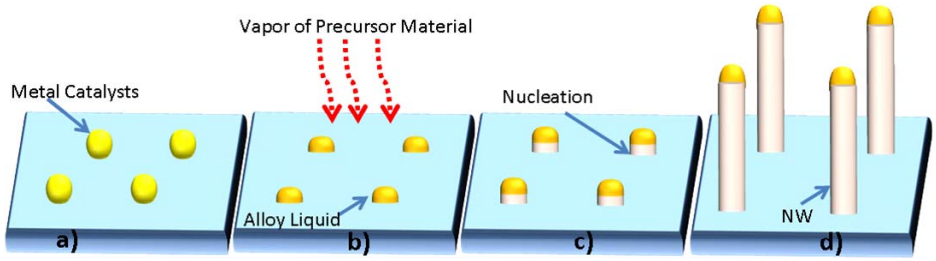

Figure 4.4: *Schematic illustration of catalyst assisted NW growth through VLS. Silicon or sapphire are typical examples for substrates that nanostructures grow. a)Metal catalysts such as gold or platinum are first deposited followed by b)heating to a desired temperature usually above the melting point of the catalyst. c) Nucleation starts after the supersaturation of the alloy is achieved and d)through further feeding of the growth material from the vapor phase [102], a long NW is achieved.*

VS method are typically utilized to grow vertically aligned nanostructures such as nanorods, nanosails and nanocombs. The growth process can be performed in a simple tube furnace equipped with a vacuum system and gas flow control. Possessing a very excellent metal oxide semiconductor properties with excellent physical properties [103], ZnO nanostructure is one of the highly investigated and synthesized through VLS technique. The synthesis of ZnO can be performed with the presence and with out the presence of catalytic particles (Figure 4.5e)). A catalytic free synthesis takes place through transportation and condensation of the vapor on the substrate by self catalyzing. As there is a direct conversion of vapor to solid on the substrate one calls such a process VS [97, 104] or which some people prefer to call it CVD [105] process. An interesting comparison of VLS and VS growth based on the experimental result on a single chip at different areas where, some areas posses catalytic Au particles and some others do not is given by Chang et al [106]. Nanorods were seen growing in a catalytic free area according to them. In VLS in general, through control of the nucleation and growth parameters, it possible to synthesize one-dimensional nanostructures of Zn, Sn [104] and other metal oxide. Furthermore, the starting precursor material could be Zn [107] or ZnO powder [22, 30, 108, 109]. When Zn is used as a source material, relatively lower temperature ($\approx 550\ ^{\circ}C$) is required to generate Zn vapor. The vapor is then oxidized by O_2 and led to the growth of ZnO nanostructures

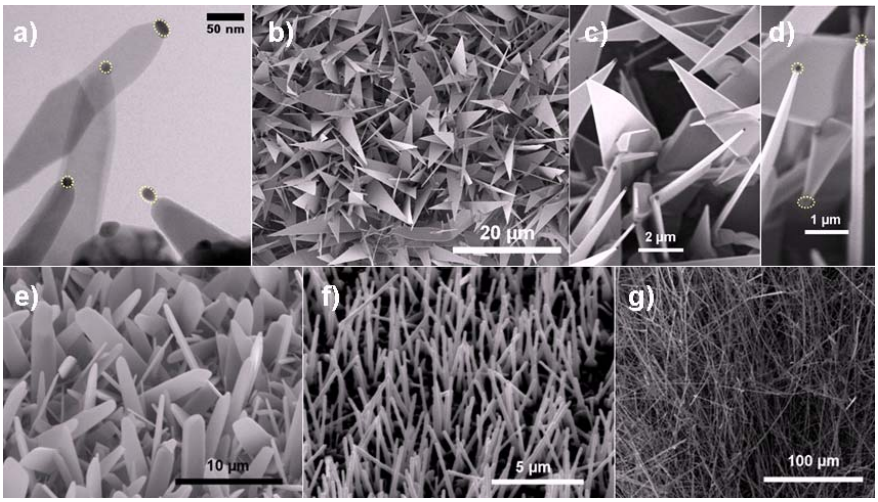

Figure 4.5: *(a-d) show nanostructures grown by conventional VLS approach, a) transmission electron microscope image of ZnO nanorods with Au NPs on their heads (inside dotted circles), b), c) and d) scanning electron microscopy (SEM) images ZnO nanosails at different magnifications. The presence of Au NP on the top of nanosail can be clearly seen in 1d (inside dotted circles). e) and f) show the structures grown by modified VLS approach [110, 111] without any catalytic NPs: e) ZnO nanomasts structures, f) ZnO nanorods, and g) tin oxide NWs.*

on the substrate. When ZnO is used as a source material, it will be mixed with other material such as graphite in order to reduce the vaporization temperature. Mixing ZnO with carbon powder, which is so-called carbon-thermal evaporation, can reduce the vaporization temperature from 1300 to 900 °C [31]. Heating the furnace above a critical temperature (>900 °C), the ZnO : graphite mixture is transformed into Zn and CO vapor (equation 4.4). The corresponding chemical reaction can be expressed as [112]:

$$ZnO_{(s)} + C_{(s)} \Rightarrow Zn_{(g)} + CO_{(g)} \tag{4.4}$$

After Zn vapor are formed, it is transported by the carrier gas (Oxygen and Ar mixture) to a substrate that has molten catalytic particles. Arriving to a substrate that is already at higher temperature than the eutectic melting point (Figure 4.6) of the precursor material (Zn) and catalytic particles (Au), Au-ZnO

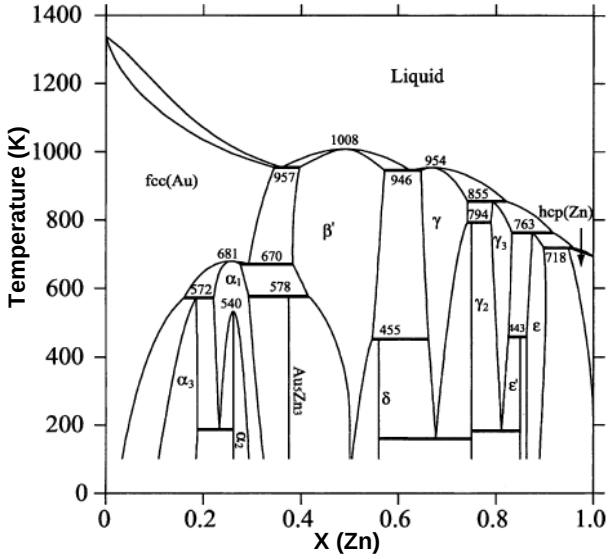

Figure 4.6: *Phase diagram of Au-Zn binary system [113]. Various eutectic alloy possibilities are given.*

liquid alloy droplet is formed utilizing O_2 from carrier gas. After supersaturation, the additional precursor material (ZnO) will continuously nucleate at the bottom of alloy-droplet and the droplet is lifted up due to capillary force that grows into one dimensional nanostructure. It is this tiny alloy that defines the growing NW structure. A typical TEM and SEM micrographs from the experimental result of ZnO synthesized through VLS process is given in Figure 4.5.

4.4 Techniques Optimized With in the Thesis

4.4.1 Flame Transport Synthesis (FTS)

Apart from the success of the conventional VLS process, several issues are still left undisclosed which motivated us to modify the VLS approach which is named FTS. Two variants of FTS are used for the synthesis of ZnO nanostructures: Burner based FTS (B-FTS) and Crucible based FTS (C-FTS). Figure 4.7 demonstrates the schematic flow process of both B-FTS and C-FTS approaches for synthesizing ZnO network nanostructures. Like other synthesis approaches used in this thesis, the initial stage involves micro structuring of a photoresist AZ MiR 701 using

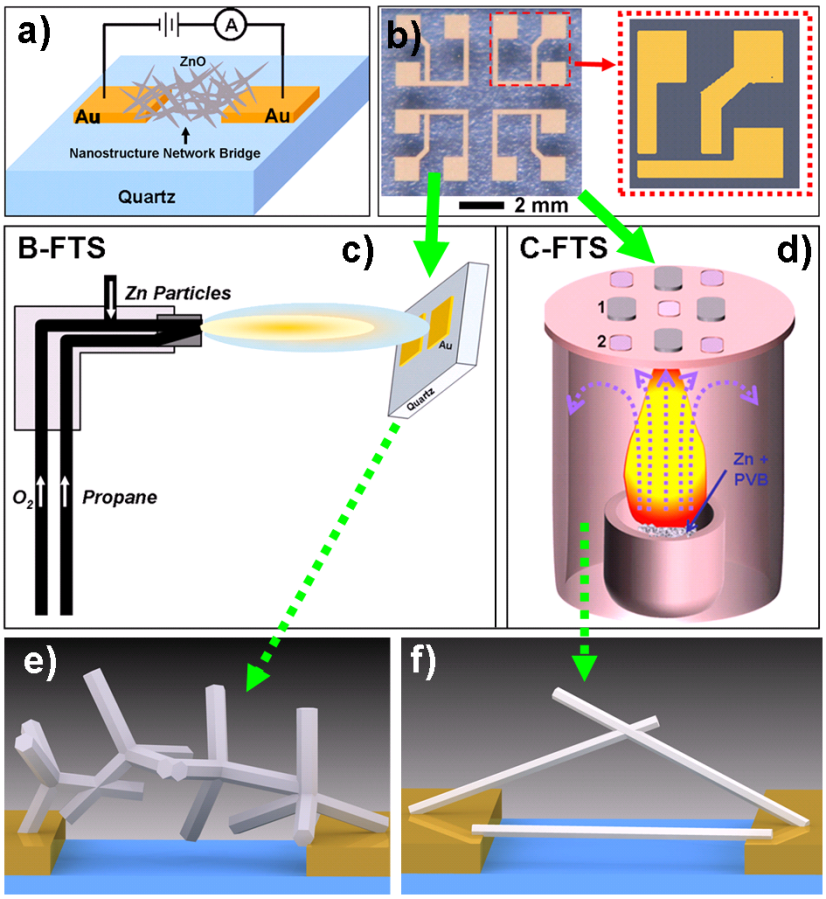

Figure 4.7: *a) Schematics of the final end photo-detection devices built from ZnO nano-microstructure networks fabricated by B-FTS or C-FTS approaches. b) Digital image of lithographically pre-patterned Au film on quartz substrate. The magnified region (on the right side in red dot lines) shows the presence of microscopic gaps* $(2-10\mu m)$ *between Au electrodes. c)Demonstrates B-FTS set-up: the Zn precursor microparticles are pumped into the flame via a pure oxygen jet which are transported and simultaneously transformed into ZnO nanostructures. d) Schematic illustration of C-FTS. The ceramic top cover has 9 exhaust holes for metal oxide vapor which is streaming from the crucible through the flame. The best and efficient arrangement for the catalytically assisted nanostructure growth is experimentally found through an arrangement where 5 holes (numbered 2) are left open and four holes (numbered 1) are covered with the catcher substrate. The samples are placed up side down where the microstructured gold faces the oxide vapor. Schematic illustrations in e) and f) shows ZnO nano-microstructure grown by B-FTS and C-FTS techniques, respectively. B-FTS mainly results in the growth of ZnO nanotetrapod bridging networks and C-FTS gives long needles forming the conducting path through the gap between two Au contacts on the chip [Gedamu et al., Adv. Mater 2013].*

conventional lithography. Chromium of 5 nm thickness as adhesion promoter and 35-100 nm gold film are consecutively magnetron sputtered on micro patterned resist. Successful experimental results have been obtained on quartz glass substrates (thickness 2 ± 0.3 mm, from GVB GmbH- Solutions in Glass, Germany) and Si substrates (356 - 406 μm thick, P/Boron <100> oriented Si chip that is coated with 100-300 nm thermally oxidized SiO_2 from Active Business Company GmbH, Germany).

B-FTS technique is one of FTS variant techniques that employs burner for the synthesis of nanostructures in a simple way just like painting a substrate with spray of molten oxide particles at ambient air condition. The experiment utilizes a single directional axial diffusion flame with oxygen jet feeding the flame besides enhancing the combustion of Zn particles (size 1-5 μm, Goodfellow GmbH, Bad Nauheim Germany). Oxygen ($\sim$2.5 bar pressure) and propane ($\sim$50 mbar) gases were inserted from two separate inlets. The Zn microparticles powder was homogeneously inserted in the third inlet by vibrating the inlet gently so that Zn is continuously feed through to the flame. The flame oxidizes and transports the feed through depositing nanostructured material on to the substrate. This approach is also called flame synthesis by some as it uses a flame for nanostructure forming particles. Single crystalline ZnO NWs with uniform diameters ranging from 25 to 400 nm directly synthesized on zinc-plated substrates as reported by Xu et al [114]. Using the same method single crystalline $WO_{2.9}$ NWs of diameters of 20-50 nm, length >10 μm are also reported grown directly on tungsten substrates [115]. Zheng and his group recently also recently studied intensively and synthesized various oxide nanostructures such as α-Fe_2O_3, CuO [116], WO_3 [117, 118] and many 1D complex oxide metal nanomaterials [119]. Obviously this synthesis method is rapid , done at ambient condition and controllable & scalable, resulting highly pure and crystalline materials applicable to diverse technologically relevant materials. Through using different precursor metal particles zinc, tin, zirconium and cerium, their corresponding oxide nanostructures could be synthesized. Apart from the versatility of large area coating, B-FTS approach can also be used for fabricating the patterns of 3D networks of metal oxide nanostructures in a 2D substrate.

In the case of C-FTS, the VLS approach is simplified through using simple muffle type of box furnace under ambient conditions rather than tube furnace

equipped with vacuum control. The basic principle in this approach is embedding metal microparticles such as Zn and Sn in a sacrificial polymer inside a crucible and heating it up at an ambient air. For the enhancement of burning and homogeneity of the slurry, ethanol could also be used. A 4 g mixture of 1:1 ratio of Zn to PVB in the crucible is heated to 950 °C for 4 hrs in an arrangement as depicted in Figure 4.7. C-FTS approach demonstrated that the synthesis of single crystalline metal oxide nanostructures could be produced with the presence or with out the presence of catalytic particles. The relative output as well as degree of freedom for synthesizing different nano-micro structures is higher in C-FTS approach. Catalytic gold is used in the synthesis so that preferential growths are obtained in lithographically patterned areas only. This will later allow for easy electrical measurement and analysis. Several 1D nano-micro structures and their mesoscopic network can be synthesized in a reproducible manner. A family of different structures have been found in a single growth processing step itself which could be an advantage for the device performance. In this work, the main focus is on a simple way to integrate such type of nanostructure into Si-chips and quartz substrate that have successfully been synthesized.

Figure 4.5e) to 4.5g) demonstrates the SEM morphologies of different nanostructures grown by C-FTS approach without using the catalytic gold nanoparticles. Nanomast type ZnO nanostructures were reproducibly grown by C-FTS approach and are shown in Figure 4.5e). Different types of vertical standing ZnO NWs (e.g., shown in Figure 4.5f)) are also grown on different substrates by using C-FTS technique. The working temperature in C-FTS technique varies from 800 °C to 1000 °C and more details about this are reported elsewhere [110]. In order to demonstrate the versatility of C-FTS approach, experiments on other nanostructure forming metals were also performed and successful results were obtained. For example Figure 5.12 shows the SEM image of SnO_2 NWs grown by C-FTS approach.

4.4.2 Thermal Annealing Method (TAM) for Iron Oxide nanostructures

In TAM, iron-oxide nanostructures are synthesized through annealing of sputter deposited Fe films in ambient air conditions. The annealing process could be

performed in a muffle type furnace or a hot plate. As mentioned in the beginning of this section, the very first step of sample processing is lithographic patterning of a substrate. Si chips of 356 - 406 μm thick, P/Boron <100> oriented, coated with 100-300 nm thermally oxidized SiO_2 are usually used. AZ MiR 701 photo resist is used to pattern the thin films. Once the desired patterns are fabricated, 10 nm Cr as adhesion promoter, 50 nm Au and 450 nm Fe are sputter deposited in a DC magnetron respectively. The aim of deposition of 50 nm Au is to use as an electrode during electrical conduction through iron oxide NWs bridging different size gaps defined by lithography as shown in Figure 4.8. After mask lift-off, the deposited multi-layer film is annealed at 300 °C on a hot plate or a muffle type furnace at an ambient air condition. A muffle type furnace has a 2.4 cm diameter hole from back that gives a limited access to the ambient air. This makes it different from a hot plate which the hot plate is completely open to ambient condition. In the subsequent sections, the results obtained using these methods and comparison to previously reported findings in the literature are also discussed. In the figure, it is not always observed that a controlled nanostructure bridged gaps although some gaps are slightly above 1 μm size. Thus for obvious reason one has to find a way so that nanostructure bridged gaps could be formed for further electrical measurement to further develop as a sensor. Out of many experiments and processing, however, it was found that iron oxide bridged gaps could be formed through a successive process of buckling and collapsing of the buckles. This was the case when microstructured iron film was annealed in a hot plate. The SEM, TEM and electrical measurement results are given in Chapter 6.

4.4.3 Thin Film Fracture (TFF) Approach for Horizontal NW Synthesis

When thin films are subjected to stress various phenomena such as buckling, delamination, fracturing and etc., can occur. The direct creation of NWs on flat silicon substrates that can be combined with silicon processing techniques like electrochemical [81] or a fracture approach was developed independently by two groups [44, 120]. The result from later group was mainly optimized not only for the integration into silicon chips [45–47] by using photoresist fracture, but also

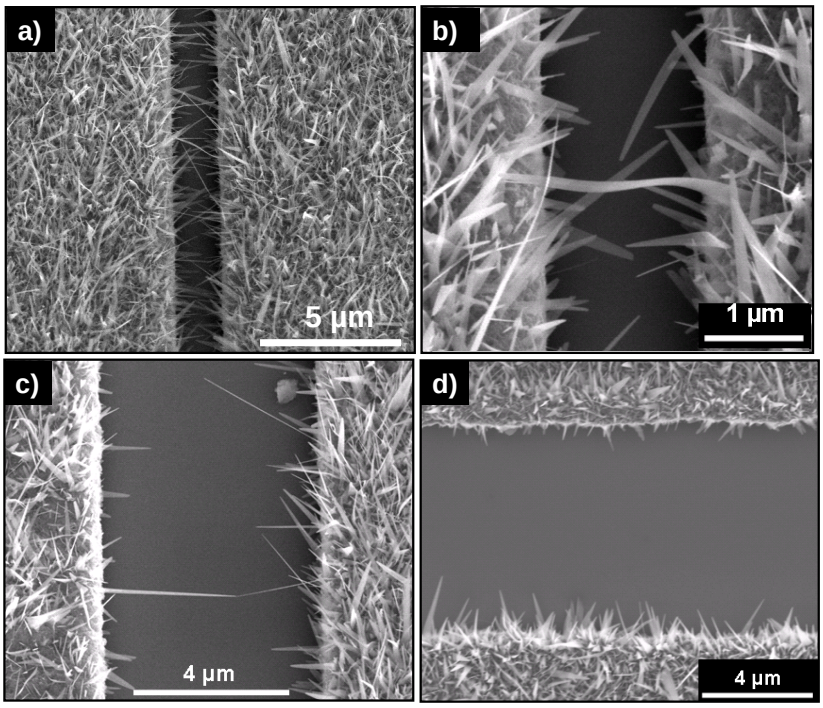

Figure 4.8: *a) Sample SEM image lithographically microstructured gap is bridged with few number of iron oxide nanostructures. b) shows magnified part of the same sample in a). c) SEM micrograph of another gap of the same specimen where very rare of the nanostructures are bridging the gap. This is the usual result obtained in many of other specimens where there is rarely connecting gaps. d) Very short nanostructures with 0 % bridged gap.*

to be used without a lithography lab by just utilizing shadow masks in vacuum deposition processes. Advantages of this method are the direct connection of the NW with macroscopic contacts on the chip, the flexibility in the utilized material as all materials are accessible through vacuum deposition techniques such as magnetron sputter deposition or thermal evaporation. The main steps involved in thin film fracture (TFF) approach are depicted in Figure 4.10. The photoresist is deposited (thickness varying from 550 nm to 1.5 μm) on the Si wafer which acts as a shadow mask. The Si wafer with photoresist mask undergoes thermal cycling for fracture (crack) formation. The wafer is initially heated on the hot plate ($\approx$323 K to 348 K) and then it is subjected to quenching for about 5 seconds to a cryogenic temperature ($\approx$77 K) using liquid nitrogen. The quenching process is not done in a single immersion step, but through three intermittent steps until

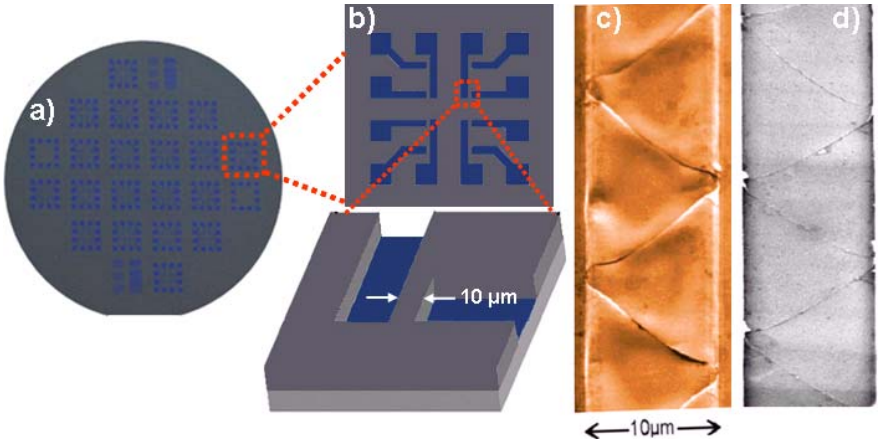

Figure 4.9: *a) Optical micrography of a wafer after it is lithographically patterned. b) Sketch of individual chip pattern. Each of the chips contain several positions where 200 µm long and 10 µm wide photoresist strips (arrowed) are located. Each of these chips undergo thermal fracturing. c) SEM image of a part of the fractured photoresist strip [47]. d) SEM image after metal deposition and mask lift off, the moulds are converted to microcontact lines on the left and right, and the cracks are converted to NWs, connected to these microcontact lines.*

the sample is completely quenched in the 3rd immersion step. The complete quenching is confirmed where no more bubbles are observed after thermodynamic equilibrium is reached. As the result of difference in the coefficient of thermal expansion between the resist and the substrate, the drastic temperature change creates a thermal shock leading to a mechanical failure which results in nanoscopic fractures everywhere on the resist but most importantly on a 10 μm by 200 μm wide resist strip where $\approx$ 22 well organized zig-zag fractures are obtained. The fracturing of thin films can be determined by strain fields which depends on the design of the film that can be chosen intentionally to create predefined crack patterns. If films are too thin (below 400 nm), the strain developed on the film may not be enough to induce the fracture and can yield almost no cracks on the resist, whereas if films are too thick (above 1,000 nm), the risk for uncontrolled delamination is very high and also the cracks may not be able to reach down to the substrate. Depending on the thickness of the resist, width of resist strips and substrate used different shapes of cracks are observed. Cracks of λ shaped (Figure 4.12), straight but zig-zag shaped, bow shaped but still zig-zag and some

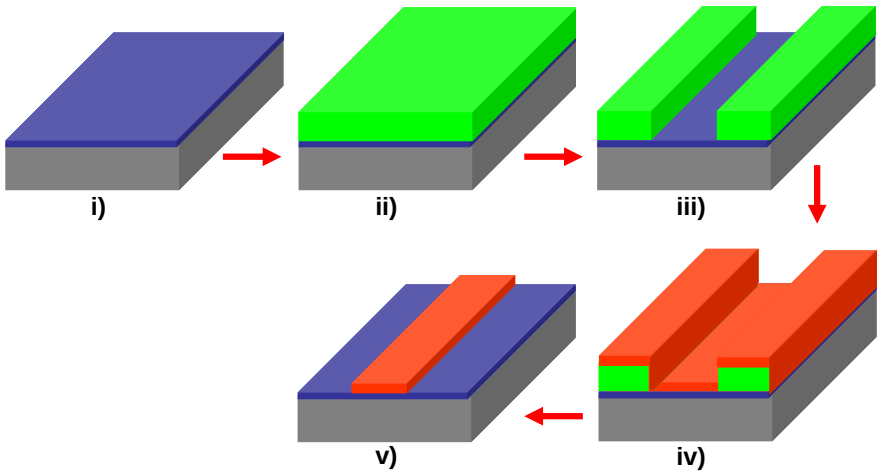

Figure 4.10: *Schematics of processing steps in fabricating the NWs by thin film fracture approach. (i) Ready made chip of Si Substrate with SiO_2 layer on top(blue color). (ii) Photoresist deposition. (iii) The microstuctured photoresist under goes a crack generation. It is first annealed to a temperature of 50-75 °C for about 5 to 10 minutes and quenched in liquid nitrogen. (iv) Deposition of NW material. The cracks and photoresist are fully covered with the deposited material. (v) Schematics of NW material after mask lift-off with ultrasonic acetone bath.*

times straight that cut the strip perpendicularly instead of a zig-zag tendency have also been observed.

4.4.3.1 Factors Influencing Fractures

As shown in Figure 4.11, a bow shaped fractures are produced when the photoresist thickness is approximately larger than 1 μm and the gaps are between 8 to 10 μm. The cracking behavior is also studied under change of parameters, substrate and resist conditions. The exact position of individual fractures can be precisely controlled, if they are confined by the lithographically produced microstructures. Depending on the thickness of the photoresist, cracks can propagate in straight line or follow curved paths or even some times lambda shaped cracks can be formed in the lithographically confined position. The process has been performed at a wafer level and the reproducibility has been proved for at least thousands of wafers. The formation of cracks with respect to the thickness

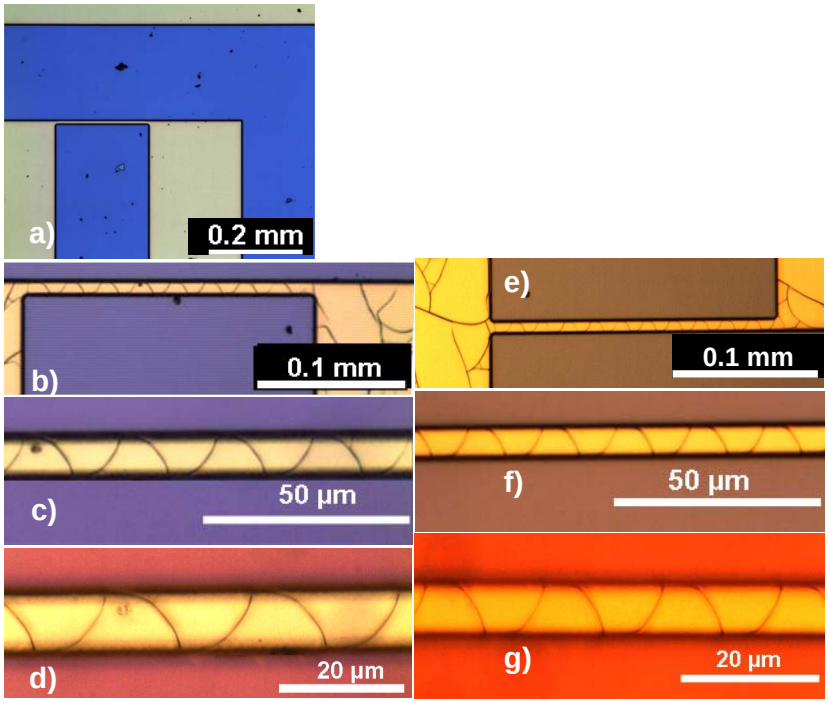

Figure 4.11: *a) Optical image of a lithographically structured sample before fracturing where 200 µm long and 10 µm wide photoresist strips are located. b) Optical micrograph after fracturing of 1.48 µm thick AZ 6612 photoresist showing bow shaped fractures. Images in c) and d) are higher magnification images of (b). e) Optical micrographs of a fractured sample that has the same resist but a thickness of 1.29 µm. f) and g) are magnified versions of image (e). The bending of fractures appears to increase when the resist thickness is increased as can be compared seen for instance in (d) and (g).*

of photoresist and influence of oxygen plasma treatment are summarized in Table 4.1. The treatment with oxygen plasma (ion) is a standard method to reduce the resist thickness. In this case, however, it negatively influences the TFF approach as it results no fractures which might be due to more branching in the polymer chains of the photoresist. Plasma treatment could enhance the cross-linking and entangling of the polymer chains which makes the bonds to be stiff for fracturing. Thus any oxygen plasma treatment will result in a more stiff photoresist which was the main reason to avoid the plasma etching of the resist if cracks ar desired. It has been clearly observed that when the thickness of photoresist is less than 550 nm, crack formation probability is less than 50%. With increase in thickness from 550 nm to 600 nm, the crack formation probability increases upto 75%.

With photoresist thickness in the range of 650 nm to 850 nm, crack formation probability reaches maximum value. Individual cracks appear to be straight but the overall orientation of cracks of being zig-zag. Some times bow-shaped cracks are also formed usually above 700 nm thickness. It appears that critical value of photoresist thickness lies on average 750 nm since the crack formation probability is 100% and with further increase in thickness beyond 750 nm, crack probability is maximum and different shapes of cracks are formed. If the width of the resist is less than 10 μm size, cracks of various shape and orientation could be the result.

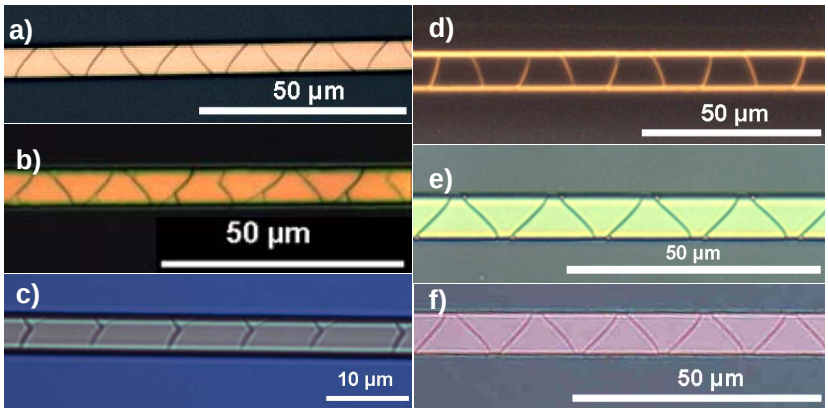

Figure 4.12: *Optical micrographs of variety of fracture shapes obtained from different resists, size of resist strip, substrate conditions and temperature differences: a) depicts fracture resulted from AZ MiR 701 resist 8 µm wide strip that has a thickness of 740 nm treated for about 10 min at 55 °C temperature. b) The same resist and condition as in (a) but a resist thickness of 850 nm and 10 µm wide strip c) AZ MiR 701 resist of thickness 850 nm, but narrow resist strip of width 5 µm. d) depicts fractures resulted from AZ 6612 photoresist on aluminum anodized surface on glass substrate: thickness of photoresist 1.43 µm, annealed at 53 °C for about 10 min. e) depicts fractures from Shipley 1813 photoresist having a 650 nm thickness and 10 µm wide photoresist strip annealed at 75 °C for about 10 minutes f) fractures from AZ MiR 701 resist diluted with propylene glycol monomethyl ether acetate (PGMEA) and having a 550 nm thickness annealed at 65 °C for about 15 minutes.*

Following fracture formation is deposition, as shown in step ***(iv)*** of Figure 4.10. The material of interest as a NW is then deposited over the entire area of the wafer with fractured resist. Finally, this wafer is again undergoes to mask

Table 4.1: *Summary of the TFF approach: Success statistics for a 10 µm sized gap width of resist. From approximately 100 chips, 80 were fabricated with a 100% success rate at the optimized photoresist thickness between 850-1200 nm.*

Thickness of resist film	**As prepared crack formation**	**Crack formation after oxygen plasma etching**
$\leq$ 550 nm	$<$ 50%	0%
600 nm	75%	0%
650-850 nm	100 %	0%
850-1200 nm	100 % bowshaped cracks	0%
$\geq$ 1200 nm	100 % bow shaped and strongly bended cracks accompanied with delamination of a resist	0%

lift-off process using ultrasonic acetone bath which allows the lifting of the whole photoresist from the wafer. The undesired material covering the top of photoresist is also lifted off together with the resist leaving behind the NWs within the cracks. The photoresists are mainly two types (i) positive and (ii) negative and depending upon the requirement, a particular photoresist can be used. Till now desired cracks are successfully produced in controlled manner using a positive photoresist, but experiments about the utility of negative photoresist have shown possibilities of their usage.

A photoresist thinning has also been experimented through the dilution of photoresist with the right solvent. The reason for thinning resists is to overcome the problem paused by resist thickness during thin film deposition. Depending on the resist thickness, width of crack opening and the width of the shadow mask, the amount deposited as a NW material is affected or it could be used to tune the NW dimension. The higher the thickness of the resist, the less probable is the deposited material reaching to the bottom substrate, which causes either no or broken NW synthesis. Figure 4.12f) shows straight and zig-zag fractures achieved through dilution of AZ MiR 701 resist (from MicroChemicals) using propylene glycol monomethyl ether acetate (PGMEA) solvent (99.5% from Sigma- Aldrich). An optimal dilution should also be done which if not fractures would not be produced when resist thickness is below 500 nm. In room temperature, the density of the resist as well as the PGMEA was measured with a formula: $\rho_{AZMiR701} = m/V = 1025\ kg/m^3$. Similarly the density of PGMEA is

determined $\rho_{PGMEA} = 800\ kg/m^3$. 1:0.5 resist to PGMEA ratio with the spin speed of 2000 rpm resulted in a thickness of 500-550 nm. Table 4.2 summarizes

Table 4.2: *Summary of spin coating speed relationship to thickness of diluted photoresist.*

Spin coater speed (rpm)	Thickness of resist(nm)
8000	400
4000	441-476
2000	500-550
1000	800-820

the relationship between spin coater rotation speed to film thickness for diluted MiR 701 resist to PGMEA in a ratio of 1:0.5. Depending on the type of crack desired, one can tune the speed and control the cracks produced.

4.4.3.2 Mechanism of Fractures in Bi-Layered Thin Films

Experimental results in the section above showed that a thin film (PMMA based photoresist) on Si substrate under thermal strain resulted in an intriguing zig-zag oriented fractures. As the SEM micrography in Figure 4.9c) shows, the fracture is believed to be buckle driven delamination subsequently followed by cracking. Residual stresses are one of the contributers for cracking in thin films of metals, ceramics and polymers [121]. The origin of these stresses arise from a mismatch strain field which is caused during constant temperature growth by defects annihilation, epitaxy, phase transition, and new material growing into grain boundaries in the film [122]. As the substrate is much thicker than the film, one can assume a uniform biaxial stress will be acting on the plane of the film only. Under such assumptions, the substrate will be set to stress free. With such conditions, one could predict, characterize and evaluate the fracture properties of thin film resists from biaxial thermal compression when dipping the sample into liquid nitrogen. Consider Figure 4.13a) that has thick substrate and very thin film on the top under stress. The magnitude of thermal strain ε_T developed in the film when its temperature reduced from T_0 (330 K) to T (77 K) that differs from the thick substrate is given by

$$\varepsilon_T = \int_{T_0}^{T} (\alpha_f - \alpha_s) dT \tag{4.5}$$

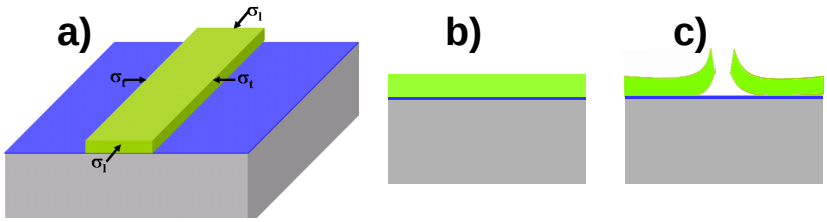

Figure 4.13: *Schematics showing a) a 3 d imaging thin film on thicker substrate under a biaxial compression action. b) Cross-sectional view of the thin film which is an elastic strip clamped along both sides. c) The application of biaxial stresses leads to a telephone cord buckling as shown by Audoly et al. [123], delamination and subsequent failure (fracture) at a critical stress.*

where α_f and α_s are the thermal expansion coefficients of the film and the substrate. This is the thermal strain on the film as a result of thermal misfit. This mismatch strain, Equation 4.5, needs to be accommodated by elastic and inelastic deformation in the film. The corresponding biaxial misfit stress is

$$\sigma_T = \frac{E_f \varepsilon_T}{1 - \nu_f} \tag{4.6}$$

which is Stoney's formula and E_f is the Young's modulus of the film and ν_f is the Poisson's ratio of the film and the quantity $\frac{E_f}{1-\nu_f}$ often is called the biaxial modulus. The compression applied on the edges of the film has a destabilizing effect. To recover its natural length, the film tends to buckle away from its rest plane and bends. Buckling therefore results from a balance between the release of the in-plane compression energy and a gain of bending energy [123, 124]. Under compression, thin films buckle, delaminate from the substrate, and fracture when buckling stress exceeds film fracture stress [125]. The strain energy release rate of a crack G regardless of the stress sign is [121, 126]:

$$G = Z(\alpha, \beta) \frac{\sigma_f^2 h_f}{\overline{E}_f} \tag{4.7}$$

where σ_f is the stress in the film, h_f is the film thickness, $\overline{E}_f = \frac{E_f}{(1-\nu_f^2)}$, E_f is the modulus of elasticity, and the dimensionless coefficient $Z(\alpha, \beta)$ depends on the elastic mismatch between the film and the substrate, through the Dundurs

parameters [121, 127]. Thin film fracture or delamination is observed when the strain energy release rate exceeds the film (G_f) or the interfacial (G_I) toughness, respectively ($G > G_f$, or $G > G_I$) [128]. One can avoid these types of fracturing or delamination by either reducing the film thickness, or the stress. The film thickness can easily be controlled so that one can either induce of thin film fracture or avoid it by manipulating the film thickness. However, as the aim here is fabricating fractures, a variety of self-organized cracks have been produced through controlling the thickness of the resist film, width of the strip, and temperature.

5 Semiconductor NW and Nanostructures for Sensor Applications

This chapter shows results from metal oxide semiconductor NWs and nanostructures integrated in a microchip and their promising applications as a UV photodetector and gas sensor devices. Two synthesis routes namely, TFF and FTS approaches are successfully employed to fabricate devices. In section 5.1, the synthesis of horizontal ZnO NWs from TFF approach are demonstrated. More over photocurrent measurements and a UV assisted oxygen gas sensing of the NWs are presented. In section 5.2, results of ZnO network nanostructures synthesized using FTS (B-FTS & C-FTS) technique are given. The SEM and electrical conductance measurements besides its photo detecting ability are demonstrated and investigated. Finally preliminary results of chip integrated SnO_2 nanostructures (Figure 5.12) from C-FTS synthesized specimen are given and proved the versatility of the C-FTS synthesis method. Summary of all results are also briefly discussed and given 5.3.

5.1 ZnO NW Synthesized in TFF Approach

As already mentioned in the previous chapter, the next step after the synthesis of cracks is deposition of the NW material. As a ceramic semiconductor, ZnO is sputter deposited from a sputter target in RF sputtering technique. The chamber is first evacuated to a pressure of 10^{-6} mbar. The ZnO film and NW sputtered are then deposited on Si substrate at 40 Watt, 10^{-3} mbar argon pressure and as deposited, both showed electrically insulating behavior. However, after annealing

the prepared NW samples above 400 °C for about 1 hour in ambient atmosphere, electrical conductance is observed which is a clear indication of microstructural change. The correlation between annealing conditions and the physical structure of the films (crystalline structure and microstructure) was investigated by X-ray diffraction (XRD)and atomic force microscopy (AFM). The XRD results on the annealed film showed a c-axis preferred orientation which is preferred growth direction of ZnO because of its hexagonal wurtzite crystal structure. Sputtering of low layer thickness or small amount of semiconductors like ZnO is believed to come up with columnar Volmer Weber-type of growth or separate islands (details in section 4.2.1). The AFM image shows that the as-deposited ZnO film is quite rough which is modeled by the schematic Figure 5.1a) with a columnar microstructural growth with possible spacing among columns. Post deposition

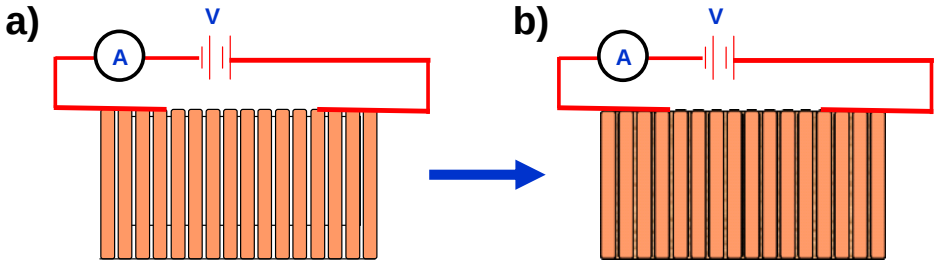

Figure 5.1: *Schematic illustration of ZnO thin film before (a) and after annealing (b). A columnar growth in ZnO can result a non-interconnected island and annealing for 1 hour in ambient condition causes interconnection between island that can offer path for electron conduction*

annealing resulted in remarkable changes in the microstructure as shown in the schematic Figure 5.1b). The film has been found to be dense and more homogeneous besides a few hillocks on some areas. This annealed film is found to be electrically conductive by interconnected islands as schematically depicted in the microstructure cross-sectional view. In relation to microstructural and quality of the film, similar results have been reported by Zhang [129] and Chu et al [130]. They showed that the electrical resistivity increases by more than three orders of magnitude after annealing. This seems to contradict the here found experimental result where both the ZnO film and NW are found to be conductive only after annealing. The electrical conductance curves before and after annealing of NWs are shown in Figure 5.2a). The conductivity in the polycrystalline sputter

deposited NWs can be as low as few nA. Even if the wires appear to have a diameter of 100 nm or more, the low current is most likely be explained by nanoscopic junctions between the polycrystalline facets which might be effectively only a few nanometers wide. The UV photodetection of the ZnO nanostructures fabricated

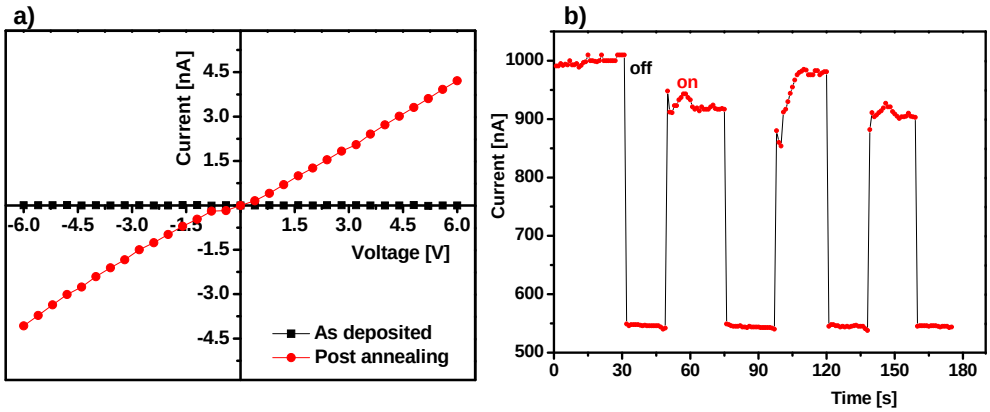

Figure 5.2: *a) Electrical conductance of as deposited and annealed (at 400 °C for about 1 hr in air) 50 nm nominal thickness ZnO NW. b) Current-time switching cycles curve at constant bias of 2 V under UV illumination.*

under TFF approach is measured under ambient conditions. It is well known that when ZnO nanostructures are exposed to an environment containing oxygen, oxygen will be chemisorbed on the surface as illustrated in the model Figure 5.3. As the NWs possess high surface area to volume ratio, the adsorbed oxygen would govern surface states and trap electron or holes generated in the NW that drastically changes the conductance. This model of explanation is not new as there exist already many reports [131–135] studying influence of oxygen on surface states which will in turn influence specially the photocurrent in ZnO thin films and NWs. The capture of electrons O_2 from n-type ZnO in dark current condition for instance can be put as

$$O_2 + e^- \rightarrow O_2^- \tag{5.1}$$

When the NW is exposed to UV-light at an ambient condition, photons of energy greater than the bandgap will generate electron-hole pairs. The generated holes then migrate to the surface and make surface recombination to electrons of the

adsorbed oxygen ions as given in equation 5.2

$$O_2^- + h^+ \rightarrow O_2 \tag{5.2}$$

Typical experimental illustrations are given for instance upon illumination of ZnO NWs with 365 nm UV lamp. The ZnO NWs conductance has increased as it is evidenced by the current versus time characteristics at a constant voltage supply. The oxygen molecules, adsorbed on the surface of ZnO NWs act as electron acceptors and capture the free electrons present in the n-type ZnO semiconductor to form O^{-2} [136]. The depletion layer formed by these oxygen chemisorptions near the surface results in the reduction of the channel conductance. The normal I-V

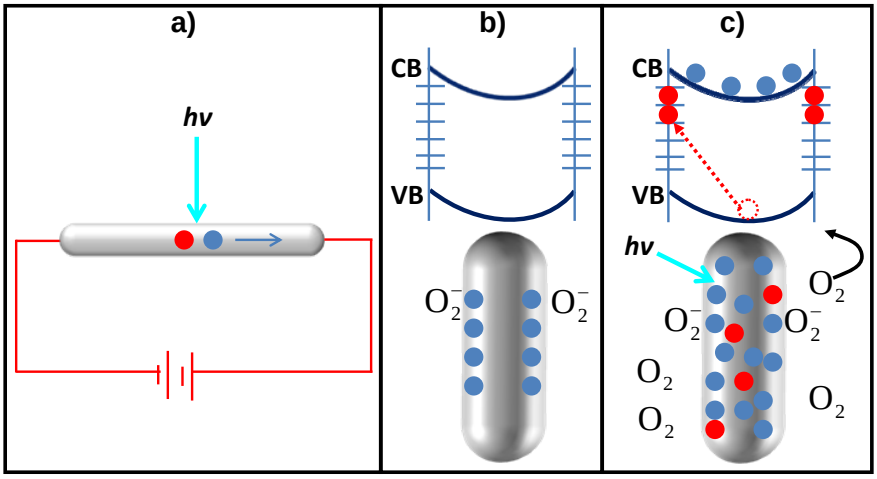

Figure 5.3: *Schematic of a NW photoconductor: a)Upon illumination with photon energy above E_g, electron-hole pairs are generated and holes are readily trapped at the surface. b) and c) show trapping and photoconduction mechanism in ZnO NWs respectively: the top drawing in b) shows the schematics of the energy band diagrams of a NW in dark, indicating band-bending and surface trap states. VB and CB are the valence and conduction bands respectively. The bottom drawing shows oxygen molecules adsorbed at the NW surface that capture the free electron present in the n-type semiconductor forming a low-conductivity depletion layer near the surface. c) Under UV illumination, photogenerated holes migrate to the surface and are trapped, leaving behind unpaired electrons in the NW that contribute to the photocurrent. In ZnO NWs, the lifetime of the unpaired electrons is further increased by oxygen molecules desorption from the surface when holes neutralize the oxygen ions [137].*

responses and current switching in the ZnO NWs synthesized through TFF are

demonstrated in Figures 5.2. According to Soci et al., [137] the photogenerated holes migrate to the surface and are trapped, leaving behind unpaired electrons in the NW that contribute to the photocurrent. The holes then neutralize the chemisorbed oxygen resulting in increased conductivity as shown in Figures 5.2b). When the UV light is turned on and off, the increase or decrease in photocurrent takes a time to reach to the saturation. This phenomenon is more pronounced in the case of ZnO nanostructures synthesized by C-FTS approach. The photoresponse of TFF grown ZnO NWs at constant 2 V applied voltage and under UV illumination show a photoresponse which is much faster than ZnO nanostructures grown by C-FTS counterpart as shown in the next section.
Besides the photo response of ZnO NWs fabricated in TFF approach, measurements for UV-assisted conductance change in gas atmosphere are also conducted. Figure 5.4 shows the average UV-assisted conductance change when a ZnO NW is exposed to different O_2 partial pressures. The as deposited ZnO film tends to

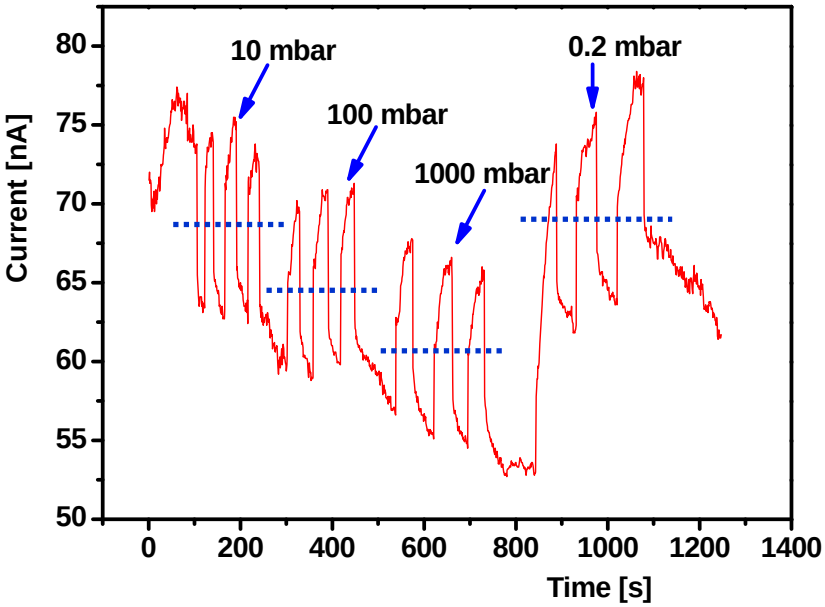

Figure 5.4: *Electric current measured at 4V for 60 nm ZnO NWs under room temperature and different oxygen pressures. Oscillation is induced by switching UV light on and off. The dashed bars guide the eye to the average currents at the different partial pressures.*

show many point defects such as oxygen vacancies, zinc interstitial, etc., which in general affect the conduction mechanism in most metal oxides based semiconductors. Conductivity mainly depends on electron hopping from intrinsic defects in

the oxide film which are related to the oxygen vacancies generated during growth [138]. Higher concentration of oxygen vacancies will result in higher conductance. The measurement shows that the I-V or the current at constant voltage which is not influenced by the oxygen gas atmosphere. To enhance the sensitivity, the device has been illuminated with a UV light (365 nm). When these NWs are exposed to UV light at an ambient condition, the NW reversibly and rapidly switched ON and OFF conductivity states as shown in Figure 5.4. The reason is that oxygen molecules from the the O_2 atmosphere are desorbed on the NW forming oxygen ions and cause a band bending as already mentioned above. As a result, there is no direct path for flow of electrons during illumination resulting in slow increase in conductance. Similarly under dark current condition (UV is off), the electrons and holes cannot recombine directly. This also does not allow a direct path for electron-hole recombination and thus resulting in a slow decay.

5.2 Properties ZnO nanostructure Networks Fabricated Through FTS

The ZnO nano-microstructures used in current UV photodetection studies were grown directly on the Si and quartz chips using B-FTS and C-FTS approaches as presented in Figure 5.5. Figure 5.5a) shows the SEM image of the ZnO deposited on the patterned chip using B-FTS approach. A digital image of the chip (B-FTS grown) is shown in inset of Figure 5.5a), where a clear contrast is visible between ZnO deposited area and the pre-patterned Au electrodes on quartz substrate. As seen from Figure 5.5a)-b), nanotetrapod shaped ZnO material was grown by B-FTS directly on the gap between two Au electrodes. The dimensions of the B-FTS ZnO nanotetrapod morphology are in nanoscale regime (arm thickness $\sim$30 - 100 nm and its lengths vary from 100 - 500 nm). The growth rate across the length of the tetrapod's arm is estimated to be in the $\mu m/s$ regime, since the time of flight in the flame is less than 200 ms [139]. Literature review shows that the growth rates range from 3.3 nm/s [140] to 33.3 nm/s [141] for ZnO structures. It seems that at preliminary stage within the flame, growth rate of tetrapods is much higher as compared to later stage when these nano & mico sized tetrapods are deposited on the substrate but upto some extent growth still remains con-

tinue which enables interpenetration between tetrapod arms [139]. It was found that ZnO nanotetrapods forms a bridging network across the gap on the chip by interconnecting tetrapods arms in form nanojunctions directly during fabrication process. At the same time, the nanojunctions between nanotetrapods provide a mechanical support to the networks bridging gap between the two Au electrodes and also establish a continuous path for electrons flow through it. Figure 5.5c) presents overall I-V characteristics of the B-FTS synthesized nanotetrapod bridging network device when UV light ($\sim$ 15 $mW.cm^{-2}$) is switched on/off. From these data it can be concluded that the electrical conductance changes more than two orders of magnitude under UV illumination. Moreover, it can be concluded from Figure 5.5c) that two Schottky contacts are formed between ZnO nanotetrapods and metal contacts.

B-FTS allows also for less complex synthesis of nanostructures. It requires no special substrate except that the substrate should be thermally stable and with stand the high temperature which can reach above 2000 °C at some particular location of the flame. Although all results are not given here, nanostructures have been so far successfully synthesized on substrates such as Al, Cu, Si, steel and quartz. In this method, the flame oxidizes and evaporates metals at high temperatures to produce large concentrations of oxide vapors that condense onto cooler substrates. The flame length approximately reaches 25 cm and the substrate is placed to capture the oxidized Zn at about 10 cm location in the flame. Microstructured gold on quartz in this case is only used for later stage electrical measurements in way that gold would be used as an electrode. This will form a two terminal metal-semiconductor-metal (Au-ZnO-Au) UV detector device. Quartz is also preferably used because of its thermal stability besides its excellent insulating behavior that could avoid any short circuit during electrical measurement.

Figure 5.5d)-e) show SEM images of ZnO nano-microstructures grown by C-FTS approach on patterned chip (Si) that synthesized in 4 hours processing time. According to experimental observations, synthesizing of such ZnO nanostructures by C-FTS approach requires about 0.5 - 4 hours. Formation of micro sized (average diameter $\approx 0.5\ \mu m$ along the length) ZnO nanoneedles network (Figure 5.5d)) bridging the gap between two Au electrodes on the chip are observed. Figure 5.5e) shows the high magnification SEM image of the gap region shown in

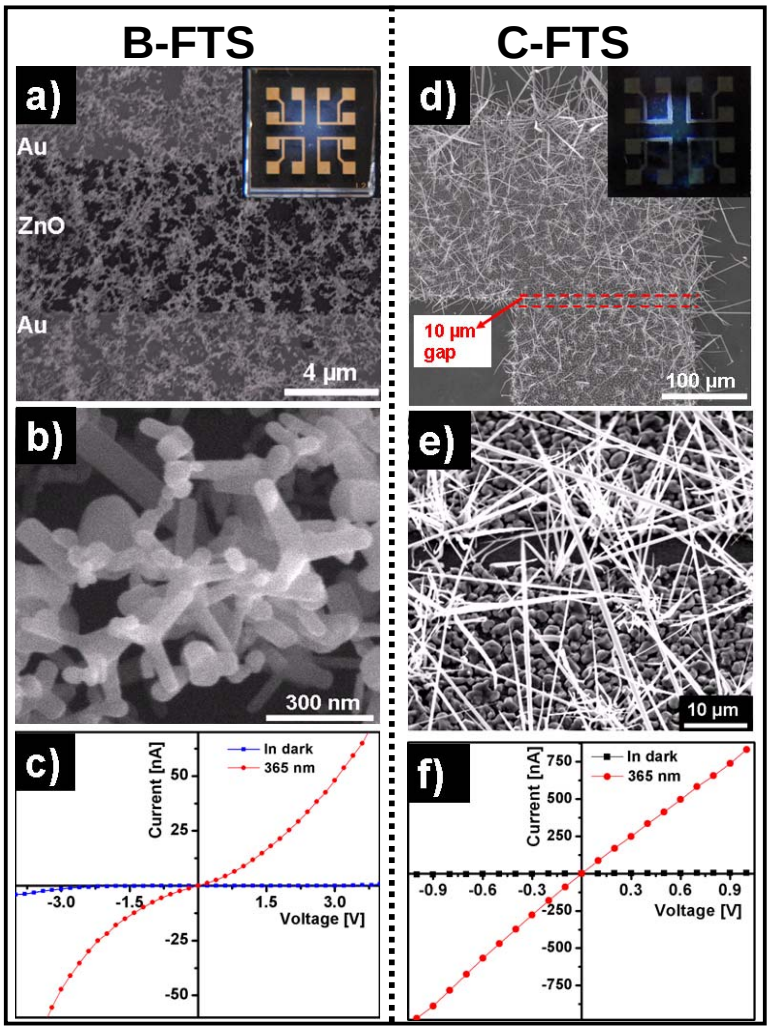

Figure 5.5: *(a-b) SEM images of ZnO nano-microstructures networks grown directly on the patterned chip (with Au electrodes) using B-FTS approach. The inset in a) shows the digital image of the chip and the bright (blue) contrast (in the centre) corresponds to location where these structures have been grown. b) High magnification SEM image from the gap region in a) showing growth of interconnected ZnO nanotetrapods which form the bridge between the gaps. c) I-V characteristics from the bridging ZnO nanotetrapods network (shown in b) between the gap the in dark and under UV (365 nm) illumination. (d-e) Low and high magnification SEM images from 1D ZnO nano-microstructures bridging the gap grown by C-FTS approach respectively. Similar to a), the inset in d) shows the digital image of the chip fabricated with ZnO structures by C-FTS approach. The high magnification SEM image (e) demonstrates the growth of large ZnO needles which can easily bridge the gap. f) I-V characteristics from bridging ZnO needles network (e) grown by C-FTS approach in dark and under UV (365 nm) illumination. It shows that the on/off ratio of the bridging network (d) is enhanced by more than 2 orders of magnitude.*

Figure 5.5d). According to SEM image presented in 5.5e), across the gap region on the chip, mm long ZnO nanoneedles from sides (on gold electrodes) interconnect each other to bridge the gap, which is complete as a final UV detector. Due to their random alignments and higher aspect ratios, there is a probability that ZnO nano-microneedles, from both sides of the electrodes, interpenetrate each other and establish a continuous path for current flow. At the same time some of the ZnO nano-microneedles can form direct bridges between two Au electrodes.

The growth mechanism in C-FTS is believed to be a combination of vapor solid (VS) and VLS process, but with the Au catalyst not coming at the top of the ZnO NWs as reported before [142–144]. The VS process take place in the early stages of temperature ramping when the Zn vaporizes at around 550 °C and it gets oxidized in presence of oxygen in air, just before the formation of molten Au droplets at temperatures higher than 630 °C. When the temperature of the furnace reached $\sim$ 950 °C, the Au droplets are already formed and might serve further as nucleation centers for growth of the ZnO nanoneedles like in the conventional VLS mechanism but since amount of gold content is very large (gold coated electrode with thickness $\sim 35nm$), gold droplets do not reach the top of ZnO needles. Zinc oxide nanoneedles with lengths in the range of 50 to 200 μm and diameters in the range of 50 to 200 nm which form interconnecting bridges across the gaps were synthesized by C-FTS approach. The I-V characteristics under dark and UV (365 nm) irradiance shows more than two orders of magnitude in the on/off ratio Figure (5.5f) and Ohmic contacts behavior in C-FTS samples. The crystalline nature and growth orientation of these ZnO nano-microstructures (grown by B-FTS and C-FTS approaches) on SiO2/Si substrates with Au electrodes on chip was confirmed by X-ray diffraction (XRD) studies. XRD spectra (Figure 5.6a-b) show that ZnO nano-microstructures do not exhibit a dominant Bragg reflection in all depositions of the samples by B-FTS and C-FTS techniques. As can be seen from the figure main XRD peaks for B-FTS and C-FTS samples are (100) and (002) and reflections (101) are a little bit lower. The Bragg reflections that corresponds to ZnO nanostructures, Si substrate and Au contacts are marked in the figure. The high intensity and narrow full width at half maximum (FWHM) XRD peaks of the samples obviously reveals that the ZnO are of high crystal quality as compared to sputter deposited NW synthesized in TFF approach. In the hexagonal structure of ZnO, the plane spacing is related to the

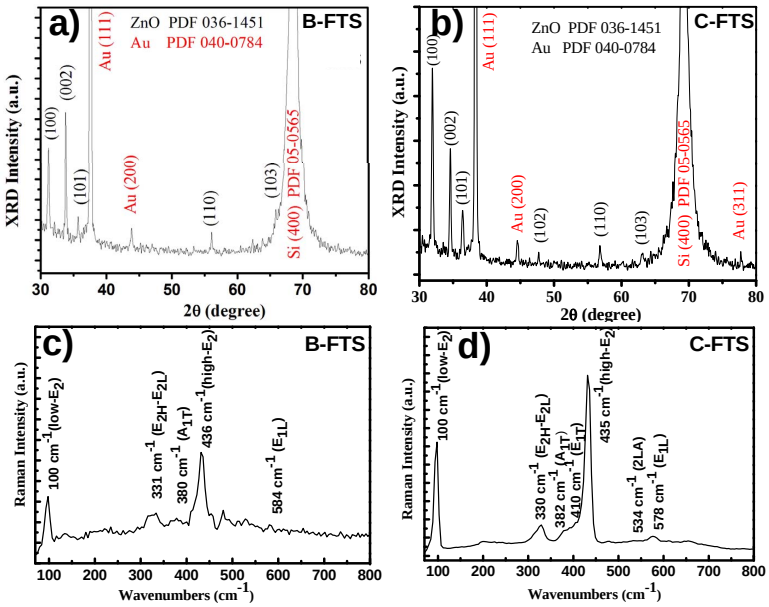

Figure 5.6: *(a-b) XRD and (c-d) micro-Raman studies of ZnO nano-microstructure network bridges fabricated on SiO2/Si substrates with Au electrodes by B-FTS and C-FTS approaches, respectively.*

lattice constant a and the Miller indices by the following relation [145–147].

$$\frac{1}{d^2_{(hkl)}} = \frac{4}{3}\left(\frac{h^2+hk+k^2}{a^2}\right) + \frac{l^2}{c^2} \tag{5.3}$$

where a and c are the lattice constants, d is the spacing between planes of given Miller indices h, k and l. The lattice parameter d (002) in the unstressed ZnO bulk is about 2.602 Å, and the d(002) value of ZnO depositions is 2.64 Å and 2.59 Å for investigated B-FTS and C-FTS samples, respectively. The lattice parameters c and a were obtained using standard relations [145–147]: $c = 5.29 \pm 0.01$ Å and $a = 3.30 \pm 0.01$ Å for B-FTS samples and $c = 5.18 \pm 0.01$ Å and $a = 3.23 \pm 0.01$ Å for C-FTS samples. These lattice parameters are in good agreement with accepted literature values and prove the quality of obtained samples. The measured value of the c/a ratio for samples B-FTS and C-FTS was around 1.603 and 1.604, respectively, which is in agreement with value for bulk ZnO at 1.602[146],[148].

In collaboration with Dr. Oleg Lupan, the quality of the B-FTS and C-FTS samples are investigated with Raman spectroscopy for confirmation of XRD result(Figure 5.6c-d). Raman measurements can provide detailed information

about the material quality, the phase and purity, which are very helpful to understand transport properties and phonon interaction with the free carriers for determining device performance [133, 144, 149, 150]. An intense E_2(high) mode peak in samples indicates that the wurtzite crystalline quality of the ZnO equivalent to literature result. All the scattering peaks are assigned to ZnO [148, 151, 152]. Thus, the Raman spectroscopy study confirms a high crystalline quality of the nanostructures similar to XRD studies.

5.2.1 UV Photodetection Using ZnO nanostructure Network Devices

In the previous section, it was shown with SEM micrographs that interconnected ZnO nanostructures are formed and also bridge the microscopic gaps of Au electrodes. B-FTS bridges the gap with interconnected nanotetrapods and C-FTS bridges with mico-nano needles. Corresponding to these, Figure 5.7a) shows a photo-detection measurement results of ZnO nanotetrapod bridging gaps between two Au electrodes on pre-patterned quartz substrate (structure shown in Figure 4.7). A B-FTS synthesized sample presents the reversible switching curves of current through the device structure when the UV light was switched on/off every 50 seconds, at a constant bias voltage of 3.6 V across it. The reproducibility of the photocurrent variations was demonstrated by almost identical rises and decays curves in four cycles. The current on/off ratio was $\sim$ 254.5 at 3.6 V biasing and it increases to $\sim$ 3277 at 3.0 V or to $\sim$ 4500 at 2.4 V biasing of the device structure. The ZnO nanotetrapods network-based device was found to exhibit a fast response time to UV light irradiation and ultrafast recovery time. Experimental results in here clearly prove the promising potentials of the B-FTS technology for rapid fabrication of highly efficient UV photodetectors devices based on networked ZnO nanotetrapods. Similarly Figure 5.7d) shows switching curves of electrical current in dark and under UV illumination of the C-FTS device at constant 0.3 V bias voltages. A current on/off ratio of $\sim$ 312 at 0.3 V bias voltage was measured for C-FTS device structure. A small peak in B-FTS sample (Figure 5.7a)) is observed in the first few seconds upon UV cycle illumination and current gradually decreases to its stable value. This small peaks however are not observed in the case of C-FTS samples and similar characteristic

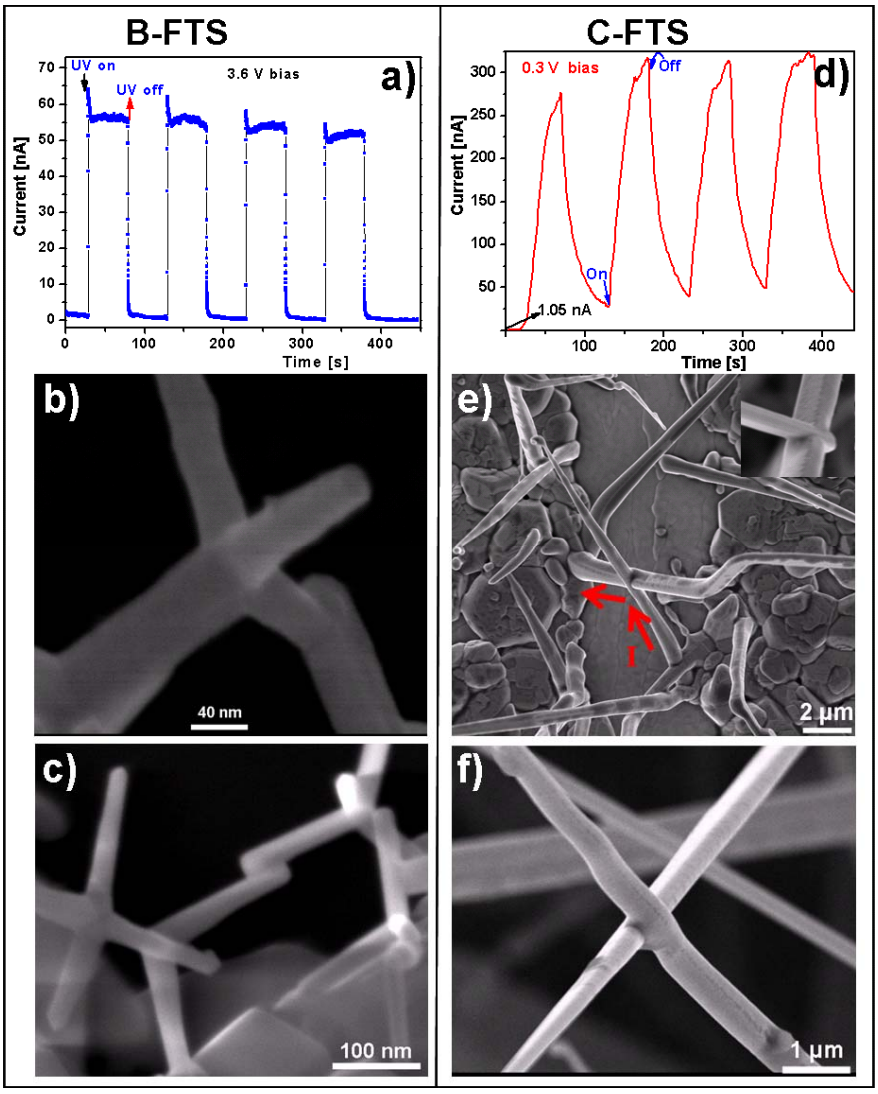

Figure 5.7: *a) Reversible switching of electrical current at 3.6 V biasing voltage with 50 s periodic illumination of UV light for B-FTS specimen. The SEM images show various combination of connections in nanotetrapods. The nanotetrapod arms can have complete interpenetration (b) giving closed circuit for current flow or the arms could be touching as in (c) which might cause a short circuit in this particular arms. d) Reversible switching of electrical current for C-FTS detector at 0.3 V biasing voltage in the dark state and under UV light irradiance. e) The SEM image of C-FTS synthesized sample shows a well binded of ZnO micro-nanoneedles to Au electrode and partially interpenetrating ZnO mciro-nanoneedles providing a complete path for electric current. The inset SEM image shows a completely interpenetrated ZnO needles. A partially interpenetrating and touching ZnO needles are also shown in (f).*

peak was also reported for NWs whose dimension is less that 100 nm, Si NW phototransistor [153], Ag-Ge NW [154], ZnO NW [155]. The reason is believed to be the reaction of NW surfaces with air molecules or water vapor. According to these reports, such behavior is not observed when UV light ON/OFF under vacuum atmosphere.

5.2.2 Analysis of Fast Switching UV photodetectors based on FTS Approach

A closer investigation of a single pulse photocurrent in air shows that the rise and decay photocurrent follow exponential function. The rising and decaying photocurrent (Figure 5.7a) and d) with corresponding time measurements are determined through bi-exponential fit respectively. The two bi-exponential function equations used for rising and decaying photocurrent respectively are [133, 156]:

$$I(t) = I_0 + A_1(1 - e^{-\frac{t}{\tau_{r1}}}) + A_2(1 - e^{-\frac{t}{\tau_{r2}}}) \tag{5.4}$$

$$I(t) = I_0 + A_3 e^{-\frac{t}{\tau_{d1}}} + A_4 e^{-\frac{t}{\tau_{d2}}} \tag{5.5}$$

where I_0 is dark current, A_1, A_2, A_3 and A_4 are positive constants. τ_{r1}, τ_{r2} and τ_{d1}, τ_{d2} are time constants for growing and decaying photocurrent, respectively. The rise and decay curve fittings are shown in Figure 5.8b) and 5.8c) respectively. Based on the curve fittings on a single pulse 5.8a), the rise time constants for B-FTS specimens were τ_{r1}= τ_{r2}=68 ms, and decay time was τ_{d1}=32.18 ms. However, for decay part of the curve, it can be seen that second time constant is large, τ_{d2}=200.48 ms. It should be noted that the response time resolution of the picoampere meter is 30 ms and thus the real reset time the device is expected to be shorter than the one shown. The sensitivity curve at different bias voltages is also shown in 5.8d). It shows that at lower bias voltage, the sensitivity gets higher. Similar fittings were performed for C-FTS samples and resulted in rise time τ_{r1}= τ_{r2}=27 s and decay time constants τ_{d1}=7 s and τ_{d2}=40 s. According to the experimental results presented above, one can conclude that B-FTS samples shows an excellent response/recovery time, with the fastest rise time constants of about 68 ms and first decay time of 32 ms. C-FTS synthesized samples show much slower total response/recovery time constants of about 27 s and

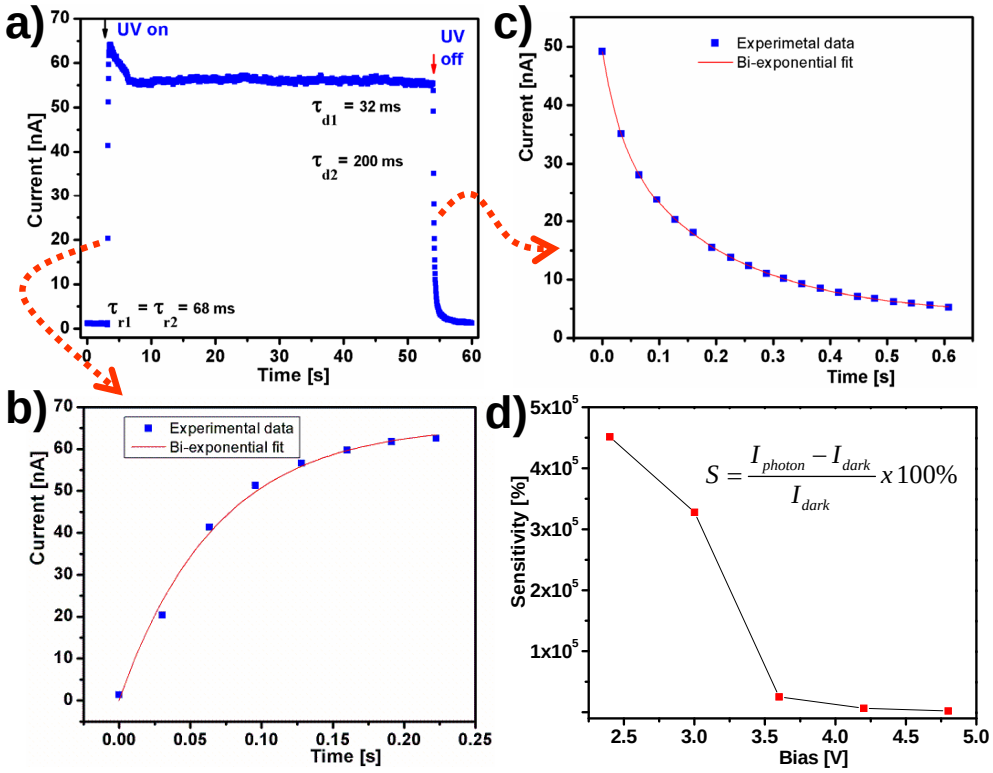

Figure 5.8: *a) Plot of a single pulse from Figure 5.7a) and measured time constants through curve fittings for B-FTS ZnO nanotetrapods device. The rising (b) and decaying (c) current time constants are measured through bi-exponential fit to equations 5.4 and 5.5 respectively. d)Photo-sensitivity versus bias voltage for B-FTS ZnO nanotetrapods device .*

7 s, respectively (5.9). In C-FTS, when the UV light is turned on and off, the increase or decrease in photocurrent takes some time to reach to the saturation. The reason would likely be the reduced influence of the surface states observed for nanostructures fabricated by C-FTS approach. The photoresponse showed only a minor component with long decay times (tens of seconds) which seems to originate from surface states. Because a combination of high-density micro-nano networks connected are observed in the C-FTS approach in which the surface to volume ratio would be smaller as compared to the fracture approach or to the nanosized tetrapod arms in B-FTS. Similar results have also been reported by Pearton et al. [138].

Table 5.1 summarizes earlier reports on ZnO-nanostructures based UV pho-

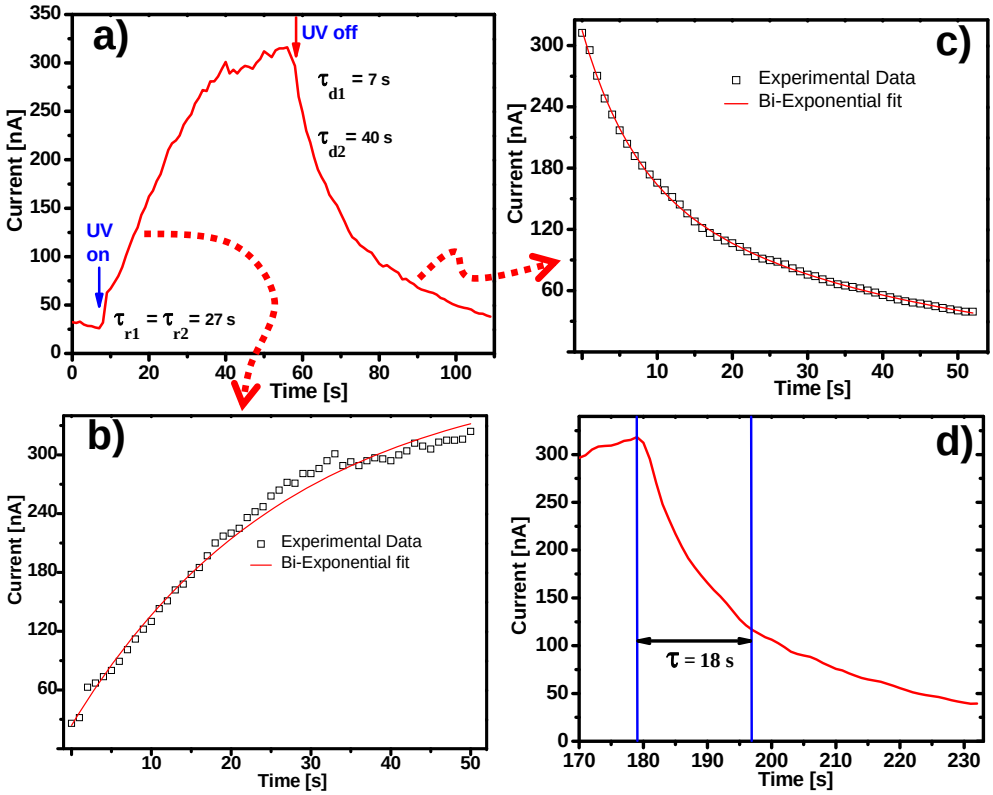

Figure 5.9: *a) Plot of a single pulse from Figure 5.7d) and measured time constants through curve fittings for B-FTS ZnO nanotetrapods device. The rising (b) and decaying (c) current time constants are measured through bi-exponential fit to equations 5.4 and 5.5 respectively. d) Measurement of time taken to reach 37% of the maximum current for the same pulse shoen in a).*

todetectors and gives a comparison to devices from B-FTS and C-FTS specimens. As compared to most of the previous reports, the B-FTS UV photodetectors show the best performances in terms of fastest rise/decay times with higher signal ratio ever reported. Although, Law et al. [133] reported small rise/decay times for their UV photodetectors, they used multiple patterning steps followed by evaporation for ZnO NW device fabrication. In comparison to previous reports, B-FTS photodetector devices are superior in terms of higher signal ratio (I_{UV}/I_{dark}) (3288 in B-FTS and 1.4 in the previous report [133]), of synthesis time and simplicity of fabrication technique with in-situ possibility to integrate ZnO nanostructures directly on a chip. It is also possible that the speed of B-FTS specimens (based on crystalline nanostructure networks) could be limited by the resolution limit

Table 5.1: *Summary of ZnO nanostructure Based UV Photodetectors.*

Type of nanostructure	Growth Duration & method	UV light (nm)	Bias voltage	$\left(\frac{I_{UV}}{I_{dark}}\right)$	Rise time	Decay time	Ref.
Single NW	30 min, CVD	365	-	1.25	2 min	3 min	[157]
Single NW	2-10 min, VLS	365	0-5 V	2×10^5	∼1 s	∼1 s	[132]
Nanorod network	3-5 h, HT	365	5 V	1.8	2 s	-	[158]
NW array	3 h, TE	370	5 V	1.4	0.1 ms	0.4 ms	[133]
Spatial tetrapod network	38 min, TE	365	1 V	10^6	0.4 s	0.3 s	[159]
Nanorod network	4 h, C-FTS	365	0.3 V	312	22 s	7-12 s	this work
Nano-tetrapod network	<5 s, B-FTS	365	2.4 V	4.5×10^3	∼67 ms	∼30 ms	this work

the pico ampere meter (∼ 30 ms). In general, the B-FTS fabricated photodetectors are superior due to the rapid synthesis procedure and very good device performances as compared to previous reports.

Like the ZnO NWs in TFF approach, the change in conductance by UV light in ambient condition is due to change of surface states that are influenced by adsorbed oxygen and electron-hole pairs as explained in Figure 5.3 and equations 5.1, 5.2. C-FTS samples offered the slowest rise and decay photon under UV on/off condition. This believed to be because of the size difference in thicknesses of the NWs which the diameters are well below 100 nm in both TFF and B-FTS samples. The B-FTS samples have also showed various morphologies and a combination of many different effects that are not clearly understood could also contribute the fast response. As evidenced by SEM images, the majority of nanostructures in B-FTS devices are nanotetrapods that have nanosized arms interconnected either as touching, partially or completely interpenetrating. Based on the nano arms connection types, the possible photo-detection mechanism for such high current ratio (I_{UV}/I_{dark}) and ultra-fast response/recovery times of the

B-FTS fabricated devices can be explained by using schematic drawings presented in Figure 5.10.

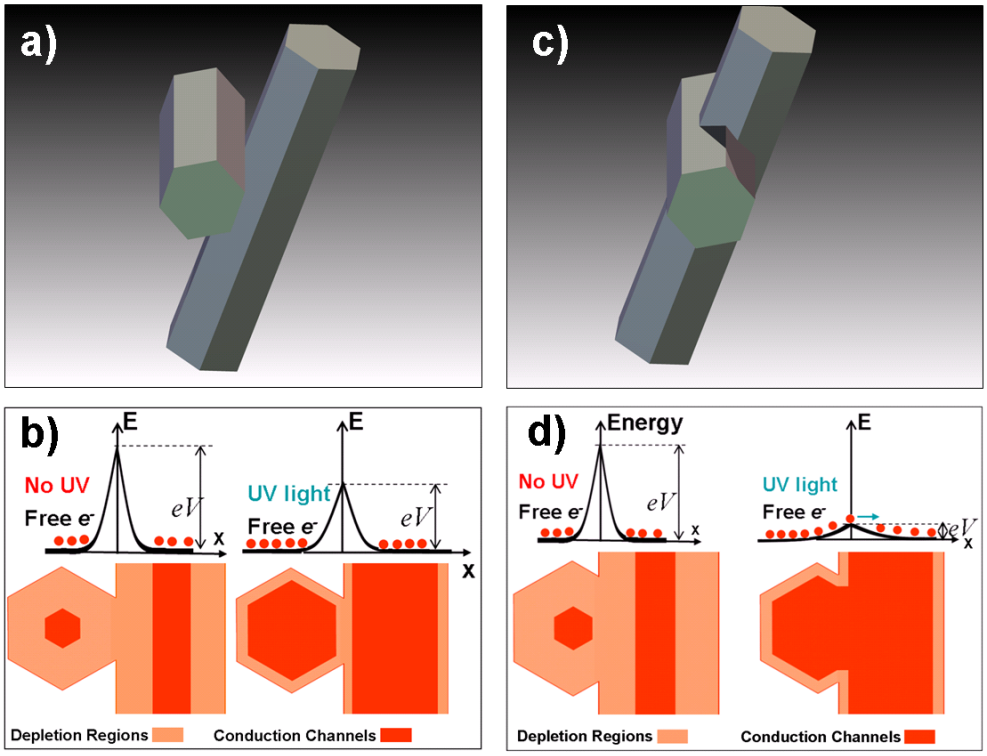

Figure 5.10: *Schematic representation of: a) touching nanotetrapod arms and its corresponding b) (top) energy band diagram in the radial direction and (bottom) cross-section structural models of the conduction mechanism of networked ZnO NWs forming potentials barriers at the boundary. A high potential barrier to the surface states because of the depletion electrons by desorbed oxygen molecules on the surface of touching NWs. Under UV illumination, the height of the potential barrier decreases but still significantly large (top). c) Shows the case of network bridge in which nanotetrapod arms are interpenetrating each other and its corresponding d) (top) energy band diagram in the radial direction and (bottom) cross-section structural models The right schematics in d) presents reduced potential barrier at the boundary of two interpenetrating NWs in cross-section that are irradiated with UV light (top) significantly increased channel and thus connected channel (bottom).*

In Figure 5.5a)-b) and Figure 5.7b)-c), it was observed that a large number of nanostructures with various morphologies being interconnected in a random fashion. These indicate on the possible presence of several types of nanojunctions

between interconnecting-interpenetrating neighbor tetrapods nanoarms or NWs forming network in the gap. In particular, it can be distinguished between a just touching nano-arms (Figure 5.10a) or partly interpenetrated nano-arms (Figure 5.10c)) of nanotetrapods synthesized through B-FTS. Similarly explanations can be extended to nano-microneedles synthesized through C-FTS approach (Figure 5.7e)-f)). Other types of nanojunctions can be formed directly inside of the nanotetrapod at the connections of four different nano-arms. As presented above, it is believed that UV detection performances strongly depend on the type of such nanojunctions formed, boundary layers which are formed and energy barriers between nanotetrapods bridging two electrical electrodes. Electrical properties of such boundary of the nanojunctions in semiconducting ZnO could be mainly responsible for enhancing the electrical activity of the interfaces between nanoarms in bridging network. It can be explained by fact that nanojunction boundary becomes electrically active by trapping an excess charge of majority carriers (e^-) at the interface. Total charge neutrality is formed by an electrostatic potential barrier between neighboring depletion layers adjacent to the nanojunction (Figure 5.10b)-d)). Considering completely ionized shallow donors of density N_0 for the depletion layers in semiconducting zinc oxide, the maximum band bending $\Phi_B(V = 0)$ at the nanojunction boundary is calculated from Poisson's equation [160, 161]:

$$\Phi_B(V = 0) = \frac{Q_i^2}{8e\epsilon\epsilon_0 N_0} \tag{5.6}$$

where e is electron charge, ϵ is static dielectric constant and ϵ_0 is permittivity of free space. Thus the width of the depletion region is

$$x_0 = \frac{Q_i}{2N_0} \approx \sqrt{\frac{\epsilon\Phi_B}{2N_0}} \tag{5.7}$$

These equations 5.6 and 5.7 permit understanding of effects at the grain boundaries in the networked tetrapods/wires. Thus, barrier height $\Phi_B(V = 0) \approx 1V$ is reduced under UV irradiation of nanotetrapod junctions and leads to a faster filling of the interface states for applied bias ($V > 0$). The bottom schematics in Figure 5.10b) present structural models of the conduction channel of nanojunctions between NWs in air for touching NWs. Interpenetrating NWs are also represented by the bottom schematics in Figure 5.10d). Formation of the depletion layer [136] and its characteristics were reported in details in previous works

[148, 149, 157]. The corresponding schematic energy band diagram (top) in the radial direction of a single ZnO NW indicating the depletion region at the surface, the surface band bending and the quasi-neutral core region of radius r in the central part of the nanostructure are also shown in Figure 5.10b). It can be seen that the conduction channels are still not connected or they are separated by the depletion layer region although the size of conduction channel of NWs increased under UV irradiance because of releasing of free electrons from oxygen ions (initially adsorbed on the ZnO surface). Unlike the case of the interpenetrating ZnO nanostructures, it can be concluded that the UV irradiation does not influence significantly energy barrier between touching NWs and electrons do not have a free conduction path. A high potential barrier to the surface states exists because of the depleting electrons by oxygen on the surface of interpenetrating NWs [137, 149, 162]. However, with irradiance of the interpenetrating ZnO NWs forming nanojunctions using UV light (365 nm), the potentials barriers are significantly reduced and the channel width became interconnected as schematically shown in Figure 5.10d). Unlike the case of the interpenetrating ZnO NWs, it can be concluded that the UV irradiation does not significantly influence the energy barrier between touching NWs and electrons do not have a free conduction path. As revealed by the high magnification SEM images, many of nanotetrapod arms in the B-FTS specimen are not perfectly interpenetrating but interconnected by touching (nanoscopic junction) that are speculated to offer low dark current as compared to the completely interpenetrated nanotetrapod arms. The nanoscopic junctions might be the reason for the high speed switching of the current provided that the overall conductance is dominated by these juctions. Thus, it can be concluded that several types of nanojunctions formed between networked nanotetrapods or NWs play significant role in photodetection mechanism of such photodetectors.

The reproducibility of B-FTS results is checked for many specimens. With the right synthesis method and measurement, all of them proved similar behavior. A second specimen investigated also demonstrate in principle similar behavior with quick response and recovery time (Figure 5.11d)). The UV light was switched on/off in every 50 seconds cyclically under a constant 1 V biasing. Except the very first photon-current, the reproducibility is demonstrated by identical resistance rises and decays in four cycles. The on/off ratio at 1 V for

this case is approximately 139, which much larger than the case for S1.

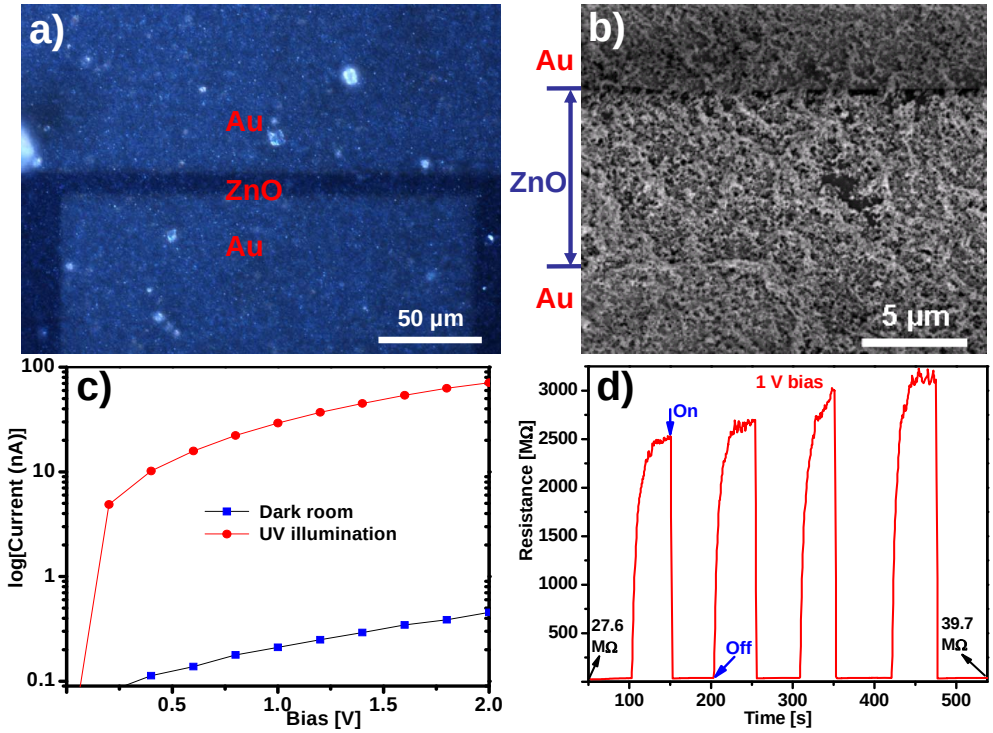

Figure 5.11: *a) depicts the optical microscopy image gold electrodes where a 10 µm gap is ZnO bridged. b) shows the SEM image of Sample 2 that has relatively low dense ZnO networks in the gap. c) I-V characteristic re-plotted on natural logarithm of the same sample under dark and 365 nm UV illumination. d) resistance switching with and without UV light at constant 1 V bias voltage.*

The versatility of the FTS approaches to fabricate devices from various metal oxide semiconductor materials is under thorough investigation. Preliminary results however indicate a promising result as given below for instance SnO_2 nanostructures. Further investigation is preformed by MSc. Ingo Paulowicz (PhD thesis under preparation). The versatility of C-FTS approach can be confirmed through the synthesis conductance measurement of nanostructures from SnO_2. It is known that one of the prominent methods that SnO_2 NWs could be synthesized is a VLS technique [163–165]. However VLS methods and many other methods are either too expensive, complicated requiring vacuum system or time consuming. C-FTS as already discussed is a modified version of VLS process and is less complicated during synthesis and cheaper as compared to the normal VLS

method. It is the second most investigated material next to ZnO. Tin dioxide is

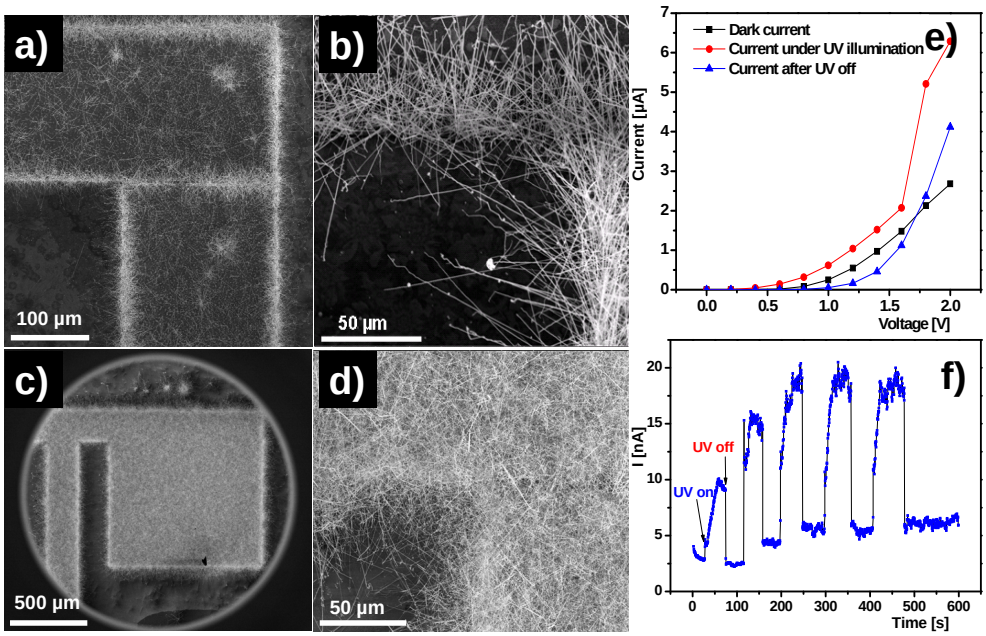

Figure 5.12: *Illustrates a)-d) SEM micrographs of SnO_2 nanostructures at various magnifications. e) I-V characteristics measurement at dark current and under UV illumination. f) UV response of the nanostructures at constant voltage of 0.4 volts. The photocurrent has increased 1n an order of magnitude once the electrons are activated by UV illumination.*

an n-type semiconductor wide band gap of $\sim$ 3.6 eV at 300 K [166] has received enormous research interest in the past few years because of its potentials as opto-electronic device. The gas sensing properties based on an individual SnO_2 NWs [167, 168] and a NWFET and photo detection property also reported [169, 170]. A similar result was achieved for in the synthesis of SnO_2 crystalline nanostructures as depicted in Figure 5.12. The nanostructures show photo sensoric property as depicted in Figure 5.12e)-f). UV irradiation of the nanostructures at an ambient air condition resulted in an increase in conductance (on/off ratio 10). The increase in conductance during illumination is believed to originate from the removal of oxygen species (O^{-2}, O_2^- that are desorbed on the surface of the nanostructures as the measurement is was performed at an ambient condition. The surface-bound electrons will be released in the depletion zone increasing the charge carriers through exciting electrons from valence band to conduction band [170] and thus enhancing the conductance. The C-FTS is thus simple, requiring

no vacuum system, can be used to synthesize nanostructures without catalyst and many oxide forming nanostructures can be synthesized. AU catalyzed synthesis of ZnO and SnO_2 nanostructures are shown reproducibly.

5.3 Summary

Two routes (FTS and TFF) for the synthesis of metal oxide nanostructures into microchips of Si and quartz substrate have been demonstrated. Both of them allow for the integration of NWs (nanostructures) into chips and are in principle ready for upscaling. A comparison between each route shows that individual route has its own advantage and disadvantage. The two types of FTS approach (C-FTS and B-FTS) synthesis approaches are mainly used to synthesize ZnO 3D network type of structure that are interesting for sensors such as UV detectors. Both approaches allow us in-situ integration of nanostructures between the electrodes on chips during the growth process itself. The B-FTS technology can be characterized by a rapid synthesis process (3-5 seconds) for fabrication of high crystal quality interconnected ZnO nanotetrapod network bridging the two pre-patterned Au electrodes. B-FTS fabricated photodetector devices exhibit a high current ratio $I_{UV}/I_{dark} = 4.5 \times 10^3$ at 2.4 V with a fast recovery time constant ($\sim 32ms$). High magnification SEM results revealed that FTS synthesized nanostructures have got bridging though completely interpenetrating or partially intenpenetrating or just connection by touching nanotetrapod and micro-nanoneedles. The UV photodetection mechanism is proposed in terms of modifications in energy band diagrams under UV illuminations of ZnO nanojunctions. The chemisorbed oxygen on the nanostructures increase the energy barriers that affect the dark current and thus detection of UV light. Proposed technological approaches can be easily scaled-up and therefore exhibit large interest for further studies and various sensor applications. In relative terms C-FTS fabricated photo detector showed slowest response under periodic UV irradiance. SnO_2 nanostructures were also synthesized through C-FTS approach and the preliminary result as UV detector shows a promising result.

It is also demonstrated that horizontal ZnO NWs can be synthesized in TFF approach employing self-organized photoresist fractures as a nanoscale template.

This method is reproducible and is a versatile process that nearly all materials deposited in a PVD technique are converted in to NWS. The synthesis and experimental studies as UV photodetector and gas sensor have already been intensively studied in this chapter. A comparison of ZnO NWs (TFF) to ZnO C-FTS as a UV detector confirmed that high crystal quality NWs do not guarantee the synthesis of best sensor out of it. A poor crystal quality and granular featured ZnO NW synthesized in TFF approach also demonstrated fast response as in a UV photo-detection process in ambient environmental condition. The possibility of A UV activated oxygen sensor was also demonstrated using ZnO NW fabricated through TFF.

Generally, the three synthesis techniques offer NW integration routes that do not require standard processes. Moreover, an *in-situ* integration of the NWs and nanostructures has been demonstrated that avoids the use of standard processing techniques such as E-beam lithography, focused ion beam methods, or alignment processes. This allows for high speed synthesis of NWs and integration which can be upscaled to mass fabrication. The synthesized devices and the measurement results also demonstrated the feasibility of the synthesis approaches in a wafer-level processing and the NWs showed promising result as photodetectors or gas sensors. However, for a NW sensor a control electronics should be integrated, for example, for sensor drift correction and selectivity, as well as long-term stability tests have to be carried out.

6 Semiconductor-Metal Hybrid Nanostructures for NWFET and Sensor Applications

In the previous chapter, semiconductor nanostructures fabrications and their potential as sensors were demonstrated. An *in-situ* integration of nanostructures into chips was presented through an efficiently developed TFF and FTS methods and promising results have been shown. In another approach, core-shell nanostructures (metal-metal oxide hybrid structures) that add new functionalities can also be obtained from NWs and nanostructures. This chapter presents the synthesis of a novel metal-metal oxide hybrid nanostructures integrated into chips with tremendous potential applications as NW field effect transistor(NWFET) and magnetic field sensor. TFF and TAM are the two main routes employed for such hybrid nanostructures synthesis. The details on the procedures and the synthesis parameters used for fabricating iron oxide nanostructures are already discussed and refer to Chapter 4.

In section 6.1, the electrical transport properties of both metal and semiconductor-metal hybrid NWs are given. In the subsequent subsections, results from two different materials Ti and Al NWs are presented. In section 6.2, a general discussion on the synthesis and the factors that affect properties iron oxide NWs are given. Results from iron oxide NWs synthesized in a hotplate and a muffle type furnace are given in sections 6.2.2 and 6.2.3 respectively. Detail characteristics of iron oxide-iron core nanospikes in the subsections of 6.2.2. Finally the summary of this chapter highlighting the most important achievements are given in section 6.3.

6.1 Transport Properties in Metal and Semiconductor Hybrid NWs

6.1.1 Ti NW Synthesized in TFF Approach

Ti NWs synthesized using TFF approach are demonstrated in this section. After fabrication of a networked crack structures, 70 nm nominal thickness of Ti was sputter deposited on a 100 nm SiO_2 coated P^{++} doped Si substrate. After mask-lift off in ultrasonic acetone bath, the Ti NW was electrochemically anodized at 10 V DC voltage for a duration 10 minutes. This gives a possible route for the fabrication of oxide wrapped metal NW structures (i.e., core-shell metal oxide NWs with the metal as core and metal oxide as shell). The NWs synthesized through sputter deposition are found to have granular structure. Typical NWs from Ti and Au that are rough and granular structure synthesized in TFF approach are shown in the Atomic Force Microscopy (AFM) micrographs in Figure 6.1. The AFM images of NWs produced are found to be polycrystalline with grainy features as shown in 6.1 b). The electronic characteristics of Ti and anodized Ti core-shell NWs field-effect transistors (NWFET) are illustrated here.

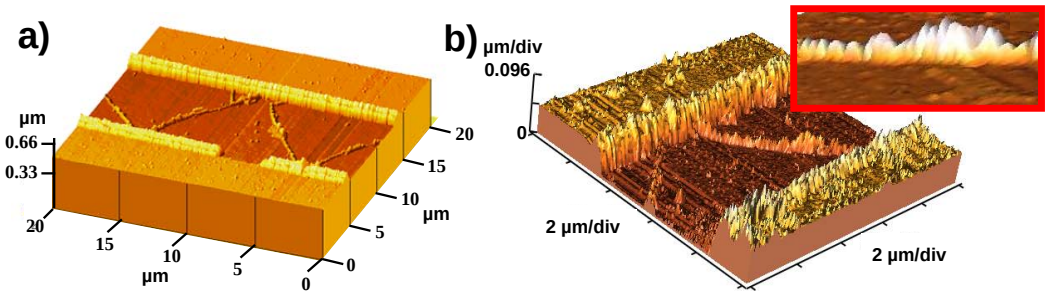

Figure 6.1: *a) AFM Image of zig-zag oriented Ti NW and b) AFM image of a rough Au NW synthesized through sputter deposition. The inset in b) illustrates grainy features of the NWs. Note that the z-scale is drastically overemphasized.*

6.1.1.1 Anodization for Controlled Shrinking of Metal NWs

A vacuum deposition of NWs in cracks result in granular NWs as shown above by the AFM images. A problem in deposition is to meet the exact point in time, where the grains during their growth close their intermediate gaps and form a transition from a chain of clusters into a continuous NW. But this transition is very interesting for sensor fabrication [171], as it creates narrow nano gaps or only a few atom wide points of constriction. Metal NWs such as Ti, Ni, Pd and Au synthesized in TFF and possessing granular structure have been studied and characterized [47]. Depending on the type of NW material, the NWs could also be converted into metal-oxide-metal (M-O-M) or core-shell structure in a controlled manner through electrochemical anodization.

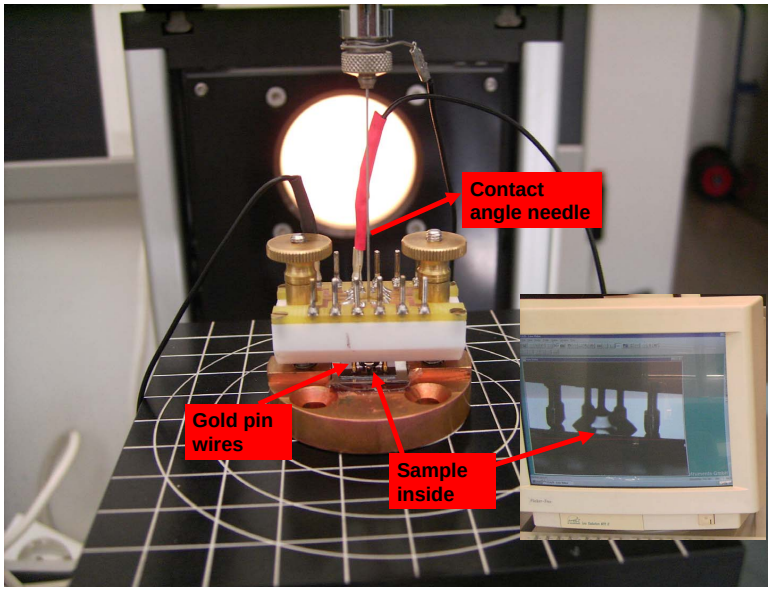

Figure 6.2: *Camera image of experimental setup for the electrochemical anodization of titanium films and NWs. The course of current flow at a constant voltage through a sample containing titanium NWs and films while anodizing at a constant voltage. The computer inset image shows image of water droplet with voltage sourcing taken during anodization.*

An electrochemical anodization setup as shown in Figure 6.2 can be used to form a controlled shrinking of the diameter, as here discussed in the example of Ti NWs. Furthermore, by the partial conversion of the metallic Ti grains in the wires into TiO_2, hybrid devices can be formed with interesting field effect

properties. The grain boundaries play a significant role during the oxidation process. The AFM images shown in Figure 6.1, reveal the granular nature of Ti NW. The approximate diameter of these NWs vary from 80 nm to 120 nm. These grains also limit the usefulness of the description of the diameter of the wire, as it can be much thinner between the grains. A contact angle instrument needle is used to place a micro liter droplet of deionized water on top of the gap where NWs are located and the schematic details of the anodization set-up depicted in Figure 6.3a). A deionized water is found to be a good enough electrolyte for controlled electrochemical oxidation for Ti NWs and films. Experiments with several electrolytes like citric acid showed that controlled anodization conditions could be affected most by simply using partially ion depleted water, which was produced in a deionization setup. In anodic oxidation, the growth of a uniform oxide film begins (mainly TiO_2), inhibiting the active dissolution of titanium

$$Ti + 2H_2O \rightarrow TiO_2 + 4H + 4e^- \tag{6.1}$$

A non-stable Ti_2O_3 may be formed but shortly oxidizes to TiO_2 as it is in contact with water. Its chemical equation is

$$Ti_2O_3 + H_2O \rightarrow 2TiO_2 + 2H + 2e^- \tag{6.2}$$

Thus, a stable TiO_2 formation expected after anodization experiment is performed [172]. Between the 200 μm wide Ti thin films, a gap is visible (10 μm) as shown in Figure 6.3b) where the anodized Ti NWs are located. The color contrast in the figure also shows part of the oxidized Ti. The current measured during oxidation is used for deciding the thickness of the oxide. A constant voltage was supplied and the corresponding current was measured while anodization is taking place through a voltage of 10 V (Figure 6.3d)). By measuring the resistance (current) in the wire during anodization, a well-controlled thickness of the conductive part of the wire can be set by stopping the anodization processes at the desired resistance. Reports show that the anodization rate for very thin films by using purely electrochemical methods is about 2-2.5 nm/V, independent of the electrolyte pH [173]. The higher the anodization voltage, the higher will be the rate of oxidation and thus faster decrease in current. After anodization, the average thickness of top oxide layer is expected to be around 20-25 nm. This

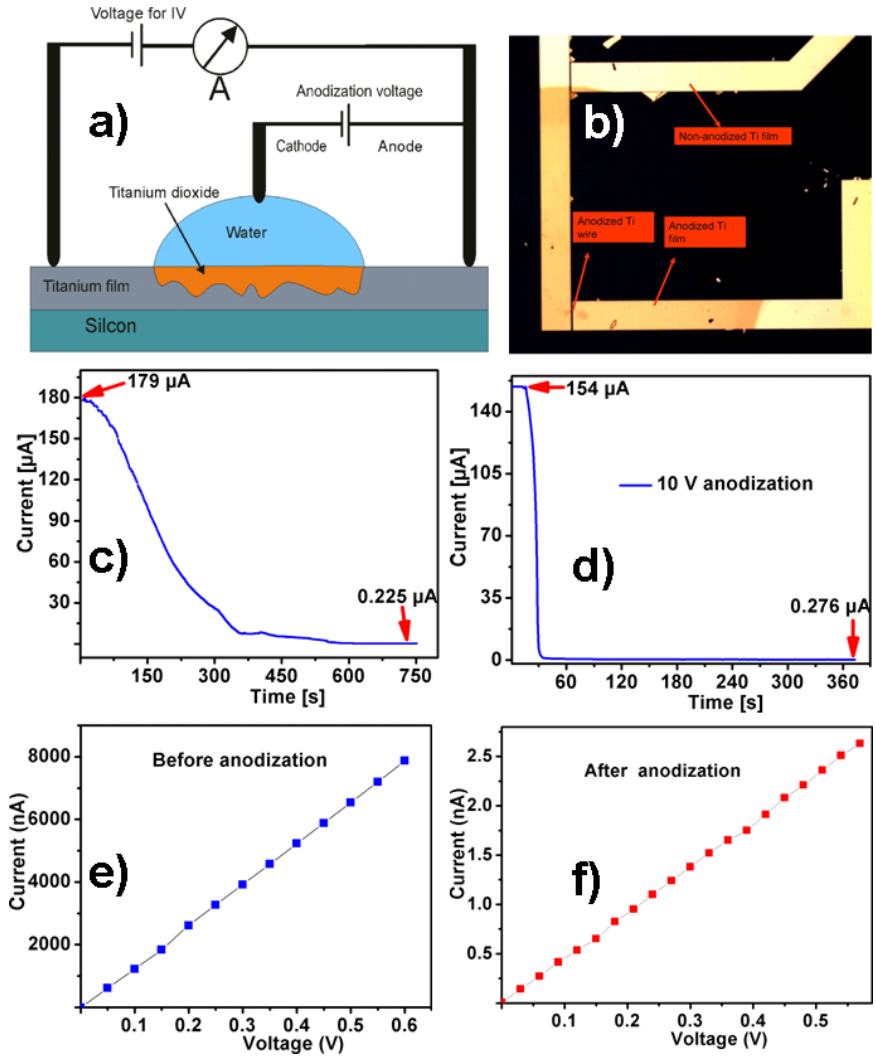

Figure 6.3: *a) Schematic experimental setup for the anodizing Titanium films and NWs. b) Optical micrograph of anodized sample showing a color distinction between anodized and non-anodized parts. c) Test current vs time through a 10 nm titanium film while anodization takes place. A constant of 1 V for electric current during 10 V anodization. d) The course of current flow at a constant voltage through a sample containing titanium NWs while anodizing in 10 V voltage supply. I-V characteristics e) before and f) after anodization. The resistance increases from 0.076 to 217 MΩ.*

means that the average thickness of the conducting NW shrinks in the range of 45-50 nm in cross-sectional view. This can lead to a core shell structure, where the metallic core is only a minor fraction of the NWs. To tune in a special titanium oxide structure like rutile or anatase, a controlled setup like in [174] can be

used. Especially such an automated micro droplet setup could be used on wafer level, allowing the setup to be used in micro-fabrication. The study here should only elucidate the potentials of the approach which holds for devices. The I-V characteristics before and after anodization are demonstrated in Figures 6.3e) and f) respectively. From the linear I-V response, it can be observed that the resistance is increased from 0.076 to 217 $M\Omega$ after anodization, which is close to the resistance regime where electron tunneling plays the main role of electron transport. The anodized NWs exhibit several types of electrical conductivities.

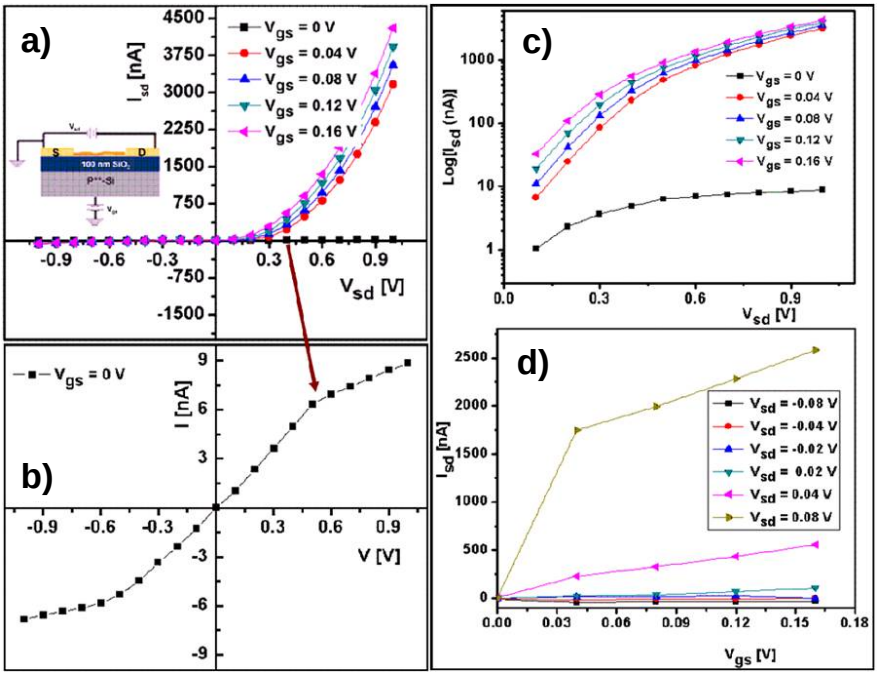

Figure 6.4: *a) I_{sd}-V_{sd} characteristic of anodized Ti NWs as a NWFET, b) the magnified I_{sd}-V_{sd} plot for zero gate voltage in forward and reverse bias, (c) Logarithmic plot corresponding to Figure a, (d) transfer characteristics of NW-FET at different source drain voltages V_{sd}.*

The recorded data in Figure 6.4 shows an increase in conductance when the gate voltage is increased ($V_{gs} > 0$). The current can be increased more than three orders of magnitude by gate-voltage supply. When a gate voltage is applied, the corresponding electric field developed in the 100 nm SiO_2 depletes electrons from titanium oxide layer. The increase in conductance with increasingly positive $V_{gs} > 0$ indicates the NWs to be n-type [175].

The FETs exhibit properties which are already suitable for applications as sensors. Thus the gas detection experiments were performed with anodized Ti NWs synthesized in TFF approach. The observed field effect behavior might be used to shift the NW-operated devices, for example, as sensor, into a sensitive region of its conductivity curve. The hybrid NW FET, however, showed a drastic and fast response in the drain current when it is exposed to different partial pressures of oxygen (Figure 6.5). The reduction in drain current under the exposure of oxygen is believed to be the result of adsorption of O_2 at oxygen vacancy sites forming O^{-2} and O^{-} through depleting electron from titania.

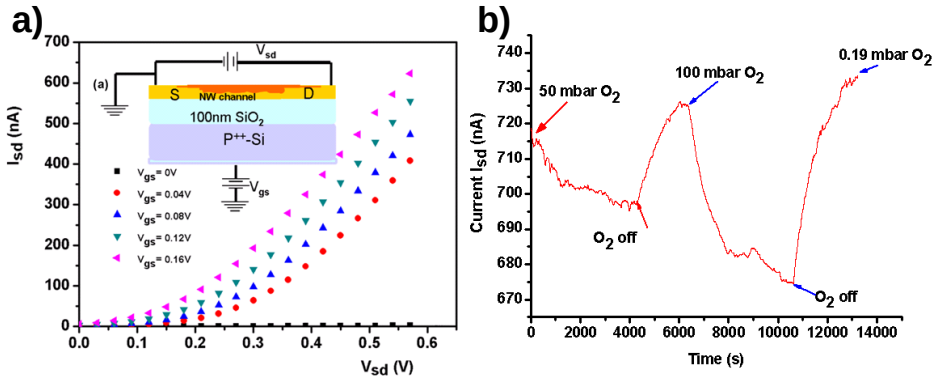

Figure 6.5: *a) I-V characteristics after Ti NW anodization (black square dots at the bottom) without an electrical field, it is the same curve shown in Figure 6.3(f) and after applying a gate voltage (increasing, rectifying curves). The inset (a) shows the here used setup to apply the gate voltage: the highly doped silicon wafer serves as gate electrode. b) Sensing response of anodized Ti NWFET (at a constant V_{gs} = 0.08 V and V_{sd} = 0.6 V) at different partial pressures of oxygen. A pronounced answer is visible.*

Palladium (Pd) NWs [47] synthesized using TFF respond respond quickly so that one can see the performance of anodized Ti NW when it is exposed to hydrogen gas environment. Of course Pd NWs are known for their very fast response from the works of Penner [81]. The gas detection experiments were performed with the NWs synthesized with the help of TFF approach. In this context, the gas-sensing capabilities of Pd and anodized Ti NWs synthesized under fracture approach have also been tested and are shown in Figure 6.6. The synthesized Pd NWs showed a drastic change in the conductance when exposed to H_2. However the anodized Ti NWs used above did not show any change in the conductance when the NWs are exposed to H_2 gas environment. Penner et

al., proposed that the drastic change in conductance appears from the closing of nanoscopic grain gaps which is caused by swelling of lattices (increase in the size) of palladium grains due to absorption of hydrogen. Granular features of Pd NWs in this case have nanoscopic gaps in air that null down the conductance. In hydrogen environment, nano-break junctions will get close leading to 6-8 orders of magnitude decrease in the resistance along the length of the wire and providing a sensing mechanism for a range of hydrogen concentrations [176].

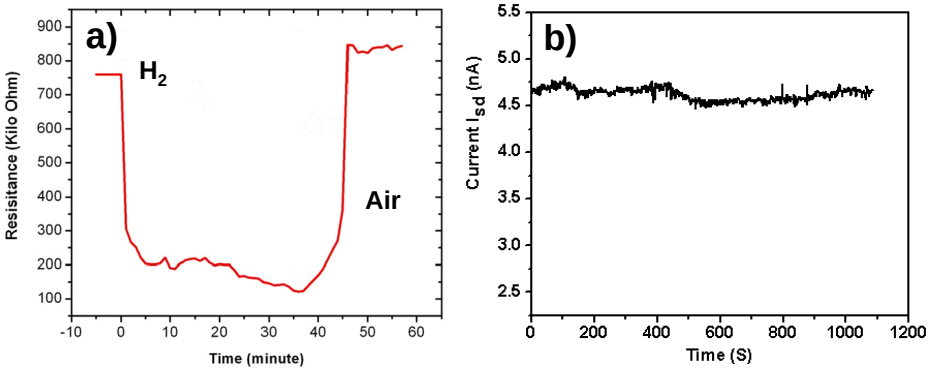

Figure 6.6: *a) Comparison of sensor properties at H_2 containing environments. (a) Palladium NW as hydrogen sensor, comparison [47], shows a pronounced answer in terms of increased conductivity. (b)The anodized Ti NW FET (at a constant V_{gs} = 0.16 V and V_{sd} = 0.3 V) shows no response to hydrogen.*

6.1.2 Characteristics of Al NW

TFF and modified version of TFF (MTFF) are used here for the synthesis of Al NW. In principle both approaches follow similar procedures except three more lithographic processing steps in the MTFF approach. The MTFF approach however permits for the integration of localized gate and localized area application of gate electric field. The small area gate electric field is believed to reduce the probability of the dielectric break down that increases with larger surface area which the gate voltage is applied. The details and results obtained are given in the following subsections.

6.1.2.1 Characteristics of Al NW Synthesized in TFF Approach

Like Ti NWs, the synthesis of Al NW begins with deposition of photoresist template. After thermal fracturing of the resist, aluminum is sputter deposited in two cycles through magnetron sputtering. A nominal thickness of 50-70 nm is sputter deposited following the deposition of 6 nm Nb for better adhesion of Al on SiO_2. Figure 6.7 shows AFM images of Al NW integrated into chips and Al electrodes. A detail consideration of the image reveals that the NWs are grainy in feature rather than continuous NW. Both polycrystalline and single crystalline Al NWs were reported to be synthesized and characterized in different approaches. The synthesis of polycrystalline Al NW through evaporation is reported to be granular with Ohmic behavior at room temperature [177]. However, a single crystalline Al NWs were also reported to be synthesized with stress induced technology [178, 179] and no grain boundaries were observed as per TEM observations. The Al NWs synthesized in TFF are thus expected to have oxide layer formation on the grains and grain boundaries (GBs) as the samples are processed in ambient environment condition. The presence of humidity and oxygen result in the formation of passive native aluminum oxide film [180, 181] (Al_2O_3) or even hydroxide film if the sample is placed in hot water ($Al(OH)_3$) [182]. The native oxide that could be formed in Al NWs in this case is thus believed to be Al_2O_3. The thickness of the oxide ranges from 2-6 nm depending on the hours (typically several hours) of exposure to the environment [180, 182, 183]. Such thin native oxide forms a protective layer for the interior material so that further oxidation could not happen. The schematic Figure 6.7e)-g) describes the nature of the native oxide formed besides the granular feature of the NW. The oxide thickness in grains and GBs are shown to be different. GB which is energetically favorable region for oxidation as compared to the oxidation of grains themselves. Like atoms on the surfaces, GBs are necessarily more energetic than those within the grain interior. This causes the GB to be a heterogeneous region where many processes such as corrosion, solid-state diffusion precipitation, etc. could happen. A thicker and wider oxide is thus expected across the grain boundaries.

As dimensions of conductors approach the mean free path of the electrons, the electrical resistivity of metals increases and deviates from bulk counter parts. The effects of electron scattering at surfaces and in grain boundaries are then be-

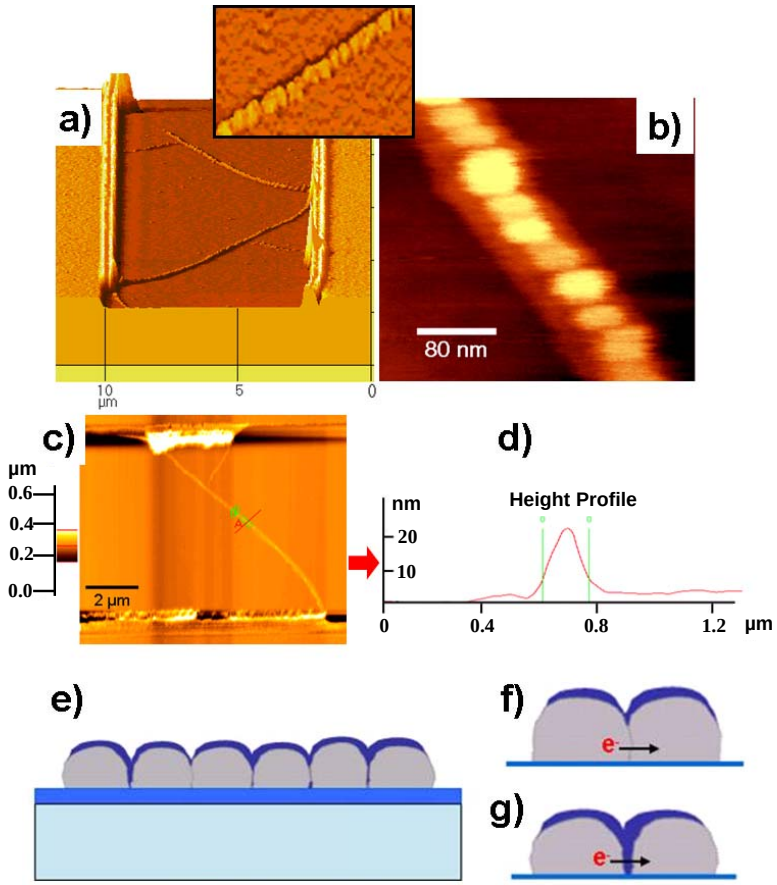

Figure 6.7: *AFM image of Al NW. a) A λ shaped 3D AFM micrograph of Al NW which is one of the typical representative shapes among others. The inset shows the rough (grainy) feature of the NW with grain boundaries that significantly affect the electrical conductance. (b) shows top view of the NW and the width of the NW is below 80 nm. c) 2D inverted λ shaped Al NW with a corresponding height profile (≈ 20 nm) and width shown in (d). The nominal thickness sputtered from the chamber was 70 nm. Schematics of Al NW grains e) on Si substrate coated with SiO_2. At ambient condition Al NW will have a thin layer of native oxide (blue colored). Two possible results could be obtained depending on the size of contact area between neighboring grains f) the oxide does not reach to the substrate and electron can only be scattered at the grain boundary (doted line between grains). In g) electrons can either tunnel or blocked in such a case.*

coming substantial [184–186]. When NWs in this case are electrically biased, the electrons are believed to encounter two kinds of barriers that cause scattering besides others: GB scattering and scattering due to the tail of native oxide reaching

down to the substrate as shown in Figure 6.7f) and g) respectively. The barrier however is not expected throughout all NWs as the NWs are quite rough, but it could only be expected at the locations where there are very small thickness or on a small GB contact areas. The electrical measurement performed for many samples processed similarly also confirm this fact. The I-V characteristics measured for such samples can show linear behavior, exponential (semi-conducting) behavior or even non-conducting behavior (where no current is actually measured). The non-conductive behavior observed is attributed to either non-connected (broken) grains that have substantially big gaps (air) for not allowing electron transfer or a thick oxide reaching to the substrate beyond the tunneling regime. If the NWs conduct and show semi-conducting I-V behavior, it can be a result from two possible NW cases. The first one could be a very thin oxide that electrons encounter and tunnel through the barrier or the second case could be that the Al NWs are so thin that surface effects and grain boundary scattering contribution are substantially low. In Figure 6.7, it was shown that Al NWs are not smooth and continuous wires but rather having grains of various size including a gap between them. The gap could be air, insulating oxide or a grain boundary. The most likely electrical conduction process in such a system is due to an electron hopping mechanism which can happen through crossing the barriers. Temperature is a key factor that can cause electron to pass through a potential barrier. Thus as the temperature of the sample is increased, the electrical conductance also increases which is shown in Figure 6.8 or a decrease in resistance as plotted in Figure 6.8b). The curve fit and its experimental plot show a power law fit equation $R \sim exp(-T)$. This result fits to Mott power law or Mott variable range hopping, which is the most suitable model to describe low temperature conduction in strongly disordered systems with localized states [79]. Previous report on the conduction mechanism of granular aluminum showed that it does not follow the Mott hopping law [187]. However, a more detailed investigation of Al NWs as given below shows that the temperature dependent resistance follows Mott's VRH.

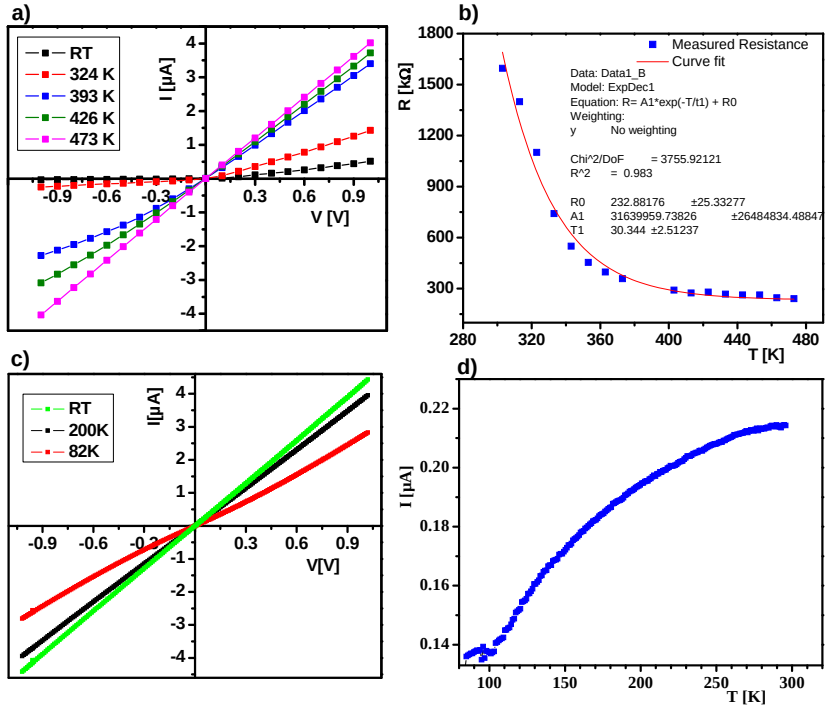

Figure 6.8: *Effect of temperature on the resistance of Al NW. a) Depicts the IV characteristics of Al NW at various temperatures and (b) shows the evolution of electrical resistance while the temperature of Al NW is increased from RT to 200 °C at the supply of constant voltage 50 mV. c) The IV characteristics of the Al NW at different cryogenic temperature when the NW is cooled down to 82 K. d) Shows current vs temperature (IT) measured at a constant voltage of 50 mV.*

6.1.2.2 Characteristics of Al NW Synthesized in MTFF Approach

As pointed out earlier, one of the challenges in large area gate field application is the dielectric breakdown. This is very common effects that is observed in many dielectric oxides such as SiO_2. According to Klein [188], maximum calculated fields for SiO_2 thin film at room temperature is found to be 9 MV/cm. The average calculated maximum field from the measurement shows that it is 0.6 MV/cm. It is also found out that the dielectric break down could happen at lower voltage for specimens and nearly all specimens have showed a breakdown even at lower voltages under cyclic biasing. The possible mechanism for dielectric breakdown could appear in three forms: single hole, self-propagating, and maximum voltage breakdowns [188]. Any form of these voltage breakdown will pause a challenge in having a stale dielectric material for application of gate electric field

in the NWs. In order to minimize the probability of breakdown by single hole or self-propagating at flaws, surface area of the dielectric gate oxide is reduced by lithographic steps together with electrochemical anodization. Figure 6.9 depicts the flow process involved in the synthesis of Al NW through MTFF approach. The first lithography is done for pattering of bottom electrode. Nb as adhesion

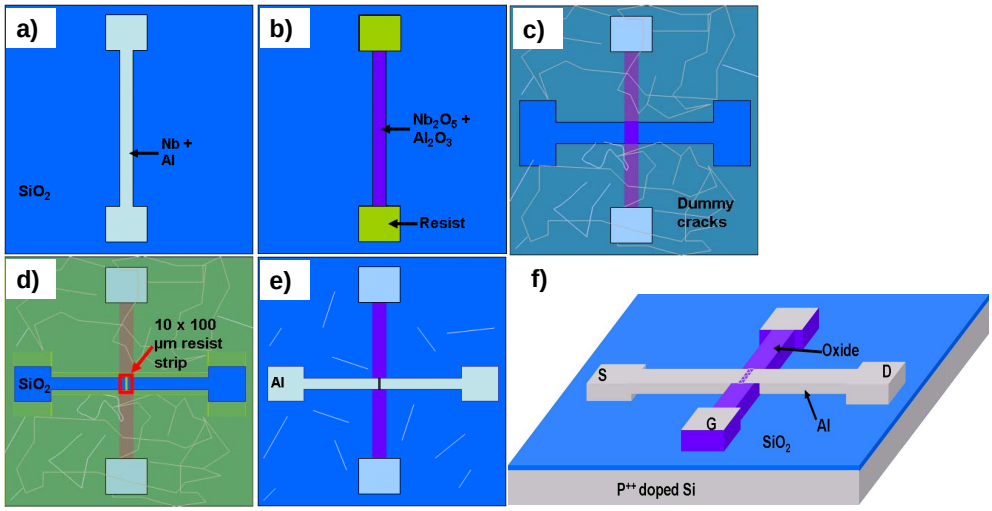

Figure 6.9: *Schematics depiction of step processing in MTFF approach a) The first lithography followed by deposition of base electrode and mask-lift off resulted a patterned base electrode. b) Second lithography for covering contact pads with resist followed by partial electrochemical anodization of the electrode. The contact pads are free of anodization because of resist. c) Third lithography followed by annealing at 50 °C and immersing into liquid nitrogen for dummy crack formation. d) Fourth lithography for forming 10 µm resist strip, annealing at 50 °C and immersing into liquid nitrogen for zig-zag crack formation. e) Finally deposition of 6/50 nm thick Nb/Al followed by mask-lift off in ultrasonic acetone bath. f) Depicts a 3D schematics of the final sample.*

promoter is used before the actual deposition of the Al electrode. To avoid any possible chemical reaction between Al and developer in later stage, 10 nm Nb is again sputter deposited on the top. The base electrode will be ready after mask-lift off in acetone bath followed by cleaning with isopropanol and deionized water. This leads us to the second lithography just to cover contact pad to avoid electrochemical oxidation in later stage which is important for later gate wire bonding as depicted in 6.9b).

The third lithography is then performed immediately after the partial elec-

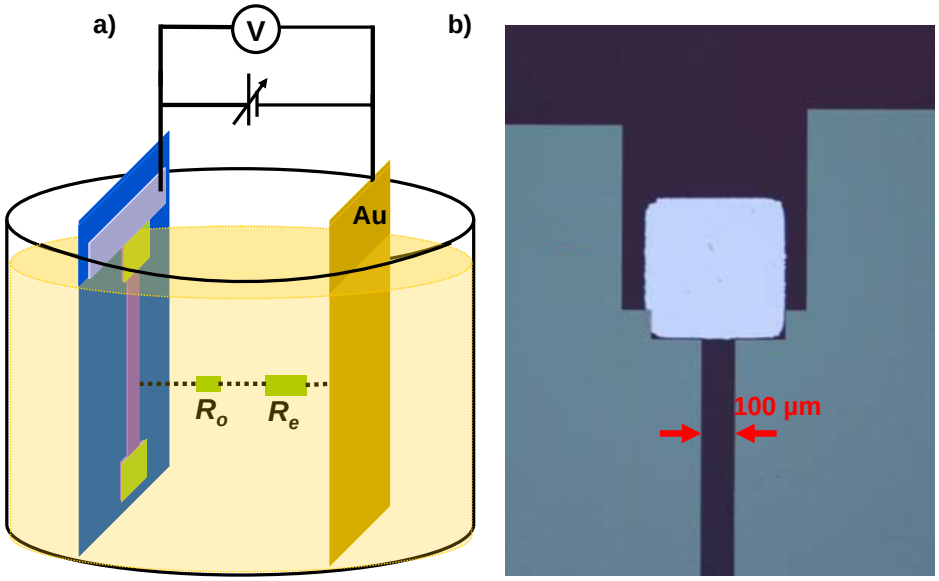

Figure 6.10: *a) Schematic illustration of the partial electrochemical oxidation of Al+Nb base electrode. The electrolyte is composed from 156 g ammonium pentaborate, 1120 ml ethylene glycol, 760 ml hydrogen peroxide and diluted in 760 g of water. The voltage is ramped to a desired value for e.g. to 33 V at an approximate rate of 1 V/s. R_o and R_e refer to the resistance that is growing in the electrode and the natural resistance of the electrolyte respectively. The optical micrograph of anodized sample at 33 V maximum voltage is shown in d).*

trochemical oxidation of the gate. It is partially anodized so that the unoxidized part will be used to apply gate voltage. The sample is then annealed in a hot plate usually at about 50 °C for 5 minutes and immersed into liquid nitrogen to form dummy cracks. The dummy cracks are intentionally produced so that the resist in the next stages of processing won't be stressed and avoids the formation of further cracks. The dummy cracks are filled with the resist in the fourth lithography (6.9d)) step and in addition, a 10 μm x 100 μm resist strip is produced where the actual NW forming zig-zag cracks were synthesized later. These cracks are produced using similar parameters as the dummy cracks are produced. Finally 6 nm Nb and 50nm Al are sputter deposited consecutively for drain (D) and source (S) electrode deposition together with deposition of NW forming material followed by careful mask lift-off.

Figure 6.11 shows actual results from the synthesized sample though pro-

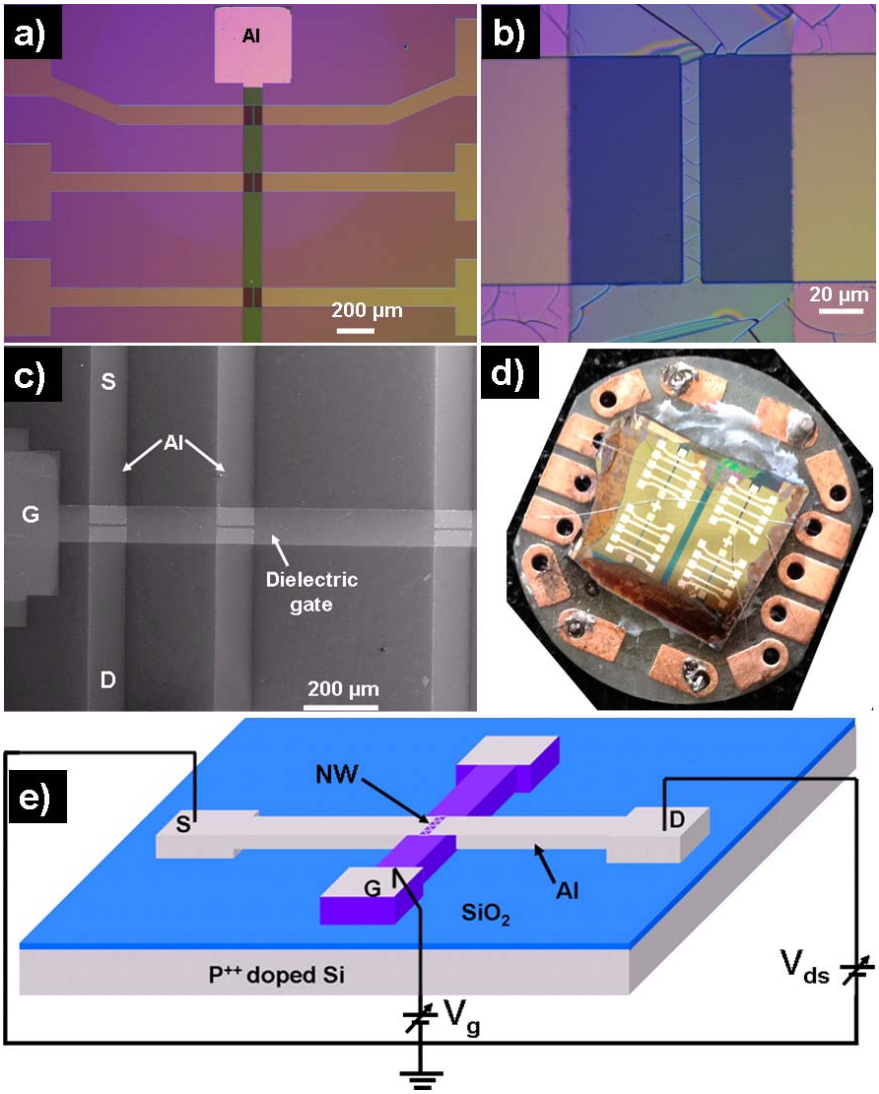

Figure 6.11: *a) Depicts optical micrograph of the sample after the fourth optical lithography. b)Optical image after zig-zag cracks are synthesized after annealing the sample at 50 °C for 5 minutes and immersing the sample in a) into liquid nitrogen for about 5 seconds. c) Depicts SEM micrograph of sample after mask-lift off. The source(S), drain(D) and gate(G) electrodes are also marked . d) Photographic camera of the wire bonded sample which is ready for electrical measurement. e) A 3D schematic depiction of the ALNWFET final device ready for electrical measurement.*

cesses described above. The contacts which were covered with photoresist remained unoxidized but the rest area is anodized as depicted in 6.11a). AZ MiR 701 is the photoresist utilized in all of the lithography steps. Zig-zag fractures are

produced as shown in 6.11b) through thermal cycling. To experimentally probe the electrical transport properties of Al NW, the Nb+Al electrodes are contacted via wire bonding to a Cu sample holder as shown in Figure 6.11d). The finished device which is ready for electrical measurement resembles the schematic depiction given in Figure 6.11e). Electrical measurements for the NWs synthesized

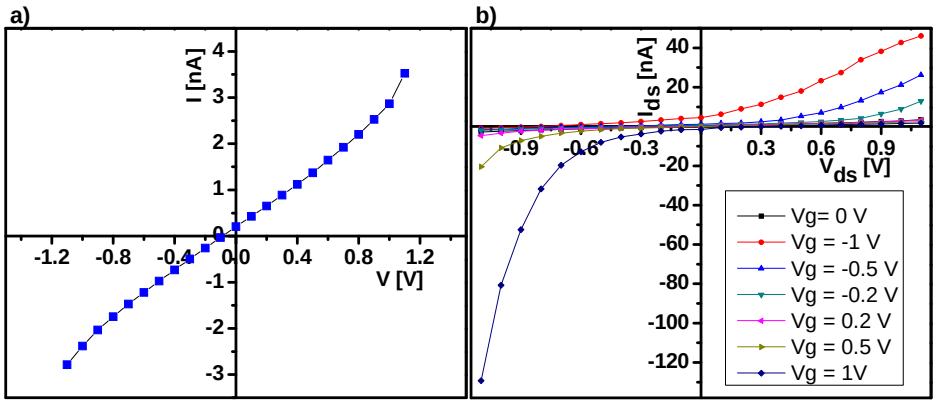

Figure 6.12: *a) Depicts I-V characteristics of 50 nm nominal thickness of Aluminum NW (AlNW) b)AlNWFET of the same NW under various gate voltages. An increase in two orders of drain current is visible.*

in MTFF approach is performed in two sets of experiment and results from two different probes are demonstrated. For the first sample (S1), DC power source is assembled with another power supply (generator) sourcing a floating gate voltage. For the confirmation of the measured result, a second set where a floating battery is used in the second sample (S2) (Figure 6.13a)). Before the application of gate voltage, an electrical test through I-V measurement is performed to check if the dielectric is leaky or not through ramping 0 to 1 volt. The maximum leakage current at 1 V was 3 pA and it is well below the noise regime (10 pA) that assures gate field could be applied to bias the NW. The I-V characteristics and measured electrical behavior with the application of localized gate voltage for S1 is shown in Figure 6.12. The drain current increases for a negative bottom gate bias field when positive drain voltage (V_{ds}) is ramped between 0-1.1 volt. The negative gate bias is found to switch off (decrease) the drain current in ramping V_{ds} in negative polarity. A reverse phenomenon happens when the polarity of the gate voltage is changed. The gate polarity favors only one directional flow of the drain current.

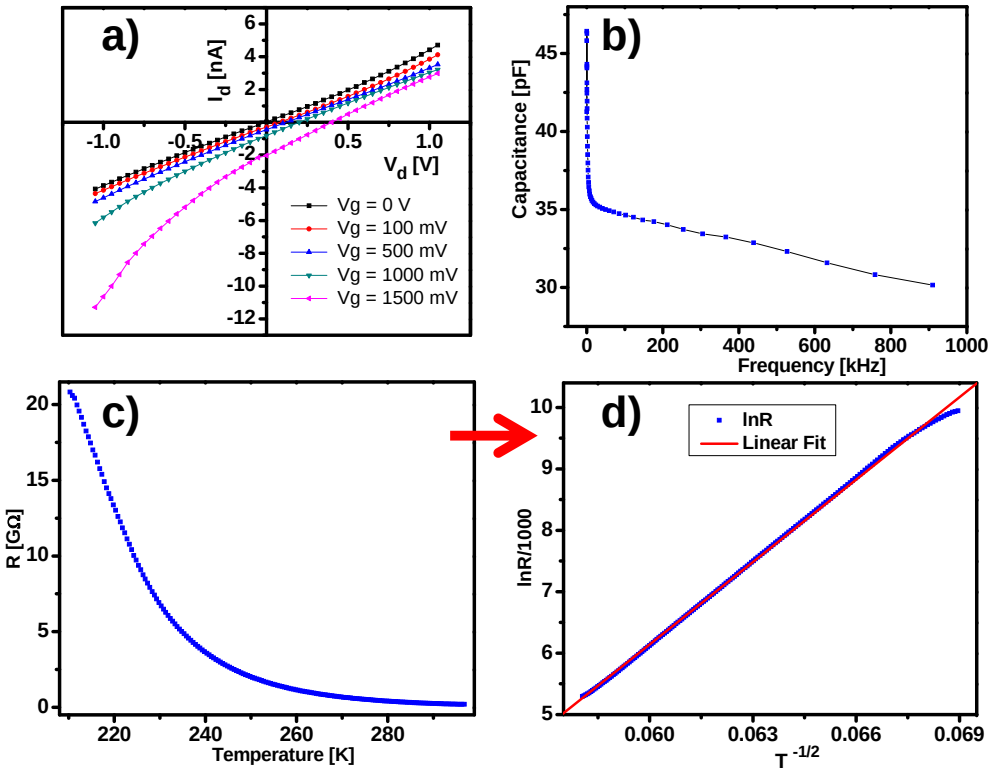

Figure 6.13: *a) Depicts I-V characteristics of Aluminum NW (AlNW), 50 nm nominal thickness at various gate voltages b)Frequency sweep of capacitance measured for the gate oxide in sample a). c) Plot of temperature dependence resistance of Al NW at 0.5 v bias voltage and its logarithmic plot (d). The resistance (red) fitted to Mott model with d=1.*

For S2, a floating battery with the same circuit setup like Figure 6.11e) is implemented in a way that gate voltage was varied using custom made circuit. Once the insulating characteristic is confirmed, several measurements including capacitance were performed which are shown in Figure 6.13. Using the total capacitance (C_T) of the capacitors connected in series (C_1 & C_2), the capacitance the gate oxide can be estimated. That is two capacitors are formed from Al_2O_3 and NbO dielectrics connected in series.

$$\frac{1}{C_T} = \frac{C_1 + C_2}{C_1.C_2} = \frac{1}{\epsilon_0 A}\left(\frac{d_1}{\epsilon_1} + \frac{d_2}{\epsilon_2}\right) \tag{6.3}$$

where $\epsilon_0 = 8.85 \times 10^{-12}\ C/Vm$, $\epsilon_1 = 9$ and $\epsilon_1 = 40$ are the permitivities of Al_2O_3 and NbO respectively from literature. $d_1 = 60\ nm$ is thickness of Al_2O_3 and

$d_1 = 20\ nm$ is thickness of NbO. A is the surface area in which the gate voltage is applied and is approximately calculated as 450 μm^2. Using these numbers into equation 6.3 yields the gate capacitance C_T to be $\approx 1\ pF$. This result is not very far from the capacitance measured in Figure 6.13b).

In section 2.4.1 of Chapter 2, temperature dependent hopping conductance for 1D nanostructure is shown. In Figure 6.13c) temperature dependent resistance measurement is also given. From the R versus T behavior, several characteristic parameters describing the charge transport in NWs can be extracted. A solid fitting is used to extract d as depicted in Figure 6.13b). It can be observed that Mott variable range hopping also fits for 1D NW. From the slope of $ln(R)$ vs $T^{-\frac{1}{2}}$, the fitting parameter T_0 between 210.3 K and 296.8 K can be estimated. The calculated value of T_0 is $4.47 \times 10^5\ K$.

6.2 Iron Oxide Nanostructures (NWs) Synthesized in TAM

Iron oxide NWs are one of the most widely synthesized and investigated materials because of the potential they offer for various applications [189]. Already in the 1950s the possibility for iron oxide NWs growth was found by Pfefferkorn [190] through investigating the growth and structures of whiskers emerging out from oxidizing iron metal foils and alloys at higher temperatures. Three years later, Takagi [191] reported blade like α-Fe_2O_3 whiskers synthesized at 400 - 800 °C in oxygen using electron microscopy and electron diffraction. He showed that whiskers grow at the tip by surface diffusion of atoms and molecules from base towards tip. Alternatively, blade like whiskers and NWs can also be synthesized from thermal oxidation of sputtered iron films [192]. The temperature and oxidizing environment are found to be the key factors responsible for changes in the morphologies of NWs. By controlling these growth parameters, NWs ranging from microsized blades to NWs could be obtained [193–195].

6.2.1 Factors Affecting Growth of Iron Oxide NWs

The growth and morphology of iron oxide nanostructure are found to be influenced by a number of factors: thickness of the iron film, temperature, duration of annealing and pre-treatment of the samples with oxygen plasma. In order to find out how the thickness of a film influences, iron film with a nominal thickness of 50, 350, 600 and 1000 nm were deposited under similar sputtering conditions. These samples were annealed on a hot plate at 300 °C for 4 hours. The SEM results obtained for these thicknesses are shown in Figure 6.14. The overall microscopic images show that there is a minimum iron film thickness required to be deposited so that long and dense nanostructures are grown. Almost no growth

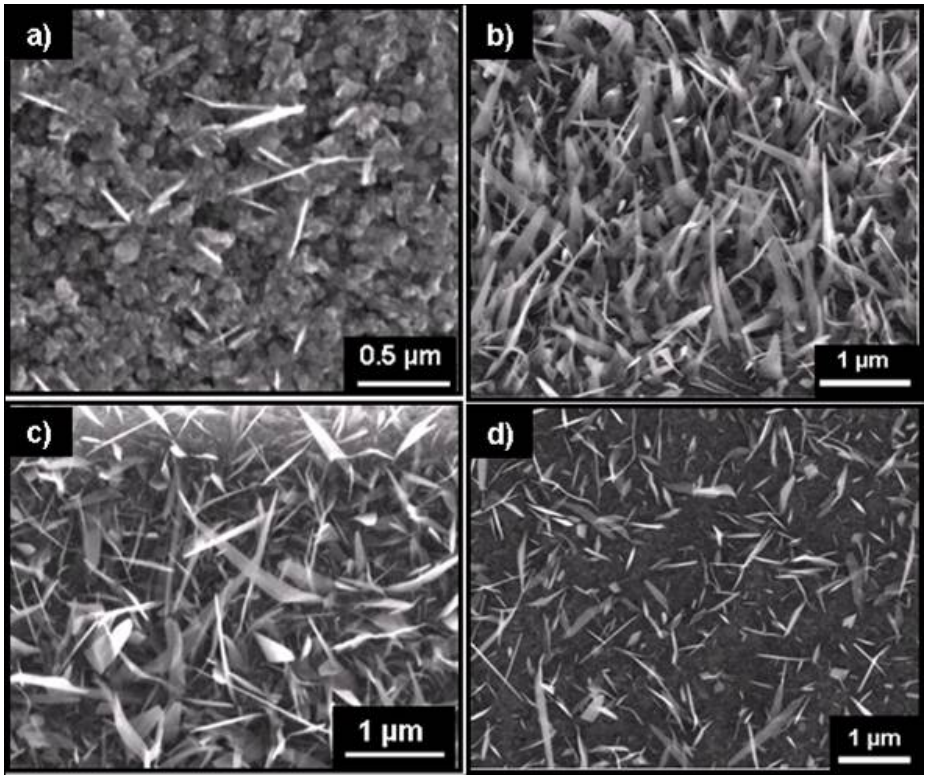

Figure 6.14: *Depicts SEM micrograph evolution and the influence of sputtered iron film thickness on the growth of iron oxide nanostructures synthesized on a hot plate at* 300 °C *for 4 hours. a) 50 nm, (b) 350 nm, (c) 600 nm and d) 1000 nm film thicknesses.*

of nanostructure (except rare 500 nm long rods) are observed when the iron film thickness is $\leq$ 50 nm. When the film thickness is 350 nm, dense and a mixture

of differently shaped nanostructures are grown. Many of the nanostructures appear to be wide at the bottom and sharp at the top resembling nano whiskers (nanospikes). A 600 nm thick film also shows growth of nanostructure which appears to be thinner and less dense as compared to the 350 nm thick iron film. The whiskers are longer and thinner for 350 nm film than 600 nm thick film and furthermore, the areal distribution (density) of whiskers at some areas for a 600 nm thick film is low. A further increase in the thickness to 1000 nm resulted in a lower areal distribution and a thinner nanostructure. The reason for this is speculated to be due to the difficulty of iron ions facing in penetrating through grain boundaries because of a thick iron layer on the top. The influence of film thickness on nanostructure growth is also reported elsewhere [196]. A thickness of 450 *nm* iron film at 300 °C annealing temperature is found to be the optimal parameter for obtaining various combinations with a longer and denser distribution iron oxide nanostructure growth. Figure 6.15 shows the influence of annealing

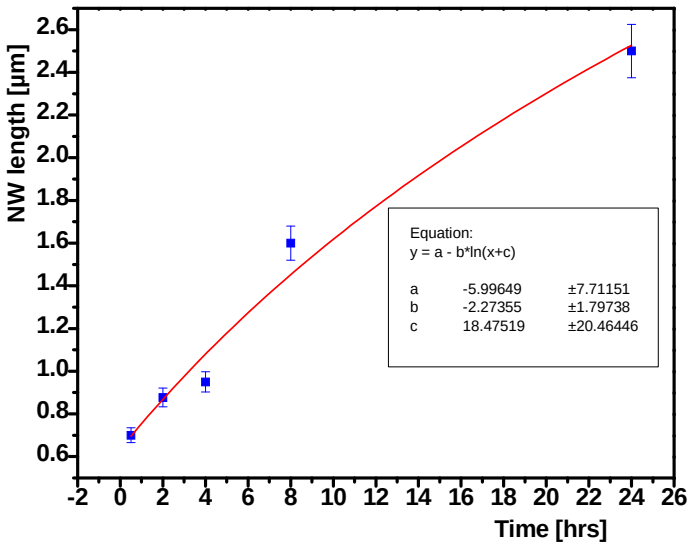

Figure 6.15: *Depicts plot of the influence of annealing time on the average iron oxide NW length synthesized in a hot plate. The plot shows that the average length is logarithmically related to the average time as shown by the curve fitting (red).*

time on the length of the nanostructure (NW) for similar samples that have 10 nm Cr, 50 nm Au and 450 nm Fe film annealed at 300 °C. The length of NWs shows a saturation with respect to annealing time as it is evident from a logarithmic time dependence. The logarithmic dependence of NW length to annealing

time was also reported else where [192]. The analysis of the data points shows that the rate of increase in length was 23 nm/min in the early stages of annealing and decays to 1.7 nm/min at 24 hrs annealing time. The contribution from iron diffusion through grain boundaries will get less and less as long as the annealing continues since more of iron gets oxidized at long annealing time.

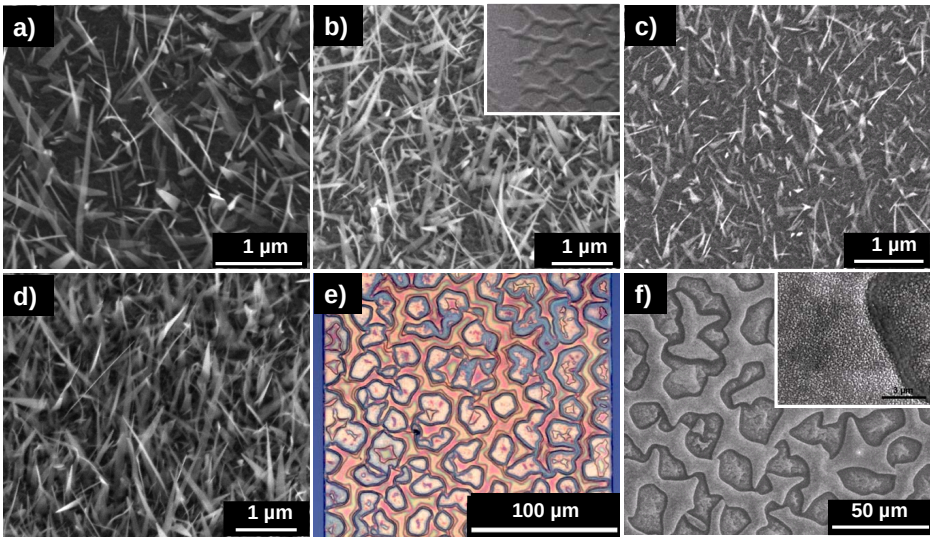

Figure 6.16: *SEM microscopy image of 450 nm thick Fe annealed for 4 hrs in a hot plate that were treated in 100 W oxygen plasma for a) 15 min b) 1 hr c) 2 hr. The inset in b) shows the buckles observed at the edge of the same sample. d) SEM image of a sample treated with oxygen for 1 hr but annealed for 8 hrs. e) and f) show optical and SEM images respectively of the sample with 220 nm thick Fe film treated in 100 W oxygen plasma for 1 hr and annealed for 8 hrs on a hot plate at* 300 °C. *Buckles are observed in this case but there are no NWs grown as shown in the inset in f).*

The other parameter that influences the growth of iron oxide NWs is the oxygen plasma treatment of the film before thermal annealing. Cvelbar [197] reported that iron oxide NWs can be synthesized by reactive oxygen plasma oxidation of iron sheet. With exothermic plasma oxidation at about 570 °C, growth of NWs was observed. Using oxygen plasma etcher, a similar experiment was performed in our multi layered samples. However, the temperature never exceeded 80 °C in the plasma and there was no any NW growth observed right after plasma treatment. The treatment however is expected to enrich the iron surface with oxygen so that a thin oxidized layer of Fe is produced. To avoid

the etching of top surface of the iron film, the chamber pressure is kept as high as possible. This will result in development of a small bias voltage between the electrodes in the plasma. However, some energy is still needed to excite the oxygen molecules in the plasma so that they can reach to the substrate. The energy is obtained through the microwave power device (at the frequency of 13.56 MHz and 100 W power). Figure 6.16 in general gives the influence of oxygen plasma treatment in the density and length of the iron oxide NWs. The longer the oxygen plasma treatment of the samples the lower are the size and density of synthesized NWs, as shown in Figure 6.16c). Although the results are not shown here, it is necessary to mention that oxygen treatments for ≥ 4 hrs showed no growth of NWs. Our speculation is that a longer oxygen plasma treatment will cause a thicker oxide layer (complete oxidation) on the film which results in not much iron ions left that could diffuse via GBs. The other important parameter which determines for the synthesis of NWs from sputtered iron film is temperature. It was found that increasing the temperature above 450 °C reduces the NW yield so much and if the temperature is increased well above 500 °C the yield will be almost zero.

6.2.2 Iron Oxide NWs Synthesized in a Hot Plate (HP)

As already said, the procedure begins with microstructural patterning (details in section 4.4.2) on a 100 nm SiO_2 coated Si chip followed by deposition of 10 nm Cr, 50 nm Au and 450 nm Fe respectively. After mask-lift off samples could be annealed as-deposited or alternatively exposed to ambient environmental condition for a while (days or some times months) or treated with oxygen plasma for intentional top layer native oxide formation. In many of the experiments annealing is performed at the optimal temperature which is 300 °C at ambient air condition. Figure 6.17 shows the AFM images of telephone cord looking buckles produced in iron oxide sample where the buckles were not completely collapsed and the aspect ratio of the buckles is approximately 10. In general, experimental results show that buckles of 0.3 to 1.5 μm height and width of 2 to 10 μm of different patterns are observed. The usual pattern observed is actually telephone cord buckle. Isolated buckles lying on the substrate separately are also observed. Different characterization results have also been found by

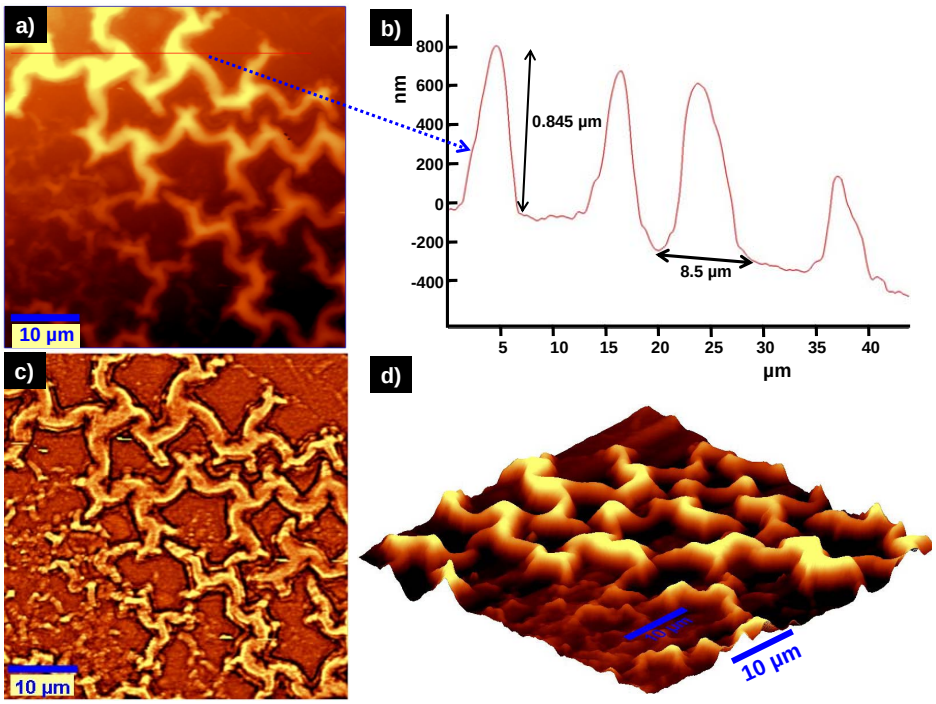

Figure 6.17: *Depicts AFM images of iron oxide buckles where the buckles were not collapsed. a) Top 2D view of buckles. The red line shows a line scan for the surface profiling and it corresponding result is shown in b). The same image is also shown in c) after averaging of the image is performed and d) shows the 3D view of the same buckles.*

using instruments such as optical microscope, SEM, TEM and EDX spectrometer. Furthermore, electrical measurements were performed across iron oxide bridged gaps and the result showed a promising result as a magnetic field sensor.

6.2.2.1 Microstructural Evolution of Iron Oxide NWs

It is evident from Figure 6.18 that a wide variety mixtures of iron oxide NWs (nanostructures) can be synthesized depending upon a number of factors where some of them are obvious and others are not till now. When the as-prepared samples are annealed (Figure 6.18b)), the synthesized NWs appear to be wider at the base (nanospikes) and sparsely populating as compared to the sample that are exposed to room air for 1 month (Figure 6.18c)) or 2 months (6.18d)). This is believed to be due to the more number of stress induced GBs that resulted from oxidation top layer of the iron film which reacts with ambient oxygen. Increased

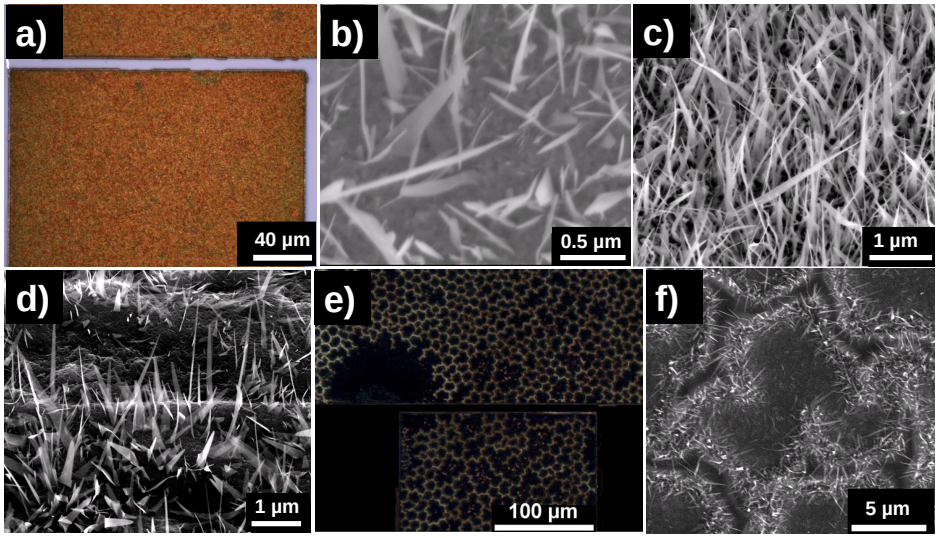

Figure 6.18: *Optical and SEM images of iron oxide. (a) The very common optical microscopy image of annealed sample. SEM image of annealed sample (b) right after mask-lift off, (c) after nearly one month stay in ambient condition, (d) after nearly two months stay in ambient condition. e) and f) illustrate DF optical image and SEM images of buckled sample annealed after two months stay on a shelf respectively.*

number of GBs will give increased number of iron ion diffusion paths which result in high density of NWs. A buckling and collapse of buckles accompanied by NW growth is the other interesting phenomena that is observed as shown in Figure 6.18e) & f). The dark field (DF) optical microscopy image shows an overview of the buckled and collapsed buckle patterns on the chip after annealing. A closer view using SEM as depicted in Figure 6.18f), shows that the collapsed buckles are bridged by nanospikes. Such a collapsed buckles are important in measuring electrical current through the nanospikes which will be shown in the subsequent sections. The NWs in the SEM pictures appear to be brighter due to the combined effect of the edge and diffusion contrast since nanostructures have really small penetration depth for electrons that causes them to appear brighter than the surface [86]. Also the ruggedness caused by the nanostructures decreases the escape distance of the incidence beam, this also contributes to the contrast of the SEM image.

The schematics in Figure 6.19a)-c) shows that with elapsing annealing time the sample undergoes buckling which later collapse and the collapsing is accom-

panied by the growth of NWs (or nanospikes). The corresponding microstructural evolution as obtained by SEM result shows a self organized buckles as depicted in Figure 6.19d) & e). Buckles are known to happen in many of thermally treated planar layer systems during device fabrication as a thin film stress relief mechanism. In addition to the intrinsic stress developed during thin film growth, thin films are subjected to high residual stresses during thermal treatment and other fabrication processes such as oxidation. The iron film which through an-

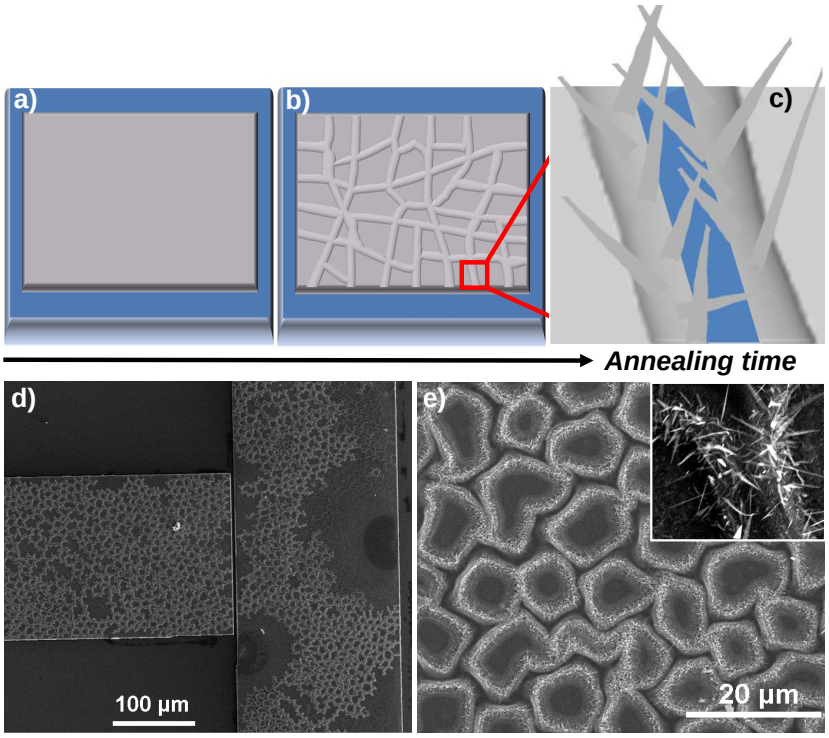

Figure 6.19: *Summarized schematic depiction of the flow process in nanostructure growth. a) A P^{++} doped Si substrate with 100 nm SiO_2 (blue color) is coated with 10 nm Cr as adhesion promoter, 50 nm Au and 450 nm Fe (gray color) by sputter deposition, respectively. b) After the mask lift-off, the sample is heated on a hot plate at a constant temperature of* 300 °C *in ambient environment that results in self organized buckles. c) A further annealing results in a collapse (fracture) of the buckles and a growth of nanospikes. d) Typical broad SEM micrograph view of buckles and nanospikes & e) shows corresponding film forming islands as a result of collapsed buckles. The inset in e) shows the nanospike bridged buckles.*

nealing changes to an oxide is typically in a state of compressive stress, as there exists a mismatch in the thermal coefficient of expansion between the substrate

($\alpha_T = 3.6 \times 10^{-6}/°C$ at 20 °C) and the film ($\alpha_T = 11.8 \times 10^{-6}/°C$ at 20 °C). The thermal biaxial stress which is corresponding to the thermal mismatch strain for the film at any temperature T can be predicted using equation 4.6, assuming elastic thermal strain and approximating the coefficients of thermal expansion constant with temperature. Considering $T_1 = 300$ °C, $T_2 = 30$ °C as if the sample is cooled down because Stoney's formula is applicable in such condition. Thus, using equation 4.5, the thermal strain in the film is calculated as -2.376×10^{-3}. Using Poison ratio $\nu = 0.29$ & the Young's modulus of the Fe which is 211 GPa into equation 4.6 results in the stress $\sigma = -0.706\ GPa$. The negative result shows that the film is under thermal compressive stress which is in agreement with buckle formation in thin film [92]. This actually is not the only stress that develops in the samples but also other stresses such as residual stresses or stresses from oxidation that contribute to the overall stress. If the sum of these stresses exceed critical values, they lead to delamination and buckle formation. In Figure 6.19d), the growth and propagation of buckles is aligned in a kind of sinusoidal or telephone cord instability until the whole film gets completely converted in a hexagonal buckle pattern through time. Each buckle allows only the relaxation of a certain amount of compressive stress in its neighborhood due to the constraints from the substrate. This explains why the buckles form a relative regular pattern. Further heating leads to collapsing of the buckle tops, opening a gap and dividing in such a manner that the film is converted into individual islands.

To estimate and explain the main reason for the formation of buckles, typical numbers such as the coefficient thermal expansion for bulk iron and the annealing temperature were used to calculate the expansion. When metallic thin films on thicker substrate are oxidized at higher temperatures, there will be a residual strain development because of thermal misfit between the film and substrate. For a typical 10 μm length of Fe film fixed at the ends, the change of length by expansion is approximately 35 nm. This number is not realistic as compared to the buckle size that are observable in optical microscope. Thus, it can concluded that the main factor for buckle formation is the increase in volume during oxidation besides the thermal misfit between the oxide layers during oxidation. However, the details are not completely understood that a thorough investigation is needed for further explanation.

6.2.2.2 TEM and EDX Analysis of Iron Oxide NWs

The SEM investigations suggested that the shapes of the majority of the NWs grown are nanospikes or blade like nanostructures that are wide at the base and narrow towards the tip with various size mixtures. High resolution-TEM (HRTEM) and scanning-TEM (STEM) measurements were also performed using a Technai F30 STwin microscope. The composition of the NWs was determined by EDX analyses in STEM mode. The corresponding results are shown in Figure 6.20. The bright-field TEM images of nanospikes at different magnifications are shown in Figure 6.20a)-b). It can be seen that the nanospike exhibits a darker contrast in the center along the entire length which could be induced by the fact that this region has a different elemental stoichiometry. The elemental stoichiometry is confirmed through a drift corrected STEM-EDX line scan measurement on a nanospike (Figure 6.20c)). In this specific specimen, the EDX result showed that the nanospike has a core-shell structure as can be seen in Figure 6.20d). In the STEM image, a bright contrast in the middle of the nanospike is observable. It is important to highlight here that the STEM images depend on the atomic mass number (Z) and thickness that affect STEM image contrast. For few nanospikes, STEM images combined with EDX line scan thus confirm that the nanospike is Fe rich in the center. The high oxygen peaks at the sides indicate that the nanospike is highly oxidized at the ages.

Crystal structure and phases of the nanostructures are the other possible material property that can be determined using TEM diffraction pattern analysis. The diffraction pattern from one of the nanostructures is shown in Figure 6.20e). A thorough investigation of many nanospikes proved that all are single crystalline, although the diffraction patterns at different locations of a nanospike appear to be different. The d-spacings and angles between the planes have been measured and are depicted on the diffraction pattern.

It has been previously discussed that the nanospikes showed non-homogeneity in the composition of iron-oxygen through TEM image mode and EDX analysis shows that atomic weight percentages are different at several locations in the nanospike. The analysis of the diffraction pattern also proved that the nanospike has no specific phase as one might expect from the synthesis technique (the expected phase is usually α-hematite). The several diffraction points taken in the

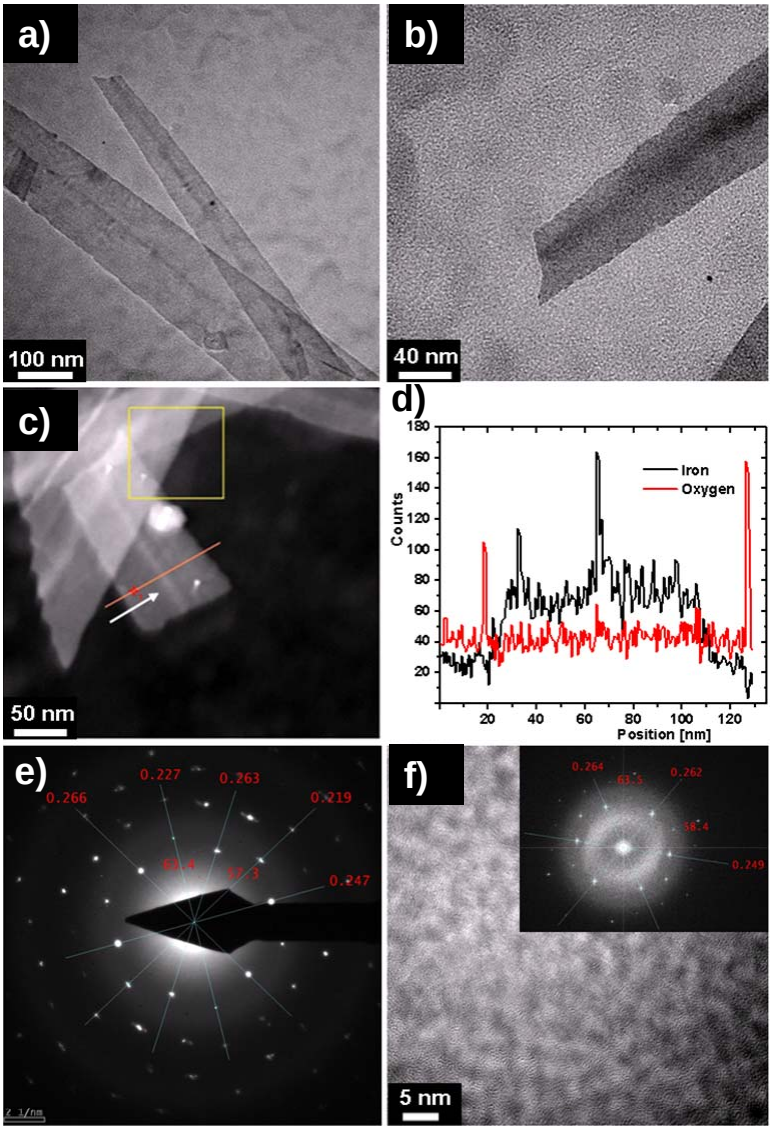

Figure 6.20: *a) Bright field TEM clearly showing a contrast between the iron rich core and the oxygen rich sides of the nanospike b) TEM micrographs of iron oxide nanospikes fabricated on a hot plate, c) EDX line scan: the yellow box indicates the reference image used in the EDX measurement. The arrow shows the direction of the scan where the spectrum from 0-130 nm is measured and d) EDX line scan profile of iron and oxygen along the nanostructure. The profile of iron has got highest peak in the middle of the nanostructure, decreasing to the sides, where the oxygen content is the highest. e) Electron diffraction pattern (DP) from one of the nanospikes. The angle between planes of diffraction and the d-spacings are also measured. In f) HRTEM micrograph and the corresponding FFT pattern in the inset are depicted. The measured d-spacings and the angles between the planes are depicted in the inset in f).The TEM characterizations shown are performed by MSc. Burak Erkatal in the group of Prof. Dr. Lorenz Kienle (Department of Synthesis and Real Structure).*

structure do not fit the hematite phase of iron oxide as can be seen from Table 6.1 and not to the other phases of iron oxide either. In relative terms, the d-spacings

Experimentally measured d-spacings (Å)	**Hematite (Å)**	**Magnetite (Å)**	**Iron (Å)**	**Wustite (Å)**
2.66	3.68	4.85	2.03	4.01
2.47	2.70	2.97	1.43	3.07
2.27	2.52	2.57	1.17	2.66
2.19	2.21	2.42	1.01	2.44

Table 6.1: *Comparison of the measured d-spacings from the diffraction pattern with d-spacings from the literature (ICSD) of known iron oxides and raw iron are depicted*

of hematite approximately fit to most of the measured values as compared to the other phases. It can be thus roughly estimated that hematite phase is the major constituent of the nanospike. As some of the the d-spacings also fit to other phases such as wustite, the nanosspike is believed to be having a combination of wustite and many other phases. The FFT pattern of an HRTEM micrograph at a random place on the nanospike is shown in the inset Figure 6.20f) for comparing the FFT pattern to the diffraction pattern and the measured d-spacings. The FFT patterns which have d-spacings of 0.264 nm, 0.262 nm, 0.249 nm and respective angles between the planes of 58.4° and 63.5° found to correlate with the measured d-spacings and angles in the diffraction pattern given in Figure 6.20e). The FFT patterns observed at various locations on the nanospike displayed that the ring in the middle of the FFT pattern is changing at different locations. This gives a hint that the nanospike has a different width profile.

Although the TAM synthesis technique of NWs is known for more than 50 years, the growth mechanism of spikes is still under ongoing discussion. A number of hypotheses such as grain boundary diffusion, screw dislocation centered tunnel [194, 198], surface diffusion [191] and even a combination of all defects [193] to account for growth of NWs under gaseous environmental annealing. There is also a recent report suggesting that the growth of iron oxide nanospikes do not take place on the grain boundary regions but on the grains themselves [199]. The α-Fe_2O_3 grains serve as nucleation centers that are fed by iron ions through surface diffusion driven by concentration gradients of iron besides the iron ions diffusion through neighboring grain boundary areas. In contrary to this, TEM

and EDX results support the hypothesis that the growth of nanospikes start to emerge on grain boundaries, as schematically shown in Figure 6.20a). From

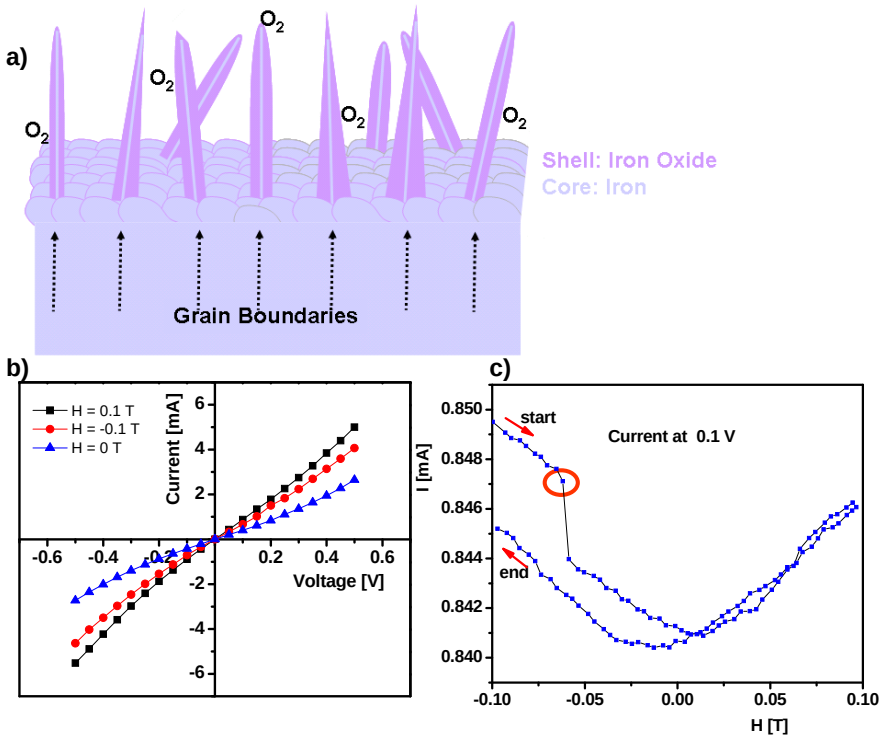

Figure 6.21: *a) Schematic of growth model of iron-iron oxide core shell nanostructures. The arrows show iron ion diffusion in GBs of the polycrystalline iron film when heated in air. The GB diffusion results in grown core-shell structures along the GBs. The GBs seem to extend along the NWs providing a further path for the diffusion of iron from the bulk up to the very end of the NWs. b) I-V characteristics of FeO-nanostructure under the influence of a magnetic field. An increase in current can be observed, when a magnetic field is applied in both directions. c) Electric current under the influence of an in plane magnetic field to the sample with (direction only switching by 180 degrees). The swing of the curve is speculated to be the result of a TMR effect. The red marker in c) shows the point when two nanospikes from separate islands are possibly untouching during measurement.*

the structure zone model (SZM) [200] of thin films, the here grown as-deposited thin film is polycrystalline in nature with a high density of intrinsic defects and GBs oriented in various directions. When this film is heated on a hot plate in air environment, growth of core-shell nanowires can be understood in terms of surface oxidation and grain boundary diffusion [201]. During heating, the surface

of the film starts oxidizing due to the presence of oxygen in the air and the assumption is that the development of a large electric field between the interior iron and top iron oxide layer as well as the thermal budget are responsible for the growth of FeO core-shell structures (FeO-CSS). It has already been reported that an electric field strength in the order of 10^6 Vcm^{-1} also develops between the underneath iron and the top oxidized iron layers. It could be possible that the electric field developed is capable enough to relieve the iron ions from the bulk and induce diffusion along the existing grain boundaries. In addition to this, the stress developed by volumetric changes in oxidation will induce a higher dislocation density especially at the edges of the collapsed buckles, where a high stress concentration and plastic deformation is observed. This will cause an increase in grain boundaries resulting in short-circuit diffusion of Fe ion along the entire length of the NWs. The high density of FeO-CSS around collapsed edges can be explained as a result of many grain boundary that are induced by the net thinfilm stresses developed. With elapsing annealing time, the upward diffusion of iron ions within the grain boundaries and subsequent oxidation(lateral NW growth) continues. During the process, initially iron oxide nano whiskers are formed corresponding to each grain boundary opening. But due to the large migration of iron atoms along the grain boundaries, not all the iron ions are oxidized and core shell NW structures are formed. As depicted in the schematic drawing in Figure 6.21a), the core is iron and the shell is iron oxide as confirmed experimentally by TEM studies. It seems that the growth direction of FeO-CSS is mainly governed by the grain boundary openings which are not always vertical but in most of the cases inclined at certain angles. Depending on the gap width and FeO-CSS density, there is a high probability for two FeO-CSS to join together and act as conductive bridge over the gap. In the present case this concept has been used as electronic circuit.

6.2.2.3 Electrical and Magnetic Measurement of FeO-CSS

Figure 6.21b) shows the electrical conductance that has been measured between islands where inter-bridging is expected to happen via FeO-CSS. The normal I-V curve (at zero magnetic field, H = 0) shows a slight rectifying behavior. The influence of magnetic fields on the electrical current in synthesized nanowires at

constant voltage were performed by a custom made TMR set-up with Bruker B-E 10f electromagnets that are capable of producing a magnetic field with a maximum field strength of 1.5 Tesla. The contact needles made of gold-plated beryllium copper are used for the electrical measurement using a Keithley 2400 source meter. In the presence of a magnetic field of 100 mT, the most responsive devices show a drastic increase in conduction by a factor of 1.5 - 2, irrespective of the orientation of the magnetic field. Figure 6.21c), where the electric current under a constant voltage and at a variable magnetic field is shown, gives a hint on the mechanism. The electrical conductance measurement shows a slight but continuous increase in current which might be due to a TMR effect mechanism, and a larger increase by discrete jumps. An explanation for the jump could be the connecting and disconnecting of individual FeO-CSS while the measurement is performed. Future experimental analysis, however, have to be performed for better understanding of the transport mechanism.

6.2.3 Iron Oxide NWs Properties from Muffle Type Furnace (MTF)

Like the case in the hot plate approach, 10 nm Cr, 50 nm Au and 450 nm Fe film are sputter deposited respectively and after mask-lift off, annealing at various temperature follows in MTF. As already said in the beginning of this chapter, the MTF is only different from a hot plate since MTF offers limited access to ambient air which is constrained by a 2.4 cm diameter hole at the back of the furnace. Besides that MTF provides an opportunity to anneal the samples to a various temperature ranges starting from room temperature up to thousands of degrees. The annealing temperature however, has been limited to 500 °C since the growth of NWs can only be established below this temperature. Figure 6.22 depicts the nanostructure obtained through annealing at 375 °C for about 6 hrs. The synthesized NWs of shown Figure 6.22b)-c) depict various size mixtures of nanospikes. A nanospike of maximum length 4 μm is observed and during SEM and TEM imaging, many of the nanospikes are found flexible. This is confirmed during the hitting of a single nanospike with focused electrons. In this condition the nanospike is found to be either bending or vibrating. This characteristic of the nanospikes nevertheless pauses a problem during capturing SEM and TEM

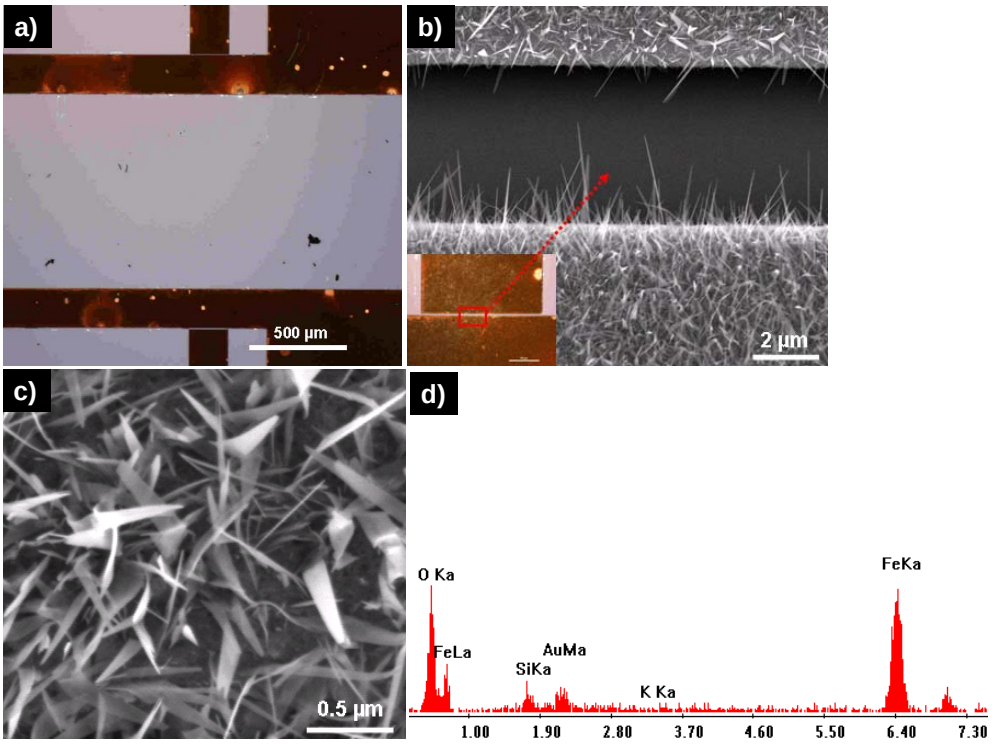

Figure 6.22: *A multilayer deposited film where 450 Fe film is at the top annealed at* 375 °C *for 6 hrs in a MTF. a) Depicts optical image of the sample and the color shows the oxidation of the film. b) SEM images of the same sample where the image is taken between the electrodes (gaps) of the patterned sample and shows the nanostructures that are shorter than gap length. A dense nanostructure growth is observed at the lower electrode also. c) High magnification SEM image taken at random position in the lower electrode shows nanospikes of various mixtures. d) EDX spectrum revealing that the nanostructures are composed of Fe and O elements (the Si and Au peaks are believed to come from the scratched Si substrate and electrode respectively).*

images of the nanospike. Figure 6.22d) is the EDX spectrum measured across the nanospikes. There are two peaks visible, which correspond to Fe and O (the Si peak is believed to come from the scratched Si substrate and Au from the scratched electrode). In the EDX analysis of single nanospikes, the quantitative measurements revealed no evidence on the existence of S, N and C, although the nanospikes grow under the ambient condition which the constituent gases include CO_2, N_2, SO_2 and H_2O. Fu et al., also synthesized iron oxide NWs from ambient annealing of pure iron and reported similar results [195].

6.2.3.1 TEM Analysis of FeO Nanospikes

The HRTEM micrographs and corresponding FFT (Fast Fourier Transform) patterns from selected areas of a nanospike are shown Figure 6.23. There are many dark spots on the nanospike as can be observed in Figure 6.23a). The EDX point

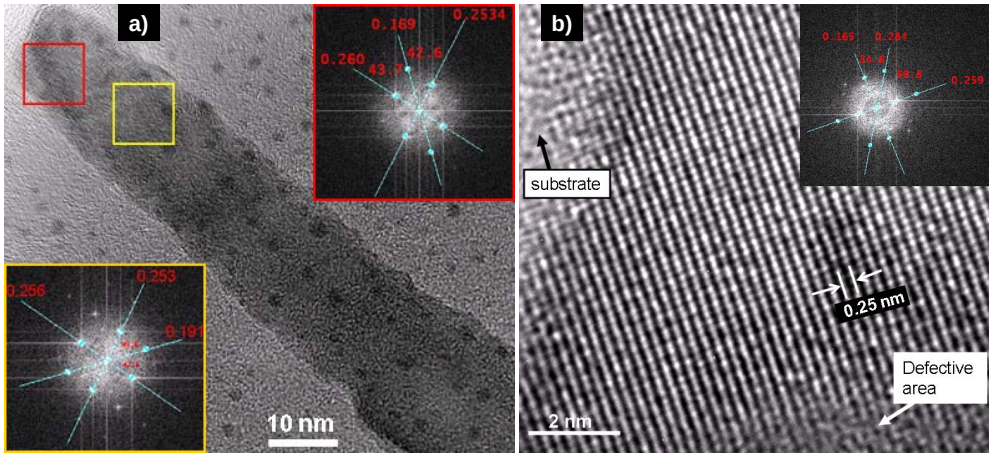

Figure 6.23: *HRTEM micrograph of a nanospike: the FFT pattern of a selected area with red box on the nanospike is depicted on the top-right corner. Similarly FFT pattern of a selected area with yellow marked box on the nanospike is shown in the lower-left corner. b) A magnified HRTEM micrograph on a selected area of nanospike in a) depicting crystalline and defective area (non-uniformity) in the crystal structure of the nanospike. The inset shows the FFT pattern in some selected area of the nanospike.*

analysis of the dark spots on the HRTEM image showed that the dark spots are gold particles which are thought to be present from the scratching of the sample during the TEM sample preparation process. The areas where the FFT patterns obtained are shown in the insets at the lower left and top right corners. The d-spacings in real space and the angles between the planes are also calculated, and are depicted on the FFT patterns. The d-spacings for the inset in the red box are measured to be 0.169 nm, 0.260 nm and 0.253 nm. The angles between the planes are measured as 43.7° and 42.6°. Similarly, the inset in yellow box gives FFT patterns with d-spacings and angles between the planes 0.191 nm, 0.253 nm, 0.256 nm and 47.6°, 47.6° respectively. The divergence in the d-spacings between the two regions can be caused by the growth of the different grains in dissimilar zone axis. A magnified HRTEM micrograph in Figure 6.23b) also shows lattice

resolved TEM on the same nanospike where regular periodicity and defective regions are observable. One of the interplanar spacings is about 0.25 nm which corresponds to one of the planes of α-hematite. The measured d-spacings on the FFT pattern are 0.165 nm, 0.284 nm and 0.259 nm. The angles between the planes are measured as 34.6° and 59.8°.

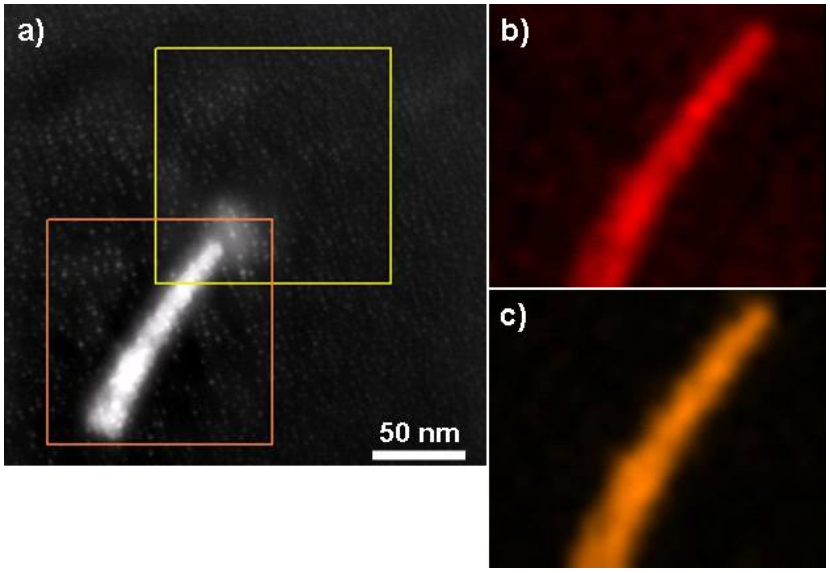

Figure 6.24: *Drift corrected spectrum images of a nanostructure. (a) STEM micrograph of the nanostructure, where red box indicates the area of interest and yellow box is the reference image. (b) illustrates the oxygen K-map and (c) is the iron K-map.*

Elemental mapping of the nanospikes in STEM mode is also performed. The STEM oxygen and iron elemental mapping of the nanospike synthesized in MTF is depicted in Figure 6.24. From the spatial distribution of the iron and oxygen in the nanostructure can be observed, it can be noted that the nanostructures are iron oxide in nature. Though the z-contrast (atomic number contrast) on the STEM micrograph shows no uniform contrast, this can be observed also from the iron and oxygen elemental maps. This contrast in the STEM micrograph and the elemental maps is due to the inhomogeneous distribution of the respective elements. The STEM micrograph also hints on the shape of the nanostructure which is of a nanospike or nanosail. In the picture, the tip of the nanostructure appears to be blurred due to the focused incident beam at this region prior to the EDX measurement.

6.3 Summary

This chapter has introduced the versatile TFF and TAM approaches and discussed the details on the fabrication of metal-metal oxide hybrid nanostructures (NWs) integrated into microchips. The unique nanostructures growth and the mechanism of growth in both cases is proposed. Also the outcome of some preliminary experimental results demonstrate the potentials of the methods to develop devices for future nanoelectronics is presented.

Nearly all materials can be converted into NWs as far as the source materials are able to be sputtered deposited or evaporated into the fractured resist template. Horizontal NWS from Ti, Al, Au and Pd synthesized using TFF approach were demonstrated. One of the most important feature of all these NWs is that they all exhibit granular feature. This characteristics of the NWs make them suitable for sensoric application. Examination of results from TFF signify that the field effect observation for the anodized Ti NWs potentials which could serve as active transistor materials and oxygen gas sensor. The preliminary electrical measurements Al NWs synthesized in both TFF and MTFF approach also showed a promising result as Al NWFET. The temperature dependent electrical measurements also confirmed that the conductance follows Mott variable range hopping that fits to 1D NW.

With TAM, a simple method of synthesis of iron oxide nanospikes integrated into chips were also presented. Ambient air condition annealing leads to a self organized thin film reorganization by micro and nanostructuring processes. Buckle and collapse of buckles are some of striking phenomenon that are observed in the synthesis of NWs in hot plate. The overall evolution of the buckles and nanospikes seem to follow neither bottom up nor top down approach, but rather a reshaping of a thin film that NWs finally evolve out of it. The edge of the collapsed buckles is also accompanied with the highly dense NWs growth where separate island are formed and bridged with nanospikes. The self-organized islands allow for an electrical measurement through the core-shell growing from edges of the island and convert to magnetic field sensor device as preliminary result shows. The film thickness, temperature, duration of film annealing and oxygen plasma pre-treatment of the film before annealing are found to be the key factors influencing the synthesis of NWs. An optimal thickness of 450 nm

and optimal temperature of 300 °C are found to provide high areal density and long iron oxide nanospikes. The length of NWs are found to be dependent on the annealing time logarithmically. Annealing temperature above 500 °C is found to result in no iron oxide nanostructure growth.

All iron oxide nanospikes synthesized through annealing Fe film in a hot plate for about 7 hours are found to exhibit a contrast difference in STEM mode ananlysis. The TEM and HRTEM analysis demonstrate that the NWs are single crystalline with a combination of many phases or superstructures. As many of the d-spacings measured in diffraction pattern coincide with the lattice spacings of α-Fe_2O_3 (α-haemetite) phase, α-haemetite is believed to be the dominating phase. A non-homogeneity in the Fe-O stoichiometry is the other experimental result confirmed through TEM image mode and EDX analysis signifies that atomic weight percentages are different at several locations on the nanospike. Core-shell, nanospikes where the center is iron rich region are also observed for majority of the nanospikes in few specimens synthesized in 7 hours annealing time.

7 Summary and Outlook

Both the high demand in the downscaling of electronic devices and the novel properties of NWs as a result of their high surface to volume (S/V) ratio and their quantum mechanical properties have driven NWs to be among the favorite research areas in recent years and are expected to remain one of the hot topics in the next decade. Thus the synthesis of NWs which is under intensive study is not only aimed at basic research but also for a wide spectrum of device fabrication and applications.

The aim of this research is to explore simple synthesis techniques of metal oxide (semiconductor) and metal-metal oxide hybrid nanostructures with proper contact lines on different substrates and investigate NWs for various device applications. In general, three synthesis routes (approaches) were developed and utilized in this thesis: Thin Film Fracture (TFF), Flame Transport Synthesis (FTS) and Thermal Annealing Method (TAM). Based on the synthesis technique, FTS is further categorized in to Crucible based FTS (C-FTS) and Burner based FTS (B-FTS). As compared to many other synthesis techniques, these synthesis techniques are cost effective, can be scaled up, offer a less complex synthesis processes and easy integration of NWs into a lithographically microstructured chips.

It is believed that the NW synthesis methods in this study offer an attractive integration route that adds minimal additional fabrication steps to the synthesis processes compared to many processes described in literature. In TFF and TAM approach for instance, a single deposition step allows for both the synthesis and integration of NWs directly on to chips. Two processing steps are however required in C-FTS and B-FTS approach: electrode deposition and NW material deposition. The direct fabrication of NWs between the contacts on microstructured Si-chips is more effective than the fabrication of contacts after the NWs synthesis as it avoids any possible damage or contamination of the NWs.

Processing on the already installed NWs paves a way for possible changes in the NWs characteristics in general. All of four NW synthesis approaches are compatible either with the already structured circuits or allowing a further micro structuring of the circuit elements after the installation of NWs. Although significant advances have been made in NW synthesis and integration, it seems that there is still a wide gap in the utilization NWs as devices in the market because of problems related to well controlled mass fabrication and integration. These challenges still open gaps between NWs and the market and they need to be solved through optimization of the factors that are essential to integration of NWs and meeting the requirements mentioned above.

The synthesis routes FTS (C-FTS & B-FTS) and TFF are used to fabricate semiconductor ZnO nanostructures with promising results as UV detectors that are in principle ready for upscaling. Unlike many other techniques, all these synthesis routes offer an *in-situ* integration of nanostructures into micro-patterned chips without additional processing steps. Many other fabrication techniques normally require several processing steps and require facilities such as high vacuum. Integration of the nanostructures into chips, nanostructures binding and interface qualities are also the main issues among many. When nanostructures separately grown and dispersed on contacts, they form gaps due to the different inherent roughnesses of contact and nanostructure surfaces. But a direct growth and integration leads to a tight interface between nanostructure and contact pad material. The two FTS variants (B-FTS & C-FTS) allow an integration of a 3D network type of ZnO nanostructures with tight interface between nanostructure and contact pad material that are interesting for UV photodetector applications. The B-FTS results proved that it clearly outperformed C-FTS in terms of synthesis time and device performance. The overall device synthesis process in B-FTS takes 3-5 seconds with estimated crystal growth time of milliseconds range. The synthesis process in C-FTS takes 0.5 to 4 hours which is much longer than the synthesis time in B-FTS. It was also shown that ZnO nanotetrapods networks synthesized in B-FTS approach are found to exhibit very fast time constant ($\sim$30 ms) and a very good on/off ratio (4.5×10^3 at 2.4 V). As revealed by the high magnification SEM images, many of nanotetrapod arms are not perfectly interpenetrating (offering low dark current) and it can be concluded that these types of nanojunctions formed between nano-microstructures in the network bridge play

a significant role in the photodetection mechanism of such photodetectors.

TFF approach is another alternative route employed to fabricate horizontal ZnO NWs that come up with a fast UV detection ability as shown by the preliminary test. The AFM images revealed that the ZnO NWs are rough and exhibit grainy feature with a probable discontinuity (gap) between consecutive grains. Both as deposited ZnO NW and film have also shown no conductance. However, annealing above 300 °C in ambient conditions for an hour resulted in more smooth morphology with a significant change in conductance in both the film as well as the NW. Although a TFF synthesized ZnO NW demonstrated promising result as a UV sensor, more investigations need to be performed. The structural quality of ZnO NW has important influence on the functionality as indicated by fast UV response. It was mentioned that nearly all materials can be converted into NWs as far the source materials are able to be sputter deposited or evaporated into the fractured resist templates. Horizontal NWs from Ti, Al, Au, Pd and ZnO synthesized using TFF approach were demonstrated. One of the most important feature of these NWs is that they all exhibit granular structure. This characteristics makes them suitable especially for sensoric applications. Further more the shrinking of Ti NWs through electrochemical oxidation in a controlled manner has been demonstrated and converted to NWFET. Partial conversion of the metallic Ti grains in the NWs into TiO_2 allowed for the formation of hybrid devices with interesting field effect properties. Al NWs that are synthesized in TFF and MTFF approach were also characterized and their potentials as a NWFET have also been demonstrated. The synthesized devices and measurements have shown the feasibility of the synthesis approaches in a wafer-level processing and the NWs showed promising potential for photodetectors or gas sensors. However, for a NW sensor a control electronics should be integrated, for example, for sensor drift correction and selectivity, as well as long-term stability tests have to be carried out.

The other novel approach for the chip integrated synthesis of iron oxide nanostructures with various and unique characteristics is TAM. This is a simple method for the synthesis of iron oxide nanospikes integrated into chips. Self organized nanospikes are synthesized through thermal annealing of Fe thin film which are believed to be due to reorganization the thin film by micro and nanostructuring processes. A muffle type furnace and a hotplate (HP) heating instruments

were used for the synthesis at ambient condition. A more detailed investigation however is performed in a HP synthesis where various characteristics of iron oxide are measured. An optimal thickness 450 nm Fe film with 50 nm Au at bottom, optimal temperature 300 °C and 4-8 hours annealing time are found to provide high areal density and long iron oxide nanospikes. The length of nanostructures are found to dependent logarithmically to annealing time. Both annealing temperature above 500 °C and annealing time below 10 min are found to result no iron oxide nanostructure growth. In a HP, both buckle and non-buckle accompanied nanospike synthesis of the nanostructures are observed. The synthesis and the overall evolution of the buckles and nanospikes seem to follow neither bottom up nor top down approach, but rather a reshaping of a thin film that nanostructures finally evolve out of it. In general the film thickness, temperature, duration of film annealing and oxygen plasma pre-treatment of the film before annealing are some of the influencing factors found out in the properties nanostructures.

All the iron oxide nanospikes synthesized through annealing Fe film in a HP for about 7 hours exhibit contrast difference in STEM mode analysis. The TEM and HRTEM analysis confirmed that the nanostructures are single crystalline with a combination of many phases or superstructures. Many of the d-spacings measured in the diffraction patterns coincide with the lattice spacings of α-Fe_2O_3 (α-haemetite) phase and thus α-haemetite is believed to be the most dominating phase. A non-homogeneity in the Fe-O stoichiometry is the other experimental result confirmed through TEM image mode and EDX analysis that atomic weight percentages are different at several locations on the nanospike. Core-shell nanospikes where the center is iron rich region are also observed for some nanospikes. The synthesis of buckles and buckle failure with dense nanospike growth at the edge of each buckles allowed the interconnection of islands through core-shell iron oxide nanospike bridges. A preliminary electrical measurement test using the self-organized islands under magnetic field demonstrated the potential of TAM to fabricate a magnetic field sensor.

Recent experimental developments in iron oxide nanopsikes investigations demonstrated that the nanospikes have got a contrast difference in STEM mode because of a thickness difference. The diffraction patterns of the nanospikes at different tilt angles series also exhibited the patterns fit to the known α-haemetite phase but with additional reflections. This shows that the nanospikes

have got multiple phase or they are α-haemetite superstructures. The growth mechanism of iron oxide nanostructures seems to be under strong debate and it is believed that the characteristics iron oxide nanospikes here will provide additional inputs on the growth mechanism. Based on the results presented, the mechanism of the nanopikes growth is proposed. Further experimental investigations have to be performed in order to maintain reproducibility in terms of synthesis and understanding the basic mechanism of iron oxide nanostructures growth.

Bibliography

[1] C. M. Lieber and Z. L. Wang,
MRS Bulletin **32**, 99 (2007).

[2] X. Duan, Y. Huang, Y. Cui, J. Wang, C. M. Lieber,
Nature **409**, 66 (2001).

[3] E. D. Minot *et al.*,
Nano Lett **7**, 367 (2007).

[4] Y. Li, F. Qian, J. Xiang, C. Lieber,
Materials Today **9**, 18 (2006).

[5] S. V. Rotkin and K. Hess,
NSTI-Nanotech **2**, 37 (2004).

[6] D. Gedamu *et al.*,
Phys. Status Solidi B **247**, 2571 (2010).

[7] W. Lu,
In *Electron Devices Meeting (IEDM), IEEE International* pages 1–4 (2009).

[8] S. A. Dayeh *et al.*,
Small **3**, 326 (2007).

[9] C. P. Liu *et al.*,
Appl. Phys. Lett. **100**, 243102 (2012).

[10] M. Law, L. E. Greene, J. C. Johnson, R. Saykally, P. Yang,
Nature materials **4**, 455 (2005).

[11] P. Krogstrup *et al.*,
Nature Photonics **7**, 306 (2013).

[12] J. Jean *et al.*,
Adv. Mater. **25**, 2790 (2013).

[13] A. K. Wanekaya, W. Chen, N. V. Myung, A. Mulchandani,
Electroanalysis **18**, 533 (2006).

[14] M. Kanellos,
Electronics. Retrieved 2009 (2005).

[15] D. C. Brock., editor,
Understanding Moore's law: four decades of innovation
(CHEMICAL HERITAGE PRESS,, 2006).

[16] In *ITRS* (2011).

[17] R. Martel, T. Schmidt, H. R. Shea, T. Hertel, P. Avouris,
Appl. Phys. Lett. **73**, 2447 (1998).

[18] S. V. Rotkin and K. Hess,
Appl. Phys. Lett. **84**, 3139 (2004).

[19] H. Cheng, C. Andrew, M. Alkaisi,
Microelectronic Engineering **83**, 1749 (2006).

[20] W. Arden *et al.*,
Technical report CATRENE Scientific Committee (2011).

[21] M. H. Huang *et al.*,
Science **292**, 1897 (2001).

[22] J. T. Hu, T. W. Odom, C. M. Lieber,
Acc. Chem. Res **32**, 435 (1999).

[23] S. Geburt *et al.*,
Nanotechnology **23**, 1 (2012).

[24] F. Schlottig, M. Textor, N. D. Spencer, K. Sekinger, F. Ochanda,
Fresenius J. Anal. Chem. **361**, 684 (1998).

[25] O. Rabin *et al.*,
Adv. Funct. Mater. **13**, 631 (2003).

[26] L. Shi, C. Pei, Q. Li,
Cryst. Eng. Comm. **12**, 3882 (2010).

[27] J. D. Holmes, K. P. Johnston, R. C. Doty, B. A. Korgel,
Science. **287**, 1471 (2000).

[28] E. C. Greyson, Y. Babayan, T. W. Odom,
Adv. Mater. **16**, 1348 (2004).

[29] H. T. Ng *et al.*,
Nano Letters **4**, 1247 (2004).

[30] R. S. Wagner and W. C. Ellis,
Appl. Phys. Lett. **4**, 89 (1964).

[31] C. Y. Lee, T. Y. Tseng, S. Y. Li, P. Lin,
Tamkang Journal of Science and Engineering **6**, 127 (2003).

[32] H. J. Fan, P. Werner, M. Zacharias,
Small **2**, 700 (2006).

[33] S. Iijima,
Nature **354**, 56 (1991).

[34] N. Agrait, A. L. Yeyati, J. M. van Ruitenbeek,
Physics Reports **377**, 81 (2003).

[35] S. V. Khare, S. K. R. Patil, S. Kodambaka,
Handbook of Nanophysics: Nanotubes and Nanowires
(Taylor and Francis Group, LLC„ 2011).

[36] M. Califanoa and P. Harrison,
Journal of Applied Physics **9**, 5054 (1999).

[37] J. H. Hah *et al.*,
J. Vac. Sci. Technol. B **24**, 2209 (2006).

[38] J. Wang and L. Gao,
J. of Mate. Chem. **13**, 2551 (2003).

[39] K. K. Caswell, C. M. Bender, C. J. Murphy,
Nan **3**, 667 (2003).

[40] R. Furneaux, W. Rigby, A. Davidson,
Nature **337**, 147 (1989).

[41] G. Cao and D. Liu,
Advances in Colloid and Interface Science **136**, 45 (2008).

[42] T. Martensson, M. Borgstrom, W. Seifert, B. J. Ohlsson, L. Samuelson,
Nanotechnology **14**, 1255 (2003).

[43] Y. Hu, D. Perello, U. Mushtaq, M. Yun,
IEEE TRANSACTIONS ON NANOTECHNOLOGY **7**, 693 (2008).

[44] R. Adelung *et al.*,
Nature Materials **3**, 375 (2004).

[45] M. Elbahri, S. Jebril, S. Wille, R. Adelung,
Advances in Solid State Physics **48**, 27 (2009).

[46] M. Elbahri *et al.*,
Advanced Materials **1059**, 1059 (2006).

[47] S. Jebril *et al.*,
Small **4**, 2214 (2008).

[48] B. Su, Y. Wu, L. Jiang,
Chem. Soc. Rev. **41**, 7832 (2012).

[49] X. Ye, Y. Zhang, Y. Sun,
In *IEEE International Conference on Robotics and Automation* (2012).

[50] Y. Huang, X. Duan, Q. Wei, C. M. Lieber,
Sc **291**, 630 (2001).

[51] W. Lu and C. M. Lieber,
Nature Materials **6**, 841 (2007).

[52] G. Snider, P. Kuekes, R. S. Williams,
Nanotechnology **15**, 881 (2004).

[53] M. S. Islam, S. Sharma, T. I. Kamins, R. StanleyWilliams,
Nanotechnology **15**, L5 (2004).

[54] M. S. Islam, S. Sharma, T. Kamins, R. S. Williams,
Appl. Phys. A **80**, 1133 (2005).

[55] Y.-K. Chang and F. C.-N. Hong,
Nanotechnology **20**, 195302 (2009).

[56] E. F. Arkan, D. Sacchetto, I. Yildiz, Y. Leblebici, B. E. Alaca,
J. Micromech. Microeng. **21**, 1 (2011).

[57] B. Rogers, S. Pennathur, J. Adams,
Nanotechnology: Understanding Small Systems
(CRC Press Taylor & Francis Group„ 2008).

[58] J. G. Simmons,
Journal of Applied Physics **34**, 1793 (1963).

[59] A. Beiser,
Concepts of Modern Physics, 6th ed
(The McGraw-Hill Companies, Inc.„ 2003).

[60] V. V. Mitin, V. A. Kochelap, M. A. Stroscio,
Quantum Hetrostructures: Microelectronics and Optoelectronics
(Cambridge University Press„ 1999).

[61] J. Martinez-Duart, R. Martin-Palma, F. Agullo-Rueda,
Nanotechnology FOR Microelectronics AND Optoelectronics
(Elsevier B.V.„ 2006).

[62] M. V. Kamalakar,
Synthesis, characterization and investigation of electrical transport in metal nanowires and nanotubes,
PhD thesis Jadavpur University, Kolkata (2009).

[63] V. V. Mitin, V. A. Kochelap, M. A. Stroscio,
Introduction to Nanoelectronics: Science, Nanotechnology, Engineering, and Applications
(Cambridge University Press„ 2008).

[64] E. Sondheimer,
Advances in Physics **1**, 1 to 47 (1952).

[65] A. M. Song,
Encyclopedia of Nanoscience and Nanotechnology:Room-Temperature Ballistic Nanodevices
(American Scientific Publishers,, 2004).

[66] A. K. Theophilou,
Journal of Physics F: Metal Physics **2**, 1124 to 1136 (1972).

[67] V. E. Kenner, R. E. Allen, W. M. Saslow,
Physical Review B **8**, 576 (1973).

[68] T. T. Tsong and E. W. Müller,
physical Review **181**, 530 (1969).

[69] C. Kittel,
Introduction to Solid State Physics
(John Wiley & Sons, Inc,, 2005).

[70] N. W. Ashcroft and N. D. Mermin,
Solid State Physics
(Thomson Learning, Inc.,, 1976).

[71] C. T. Black and J. J. Welser,
IEEE Transactions On Electron Devices **46**, 776 (1999).

[72] H.-H. Cheng,
Metallic Nanotransistors,
PhD thesis University of Canterbury, (2008).

[73] S. Reif-Acherman,
Revista Brasileira de Ensino de Fisica **33**, 4602 (2011).

[74] V. H. Satheeshkumar,
Lecture note (2008).

[75] X. F. Wang *et al.*,
J. Appl. Phys. **89**, 3847 (2001).

[76] W. Williams and N. Giordano,
Phys. Rev. B **33**, 8146 (1986).

[77] G. D. Marzi, D. Iacopino, A. J. Quinn, G. Redmond,
J. Appl. Phys **96**, 3458 (2004).

[78] D. H. Seo, S. Kumar, K. K. Ostrikov,
J. Mater. Chem **21**, 16339 (2011).

[79] N. F. MOTT,
Philosophical Magazine, 19:160, 835-852 **19**, 835 (1969).

[80] W. Paschoal *et al.*,
Nano Letters **12**(9), 4838 (2012).

[81] F. Favier, E. C. Walter, M. P. Zach, T. Benter, R. M. Penner,
Science **293**(5538), 2227 (2001).

[82] G. Binnig, H. Rohrer, C. Gerber, E. Weibel,
Phys. Rev. Lett. **49**, 57 (1982).

[83] G. Binnig, C. F. Quate, C. Gerber,
Phys. Rev. Lett. **56**, 930 (1986).

[84] R. A. Wilson and H. A. Bullen.

[85] C. Brudle, C. E. JR., S. Wilson,
Encyclopedia of Materials Characterization: surfaces, interfaces and thin films
(Manning Publications Co.„ 1992).

[86] E. Fuchs and et al.,
Particle Beam Microanalyis: fundamentals, methods and applications
(VCH Verlagsgesellschaft GmbH„ 1990).

[87] C. Viti and M.-L. Frezzotti,
Lithos **55**, 125 (2001).

[88] D. B. Williams and C. B. Carter,
Transmission Electron Microscopy: A Textbook for Materials Science
(Springer„ 2009).

[89] N. Li and C.-M. Ho,
Lab on a Chip **8**, 2105 (2008).

[90] M. J. Madou,
Fundamentals of Microfabrication: The Science of Miniaturization
(CRC Press LLC,, 2nd edition, 2002).

[91] S. Muraka and et al,
VLSI Technology
(McGraw-Hill Series International Editions,, 1988).

[92] D. L. Smith,
Thin-Film Deposition: principles and practice
(McGraw-Hill, Inc.,, 1995).

[93] G. Sauerbrey,
Zeitschrift fiir Physik t55 **155**, 206 (1959).

[94] M. Ohring,
Material Science of Thin Films, Deposition and Structure
(Academic press,, second edition, 2002).

[95] K. Reichelt,
vacuum **38**, 1083 (1988).

[96] J. A. Venables, G. D. T. Spiller, M. Hanbucken,
Rep. Prog. Phys. **47**, 399 (1984).

[97] C. Rao, F. Deepak, G. Gundiah, A. Govindaraj,
Progress in Solid State Chemistry **31**, 5 (2003).

[98] Y. Xia, P. Yang, et al,
Advanced Materials **15**, 353 (2003).

[99] B. Yu and M. Meyyappan,
Solid State Electronics **50**, 536 (2006).

[100] Y.-T. Yin, Y.-Z. Chen, C.-H. Chen, L.-Y. Chen,
J. Chin. Chem. Soc. **58**, 1 (2011).

[101] Z. Zhang, S. J. Wang, T. Yu, T. Wu,
J. Phys. Chem. C **111**, 17500 (2007).

[102] M. E. Messing, K. Hillerich, J. Johansson, K. Deppert, K. A. Dick,
Gold Bulletin **42**, 172 (2009).

[103] D. Look,
Materials Science and Engineering: B **80**, 383 (2001).

[104] Y.-J. Hsu and S.-Y. Lu,
J. Phys. Chem. B **109**, 4398 (2005).

[105] O. Lupan *et al.*,
Sensors and Actuators B **144**, 56 (2010).

[106] P.-C. Chang *et al.*,
Chem. Mater. **16**, 5133 (2004).

[107] H. Tang *et al.*,
Journal of Material Science **44**, 563 (2009).

[108] P. Yang *et al.*,
Advanced Functional Materials **12**, 323 (2002).

[109] C. Borchers, S. Müller, D. Stichtenoth, D. Schwen, C. Ronning,
J. Phys. Chem. B **110**, 1656 (2006).

[110] S. Kaps *et al.*,
(2010).

[111] D. Gedamu, I. Paulowicz, S. Jebril, Y. KumarMishra, R. Adelung,
Journal of Nanotechnology **2012**, 1 (2012).

[112] X. Wang, J. Song, Z. L. Wang,
J. Mater. Chem. **17**, 711 (2007).

[113] H. Liu, K. Ishida, Z. Jin, Y. D. u,
Intermetallics **11**, 987 (2003).

[114] F. Xu, X. Liu, S. D. Tse, F. Cosandey, B. H. Kear,
Chemical Physics Letters **449**, 175 (2007).

[115] F. Xu, S. D. Tsea, J. F. Al-Sharab, B. H. Kear,
Appl. Phys. Lett. **88**, 243115 (2006).

[116] P. M. Rao and X. Zheng,
Nano Letters **9**, 3001 (2009).

[117] P. M. Rao and X. Zheng,
Proc. Combust. Inst. **33**, 1891 (2011).

[118] P. M. Rao, I. S. Cho, X. Zheng,
Proc. Combust. Inst. **34**, 2187 (2013).

[119] L. Caia, P. M. Raoa, Y. Feng, X. Zheng,
Proc. Combust. Inst. **34**, 2229 (2013).

[120] B. E. Alaca, H. Sehitoglu, T. Saif,
Appl. Phys. Lett. **84**, 4669 (2004).

[121] J. W. Hutchinson and Z. Suo,
Advances in Applied Mechanics **29**, 64 (1992).

[122] Z. Suo,
in Encyclopedia of Materials: Science and Technology
(Elsevier Science„ 2001).

[123] B. Audoly, B. Roman, A. Pocheau,
The European Physical Journal B **27**, 7 (2002).

[124] C. M. Stafford *et al.*,
Nature Materials **3**, 545 (2004).

[125] B. Cotterell and Z. Chen,
International Journal of Fracture. **104**, 169 (2000).

[126] H. Mei, Y. Pang, R. Huang,
Int. J. Fract. **148**, 331 (2007).

[127] H. Mei, Y. Pang, S. H. Im, R. Huang,
In *Thermal and Thermomechanical Phenomena in Electronic. 11th Intersociety Conference* (2008).

[128] A. A. Volinsky, N. R. Moody, D. C. Meyer,
In *11th International Congress on Fracture* (2005).

[129] D. H. Zhang and D. E. Brodie,
Thin Solid Films **238**, 95 (1994).

[130] S. Y. Chu, W. Water, J. T. Liaw,
Journal of the European CeramicSociety **23**, 1593 (2003).

[131] Q. H. Li, Q. Wan, Y. X. Liang, T. H. Wang,
Appl. Phys. Lett. **84**, 4556 (2004).

[132] H. Kind, H. Yan, B. Messer, M. Law, P. Yang,
Advanced Materials **14**, 158 (2002).

[133] J. B. K. Law and J. T. L. Thong,
Appl. Phys. Lett. **88**, 133114 (2006).

[134] J. D. Prades *et al.*,
The Journal of Physical Chemistry C **112**, 14639 (2008).

[135] Z. Fan *et al.*,
Appl. Phys. Lett. **85**, 6128 (2004).

[136] J. H. He, P. H. Chang, C. Y. Chen, K. T. Tsai,
Nanotechnology **20**, 1 (2009).

[137] C. Soci *et al.*,
Nano Letters **7**, 1003 (2007).

[138] S. Pearton *et al.*,
Progress in Materials Science **55**, 1 (2010).

[139] Y. K. Mishra *et al.*,
Particle & Particle Systems Characterization **30**(9), 775 (2013).

[140] S. M. Mahpeykar, J. Koohsorkhi, H. Ghafoorifard,
Nanotechnology **23**, 165602 (2012).

[141] A. Wagner, A. Behrends, A. Waag, A. Bakin,
Thin Solid Films **520**, 4637 (2012).

[142] L. Hu *et al.*,
Adv. Mater. **24**, 2305 (2012).

[143] M. W. Chen, C. Y. Chen, D. H. Lien, Y. Ding, J. H. He,
Optics Exp. **18**, 14836 (2010).

[144] D. S. Kim, R. Scholz, U. Gosele, M. Zacharias,
Small **4**(10), 1615 (2008).

[145] B. D. Cullity and S. Rstock,
Elements of X-Ray Diffraction
(Prentice Hall: New Jersey„ 2001).

[146] L. Chow, O. Lupan, H. Heinrich, G. Chai,
Appl. Phys. Lett. **94**, 163105 (2009).

[147] O. Lupan *et al.*,
Materials Research Bulletin **45**(8), 1026 (2010).

[148] U. Ozgur *et al.*,
J. Appl. Phys. **98**, 041301 (2005).

[149] O. Lupan *et al.*,
Sensors and Actuators B: Chemical **173**, 772 (2012).

[150] W. Limmer *et al.*,
Appl. Phys. Lett. **72**, 2589 (1998).

[151] T. C. Damen, S. P. S. Porto, B. Tell,
Phys. Rev. **142**, 570 (1966).

[152] O. Lupan *et al.*,
Thin Solid Films **519**(22), 7738 (2011).

[153] B.-R. Huang, J.-F. Hsu, C.-S. Huang, Y.-T. Shih, K.-S. Lu,
Materials Science and Engineering C **27**, 1197 (2007).

[154] B. Aksoy, S. Coskun, S. Kucukyildiz, H. E. Unalan,
Nanotechnology **23**(32), 325202 (2012).

[155] S.-E. Ahn *et al.*,
Appl. Phys. Lett. **80**, 153106 (2007).

[156] X. Zhang, X. Han, J. Su, Q. Zhang, Y. Gao,
Applied Physics A: Materials Science & Processing **107**, 255 (2012).

[157] O. Lupan *et al.*,
Phys. Status Solidi A **207**, 1335 (2010).

[158] L. Yingying, C. Chuanwei, D. Xiang, G. Junshan, Z. Haiqian,
J. Semicond. **30**, 063004 (2009).

[159] Y. Hao *et al.*,
Micro Nano Lett. **7**, 200 (2012).

[160] G. Blatter and F. Greuter,
Phys. Rev. B **33**, 3952 (1986).

[161] G. Blatter and F. Greuter,
Phys. Rev. B **34**, 8555 (1986).

[162] G. Chai, O. Lupan, L. Chow, H. Heinrich,
Sensors and Actuators A: Physical **150**(2), 184 (2009).

[163] P. Nguyen, S. Vaddiraju, M. Meyyappan,
Journal of Electronic Materials **35**, 200 (2006).

[164] M. C. Johnson, S. Aloni, D. E. McCready, E. D. Bourret-Courchesne,
Crystal Growth and Design **6**, 1936 (2006).

[165] A. Othonos, M. Zervos, D. Tsokkou,
Nanoscale Res. Lett. **4**, 828 (2009).

[166] A. Kar *et al.*,
Nanotechnology **20**, 1 (2009).

[167] A. Kolmakov, Y. Zhang, G. Cheng, M. Moskovits,
Adv. Mater. **15**, 997 (2003).

[168] A. Tischner *et al.*,
Microelectronic Engineering **86**, 1258 (2009).

[169] L. bao Luo, F. xia Liang, J. sheng Jie,
Nanotechnology **22**, 1 (2011).

[170] S. Mathur, S. Barth, H. Shen, J.-C. Pyun, U. Werner,
Small **1**, 713 (2005).

[171] B. J. Murray, E. C. Walter, R. M. Penner,
Science **4**, 665 (2004).

[172] K. Leitner, J. W. Schultze, U. Stimming,
J. Electrochem. Soc. **133**, 1561 (1986).

[173] N. K. Allam, K. Shankar, C. A. Grimes,
J. Mater. Chem., **18**, 2341 (2008).

[174] K. A. Lill, A. W. Hassel, G. Frommeyer, M. Stratmann,
Electrochim. Acta **51**, 978 (2005).

[175] J. M. Baik *et al.*,
Appl. Phys. Lett. **92**, 242111 (2008).

[176] G. Monty, K. Ng, M. Yang,
(2008).

[177] IEEE Int. Conf,
Sub-100 nm-scale Aluminum Nanowires by Stencil Lithography: Fabrication and Characterization 3 China (2008). Nano/Micro Engineered and Molecular Systems.

[178] M. Kang *et al.*,
Applied Physics Express **4**, 064104 (2011).

[179] J. Lee *et al.*,
Scripta Materialia **63**, 1009 (2010).

[180] D. S. Jeong, B.-K. Cheong, H. Kohlstedt,
Solid-State Electronics **63**, 1 (2011).

[181] T. Kaewmaneekul and G. Lothongkum,
Corrosion Science **66**, 67 (2012).

[182] B. C. Bunker *et al.*,
J. Phys. Chem. B **106**, 4705 (2002).

[183] M. Saif, S. Zhang, A. Haque, K. Hsia,
Acta Materialia **50**, 2779 (2002).

[184] H. Marom, J. Mullin, M. Eizenberg,
Phys. Rev. B **74**, 045411 (2006).

[185] C. Durkan and M. Welland,
Phys. Rev. B **61**, 14215 (2000).

[186] W. Steinhögl, G. Schindler, G. Steinlesberger, M. Engelhardt,
Phys. Rev. B **66**, 075414 (2002).

[187] T. Chui, G. Deutscher, P. Lindenfeld, W. L. McLean,
Phys. Rev. B **23**, 6172 (1981).

[188] N. Klein and H. Gafni,
Electron Devices, IEEE Transactions on **13**(2), 281 (1966).

[189] C. Di *et al.*,
SCIENCE CHINA Physics, Mechanics and Astronomy **54**, 1190 (2011).

[190] G. Pfefferkorn,
Naturwiss **40**, 551 (1953).

[191] R. Takagi,
Journal Of The Physical Society Of Japan **12**, 1212 (1957).

[192] K. Nagato, M. Furubayashi, T. Hamaguchi, M. Nakao,
Journal of Vacuum Science Technology **B28**, C6P11 (2010).

[193] R. Tallman and E. Gulbransen,
Nature **218**, 1046 (1968).

[194] D. Voss, E. Butler, T. Mitchell,
Metallurgical and Materials Transactions A **13A**, 929 (1982).

[195] Y. Fu, J. Chen, H. Zhang,
Chemical Physics Letters **350**, 491 (2001).

[196] B. Zong *et al.*,
Chem. Mater. **17**, 1515 (2005).

[197] U. Cvelbar, Z. Chen, M. K. Sunkara, M. Mozetic,
Small **4**, 1610 (2008).

[198] R. L. Tallman and E. A. Gulbransen,
J. Electrochem. Soc. **114**, 1227 (1967).

[199] L. Yuan *et al.*,
Mate. Sci. and Eng.: B **177**, 327 (2012).

[200] P. Barna and M. Adamik,
Thin Solid Films **317**, 27 (1998).

[201] A. G. Nasibulin *et al.*,
Nano Res. **2**, 373 (2009).

[202] S. Ciraci, A. Buldum, I. P. Batra,
J. Phys.: Condens. Matter **13**, R537 (2001).

[203] K. Takayanagi, Y. Kondo, H. Ohnishi,
JSAP international **3**, 3 (2001).

[204] J. I. Pascual, J. Mendez, J. Gomez-Herrero, A. M. Baro, N. Garcia,
J. Vac. Sci. Technol. B **13**, 1280 (1995).

[205] B. Laikhtman and S. Luryi,
Phys. Rev. B **49**, 17177 (1994).

[206] A. I. Yanson, G. R. Bollinger, H. E. van den Brom, N. Agrait, J. M. van Ruitenbeek,
Nature **395**, 783 (1998).

[207] A. M. Song,
*Encyclopedia of Nanoscience and Nanotechnology: Room - Temperature Ballistic Nanodevices*volume 9
(American Scientific Publishers,, 2004).

[208] R. Landuer,
R. Landauer, Philos. Mag. , 863 (1970). **21**, 863 (1969).

[209] G. Govindaraj and V. Devanathan,
Physical Review B **34**, 5904 (1986).

[210] J. L. Costa-Kramer,
Phys. Rev. B **55**, R4875 (1997).

List of Figures

List of Publications

1. **D. Gedamu**, I. Paulowicz, S. Kaps, S. Wille, O. Lupan, G. Haidarschin,Y. K. Mishra, R. Adelung, Rapid Fabrication Technique for Interpenetrated ZnO Nanotetrapod Networks for fast UV-sensors, *Advanced Materials*, (2013) doi: 10.1002/adma.201304363.

2. **D. Gedamu**, B. Erkatal, O. N. Urs, S. Kaps, Y. K. Mishra, L. Kielne, A. F. Thajudin, K. Schlüter, E.Quandt, R. Adelung, Formation and Integration of Iron-Iron oxide Nanowire Bridged Gaps on Microchips by Simple Annealing, *Manuscript in preparation*, (2013).

3. L. Ghimpu, I. Tiginyanu, O. Lupan, Y.K. Mishra, I. Paulowicz, **D. Gedamu**, A. Cojocaru, R. Adelung, Effect of Al, Sn - Doping on Properties of Zinc Oxide Nanostructured Films Grown by Magnetron Sputtering, *Proceedings of the International Semiconductor Conference, CAS (2013) Sinaia (Romania), IEEE*, **1**,(2013), 133.

4. Y. K. Mishra, S. Kaps, A. Schuchardt, I. Paulowicz, Xin Jin, **D. Gedamu**, S. Wille, O. Lupan, R. Adelung, Fabrication of Macroscopically Flexible and Highly porous 3D Large scale fabrication of complex shaped metal oxide nano- microstructures and their interconnected networks for multifunctional applications, Accepted in *Kona Powder and Particle Journal*, (2013).

5. Y. K. Mishra, S. Kaps, A. Schuchardt, I. Paulowicz, Xin Jin, **D. Gedamu**, S. Freitag, S. Wille, M. Claus, A. Kovalev, S. N. Gorb, R. Adelung, Fabrication of Macroscopically Flexible and Highly porous 3D Semiconductor Networks from Interpenetrating Nanostructures by Simple Flame Transport Approach, *Particle and Particle Systems Characterization*, **30**, 9(2013), 775.

6. E.S. Zarie, V. Kaidas, **D. Gedamu**, Y.K. Mishra, R. Adelung, F.H. Furk-

ert, R. ScherlieSS, H. Steckel, B.G. Schreiber, Solvent free fabrication of micro and nanostructured drug coatings by thermal evaporation for controlled release and increased effects, *PLoS ONE*, **7**, 8(2012), **e40746**.

7. S. Wille, Y.K. Mishra, **D. Gedamu**, I. Paulowicz, X. Jin, R. Adelung, Zinc Oxide micro- and nanostructures as multifunctional materials, *SPIE Newsroom* (2011).

8. S. Wille, Y.K. Mishra, **D. Gedamu**, S. Kaps, X. Jin, T. Koschine, A. Bathnagar, R. Adelung, ZnO core spike particles and nano-networks and their wide range of applications, *Proc. SPIE*, **8068** (2011), 806816-1.

9. **D. Gedamu**, I. Paulowicz, S. Jebril, Y. Kumar Mishra, R. Adelung, Procedures and properties for a direct nano-micro integration of metal and semiconductor nanowires on Si chips, *Journal of Nanotechnology*, **2012**(2012).

10. **D. Gedamu**, S. Jebril, A. Schuchart, M. Elbahri, S. Wille, Y.K. Mishra, R. Adelung, Examples for the integration of selforganized nanowires for functional devices by a fracture approach, *Physica Status Solidi B*, **247**(2010), 2571.

Appendices

Appendix A: Introduction to Methods

In this study, nanostructures ranging from fine NWs to microsized whiskers are synthesized through implementing three techniques: Flame Transport Synthesis (*FTS*), Thin Film Fracture (*TFF*) and Thermal Annealing Method (*TAM*). Each technique has a unique approach that provides a unique advantage as discussed in details in the subsequent chapters. Compared to other synthesis techniques, these techniques are alternatives to other methods that offer less complicated processing, cost effective device synthesis, short processing time and most importantly they provide direct integration of NW and nanostructures into chips. Interestingly, the direct and easy integration of the NWs with their electrodes offers ready-made device for measurement without further processing step for electrode deposition.

FTS is further classified into two categories: Burner-FTS (*B-FTS*) and Crucible-FTS (*C-FTS*). B-FTS like all other approaches, the ZnO network structures are grown on a lithographically micro-structured gold electrodes. A ceramic mask that has a mm^2 size window is used to deposit a stream of hot ZnO particles from the burner. High magnification SEM images revealed a deposition of network of ZnO nanotetrapods and nanostructures bridging the 10 μm gap. As demonstration a photodetector device with fast response time constant ($\sim$ 32 ms) under 365 nm UV exposure with an on/off ratio $\sim$ 4.5 10^3 at 2.4 V) is shown.

The second FTS based synthesis approach for fabricating ZnO nanostructures is C-FTS. It is one of novel and versatile FTS based synthesis approach used in synthesizing ZnO nanostructures. This method was used to synthesize ZnO and SnO_2 NW network structures on lithographically patterned gold electrodes. Quartz glass and silicon substrate are successfully used in synthesis as given in

the result and discussion part. Depending on the the temperature and precursor composition, ZnO NWs of various morphology could be synthesized. ZnO nano needles (up to 1 mm length), nano spikes, nano rods and ZnO tetrapods or some times the combination of different shapes growing catalytically on micro-patterned gold and bridging gaps are synthesized and shown. Measurements of both ZnO and SnO_2 NWs as a photodtector exhibited promising result with more than 100 on/off ratios in response to 365 nm wavelength UV light.

Another novel and versatile approach used in synthesizing NWs is TFF approach. The TFF approach in principle is proved to be compatible to synthesize and convert nearly all materials ranging from metals to metal oxides into NW materials. In this work, TFF approach is used to synthesize NWs from Ti, Pd, Al, and ZnO. Using these materials, NWFET, gas sensor and photodetectors are synthesized. For instance, electrochemically anodized core shell Ti NW and Al NW were shown to being converted to NW field effect transistor (NWFET). Metal oxide NW and nanostructures have also shown a promising result as gas sensors and photo detectors. A modified version of TFF approach is also used to synthesize Al NWFET on electrochemically anodized Nb/Al layer system as a dielectric material. In addition to this, lithographically confined area offers a possibility for localized gate voltage application.

TAM is the other simple approach used to synthesize iron oxide and core-shell iron oxide nanospikes and whiskers from lithographically patterned iron film. A typical temperature of 300 ^oC and 450 nm thick iron film are found to be the best efficient parameters for the synthesis of micrometer sized long nanospikes under ambient conditions. A muffle type of furnace with limited access to air resulted in iron oxide NW with out any core-shell iron. However, iron oxide NWs with iron core in the middle is synthesized in open air annealing on hot plate. The possibilities of using such NWs a magnetic field sensor are shown through electrical measurement under magnetic field application.

Appendix B: Ballistic and Diffusive Electron Transport

The electrical conductance in a conductive wire is inversely proportional to its length and every material has definite conductivity. The electrical conductance G which of the interest is given by the ratio of the current I to the voltage drop ($G = I/V$). Using the relationship of current density (j) to electric field and $E = V/l$ where l is length of conductor and $I = jw$, the conductance for 2D synstem is thus [202]

$$G = \sigma \frac{w}{l} \tag{7.1}$$

For a 3D conductor, this relationship is valid provided that w is replaced by the cross sectional area A orthogonal to the current flow direction. With the continuation of miniaturization of microelectronic devices, it was pointed out that the electrical properties nano scaled devices of the same material differ from that of larger dimensions. The size-dependent effects start to emerge as the width w and length l are reduced towards atomic dimensions in the nanometer range. Equation 7.1 holds in the diffusive transport regime when both w and l are greater than the mean free path. As the length of the wire is reduced to the mean free path of the electrons, the conductance of the wire changes from diffusive to ballistic as depicted in Figure 7.1a). This is a state where quantum confinement effects are start to be noticed and lead to quantized conductance [203], [204], [202]. In ballistic transport electrons are able to travel without being impeded by atoms, molecules, defects, impurities or electrons within the transport medium. With the reduction of the length of the wire below the mean path of electrons l_m and width of the wire in nanometer or Fermi wavelength(λ_F) scale, the conductance in the NW will be quantized in $2e^2/h$ steps. The Fermi wavelength λ_F at room temperature in typical metals is about 0.5 nanometers. The conductance in a narrow constriction of the NW formed between two electrodes is given by the famous Landauer formula [205]:

$$G = \frac{2e^2}{h} T \tag{7.2}$$

where $T = \sum \tau_{ij}$ is transmission. For perfect transmission $T \sim 1$, the conductance is still finite and equal to $2e^2/h$. This corresponds to a resistance

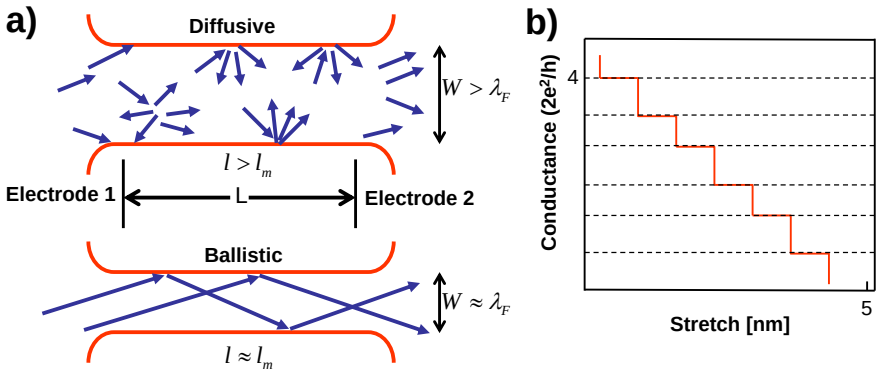

Figure 7.1: *a) Diffusive (top) and ballistic (bottom) transport of electrons in one-dimensional wires. l_m, is the mean free path of the electrons, and λ_F is the Fermi wavelength[203]. b) Schematics of conductance quantization when a metal NW is under stretching condition. Dashed lines denote $2e^2/h$ intervals. Experimental result for conductance measurement of NWs stretched through piezo stage is reported in [204].*

$R = h/2e^2 = 12.9\ k\Omega$ and is attributed to the resistance at the contacts where the conductor is attached to the electrodes or electron reservoirs. In Figure 7.1b), measurements of room-temperature electronic transport in pulled metallic NWs are presented, demonstrating that the conductance characteristics depend on the length, lateral dimensions, state and degree of disorder, and elongation mechanism of the wire. Conductance during the elongation of short Au NW (length $\sim$ 50Å) exhibits periodic quantization steps with characteristic dips, correlating with the order-disorder states of layers of atoms in the wire[204]. Yanson et al., also employed a mechanically controllable break-junction technique to stretch a contact of Au electrodes over 20 Å forming to form a chain of single atoms [206] and confirmed similar results at a temperature of 4.2 K where a conductance $G_0 = 2e^2/h$ is observed before rapture. The quantum size effect for electrical conductivity in thin metal films is studied using variety of models and experiments [207],[208], [209], [210] etc . All of them revealed and emphasized the importance of atomic structure and size of nanostructure dimensions on the electron transport properties.

Eidesstattliche Erklärung

Hiermit erkläre ich an Eides Statt, diese Arbeit selbständig angefertigt und keine weiteren Quellen und Hilfsmittel auSSer den im Text angegebenen sowie den bekannten Nachschlagewerken der Naturwissenschaften verwendet zu haben.

Kiel, am März 2014

(Dawit Gedamu)